Investigating Complexity in Networks of Percolating Tin Nanoparticles

A thesis submitted in partial fulfilment
of the requirements of the degree of

Master of Science in Physics
at the
University of Canterbury

Ford Wagner

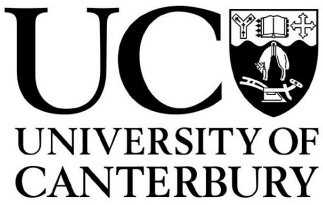

Supervised by Professor Simon Brown

Physics and Astronomy, School of Physical and Chemical Sciences, University of Canterbury, Christchurch, New Zealand

Abstract

Computers have grown exponentially more powerful for decades, and so too has their ubiquity in human society. Continued growth, formalised through Moore's Law, is under threat from fundamental limitations in component miniaturisation. Additionally, disadvantages with traditional computer architectures, such as the von Neumann bottleneck, lead to energy inefficiencies and increased costs. In contrast, the brain boasts extreme energy efficiency with the ability to complete complex pattern recognition, prediction, and abstraction tasks.

Neuromorphic computing takes inspiration from the human brain with the aim of developing a new generation of computers. There are many neuromorphic architectures in development world-wide with many attempting to emulate individual neurons and synapses. Percolating atomic switch networks (PASNs) take a different approach by using self-assembly to mimic the complex connectivity of the human brain.

The focus in this thesis is the fabrication of multi-electrode PASNs. First, key switching activity statistics (voltage dependence of the event rate, distribution of times between consecutive switching events, and avalanche statistics) are compared between the multi-electrode and previous two-electrode device geometries to establish that the new device geometry does not qualitatively change the switching activity. The remainder of the thesis investigates the qualitative and quantitative complexity of physical and simulated multi-electrode PASNs. The qualitative analysis demonstrates that the switching activity is qualitatively complex and related to the fractal structure of the PASN. The quantitative analysis applies a metric for complexity in neural systems and shows that PASNs are complex according to that metric. Finally, the complexity of PASNs is compared to that of biological systems.

Acknowledgements

Firstly, thank you to Professor Simon Brown for the opportunity to join the neuromorphic research team, and for your constant support and advice throughout the year. Thank you to Edoardo Galli, Dr. Susant Acharya, Dr. Joshua Mallinson, and Dr. Saurabh Bose for teaching me the ins and outs of the devices, and always being willing to help with my questions. To Zachary Heywood, thank you for all the simulations you ran that helped me complete this research. Thank you to everyone else in the neuromorphic research team for your help learning about neuromorphic computing and your feedback on my work and ideas. You all played a huge role in this research and I couldn't have done it without you all.

I would like to thank my partner, Emily, for her endless patience and support through the many long nights spent working on my research. Finally, thank you to all my friends and family who have helped keep me sane throughout my studies.

Contents

List of Figures

List of Tables

Chapter 1

Introduction

Computers have revolutionised human society. The rapid integration of computers into communication, banking, and science has inspired the past 50 years to be known as the "Information Age". Over this time, we have become accustomed to an exponential growth in computational power. This growth is formalised through Moore's Law, which predicts the number of transistors on an integrated circuit will double approximately every two years [2]. Originally, Moore predicted this relationship would hold for 10 years, but incredibly, it has roughly held for over 50 [3].

The complementary metal oxide semiconductor (CMOS) transistor is the essential component of conventional computers. The inspiration behind Moore's Law came from the remarkable observation that packing more CMOS transistors on an integrated circuit made each individual transistor cheaper [4]. However, the foundational cost benefits of Moore's Law have significantly weakened over time - it now requires 18 times the number of researchers to double the number of transistors per integrated circuit than it did in the 1970's [5]. Additionally, CMOS transistors are approaching fundamental limits in scalability; the smallest fabricated transistor is 1nm across, or approximately 10 atoms [6]. It is clear that Moore's Law will not hold indefinitely, and so other avenues must be explored to continue increasing computational power.

When thinking about computers after Moore's Law, it is natural to look at the most advanced computer in history: the human brain. Even after half a century of exponential improvement, modern computers struggle to compete with the complex planning, decision making, and pattern recognition of the brain [7]. There have been many attempts to design computers that can surpass the brain. However, these attempts are restricted to specialised tasks, such as playing classic board games [8]. A famous example is the computer program AlphaGo, which was designed to master the game of Go. AlphaGo made history when it defeated 18 time world-champion Lee Sedol [9]. While impressive, it is important to note that AlphaGo required approximately 5,000W of power, whereas Sedol's brain used around 20W [10].

To narrow the gap between computers and the brain, alternative computer architectures and components need to be considered. A promising approach is *neuromorphic computing*, a term first coined by Carver Mead [11]. Neuromorphic computing aims to create a new generation of computers that can complete complex tasks with the energy efficiency of the brain [12]. This thesis focuses on percolating atomic switch networks (PASNs), which are a

promising neuromorphic architecture [13–18].

The remainder of this chapter provides relevant background on neuromorphic computing, the brain, neural networks, and the current neuromorphic architecture research (Section 1.1). Section 1.2 introduces the key concepts of PASNs and the important results achieved thus far. Finally, Section 1.3 provides an overview of the goals for this thesis and outlines the thesis structure.

1.1 Neuromorphic Computing

Carver Mead described a neuromorphic system as the very large scale integration (VLSI) of analogue components to simulate a biological system [11]. In modern times, the definition encompasses both a range of hardware and software implementations of neural networks [19]. However, software approaches rely on conventional hardware architectures, which are approaching limitations for further improvement. Therefore, software implementations will only be briefly described in Section 1.1.3, while the rest of this thesis will focus on hardware approaches to neuromorphic computing, now referred to as neuromorphic architectures.

The following subsections compare neuromorphic architectures to the ubiquitous von Neumann architecture (Section 1.1.1), and describe the basic components of the brain and its computational advantages (Section 1.1.2). Next, artificial neural networks are discussed in Section 1.1.3 to explain how neuromorphic computing can be applied in software. Finally, Section 1.1.4 summarises several different neuromorphic architectures that are in development.

1.1.1 Neuromorphic Architectures and the von Neumann Architecture

Conventional computers are based on the von Neumann architecture [20]. This architecture revolutionised computers by unifying and simplifying many engineering and programming challenges of the time [21, 22]. The main components of the von Neumann architecture are the central processing unit (CPU), memory, and the input/output. Figure 1.1 (a) shows a diagram of the von Neumann architecture.

The CPU and memory are separated in the von Neumann architecture, which leads to massive amounts of data being transferred from one to the other [21]. Moreover, while the performance of the CPU has doubled every two years (Moore's Law), the performance of memory has only doubled every 10 years [23]. This forces the processor to wait to receive data from the memory, which wastes energy and restricts performance. The transfer of information between memory and the CPU is called the von Neumann bottleneck, and it severely limits the potential of the von Neumann architecture.

Conventional computers with von Neumann architectures rely on CMOS transistors. These transistors are incredibly power hungry in large numbers, rely on primarily serial processing, and require explicit programming [24]. In contrast, the human brain is extremely energy efficient, massively parallel, and can learn and adapt to its environment [19]. Neuromorphic architectures take inspiration from biological information processors to attempt to

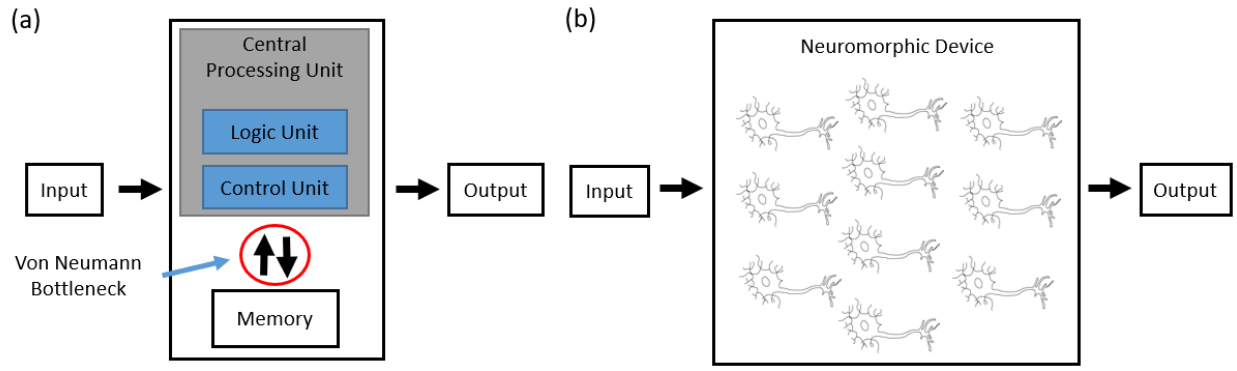

Figure 1.1: *(a) Schematic of the von Neumann architecture. The transfer of data between the memory and the CPU causes the von Neumann bottleneck. (b) Schematic of a neuromorphic architecture. Many neurons can act in parallel to efficiently complete complex tasks.*

emulate the computational advantages of the brain.

A broad range of neuromorphic architectures exist, and many utilise networks of artificial neurons and synapses that function similarly to their biological counterparts [19, 25]. Furthermore, the synapses in the network demonstrate plasticity, which allows them to learn from prior inputs and the environment [24]. Neurons and synapses are discussed in more detail in Section 1.1.2.

In neuromorphic architectures, computation and memory are collocated to eliminate the von Neumann bottleneck. Furthermore, information can be processed in parallel, which avoids the high energy cost of synchronous communication managed by a single clock in conventional computers [26]. Figure 1.1 (b) shows neurons in a neuromorphic architecture.

Neuromorphic architectures also present excellent platforms for machine learning. Currently, most machine learning runs in software artificial neural networks (Section 1.1.3). These artificial neural networks are typically run on conventional computer hardware, and they have successfully been implemented for computer vision, speech recognition, classification tasks, robot control, and other applications [27]. However, forcing brain-like computation on rigid, von Neumann architectures is highly inefficient - hence why AlphaGo required 5,000W to operate [28]. Neuromorphic architectures are more amenable to brain-like computation, and could dramatically increase the efficiency of machine learning algorithms [19]. Overall, neuromorphic architectures have the potential to be more energy efficient, powerful, and adaptable than conventional computers.

1.1.2 The Brain

There are billions of neurons in the brain that serve critical roles for information processing [29, 30]. Neurons are connected by synapses, and each neuron can be connected to thousands of others. Information is transmitted between neurons through electrical signals called action potentials. These signals travel along the axon towards the synapses. Figure 1.2 shows a schematic for a pair of connected neurons with an action potential being transmitted.

When an action potential reaches a synapse, it stimulates the release of neurotransmitters

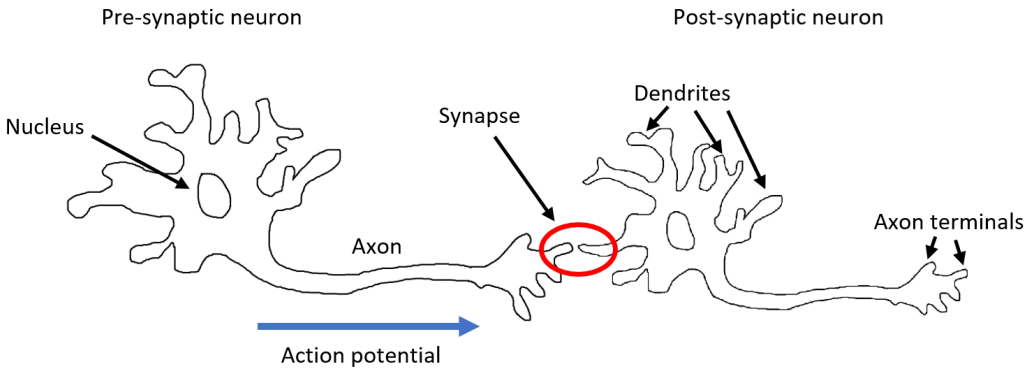

Figure 1.2: *Schematic of two connected neurons. The pre-synaptic neuron transmits an action potential along its axon, which stimulates the release of neurotransmitters across the synapse and towards the post-synaptic neuron. The post-synaptic neuron will fire an action potential when the summed input at its synapses is great enough.*

that can excite or inhibit activity in the post-synaptic neuron. The excitatory and inhibitory inputs are summed across all the synapses of a neuron. If the summed signal is great enough, then the post-synaptic neuron will fire an action potential that acts as an input for other neurons. The input from a neuron will fade over time at the synapse, therefore inputs are summed both temporally and spatially at the synapses [31].

The neurons fire action potentials while the synapses control the strength of the signal received by other neurons. An important property of synapses is plasticity, which allows the strength of the synaptic response to increase or decrease with repeated stimulation. This can increase or decrease the chance that another neuron fires an action potential, and is thought to be critical for learning [32, 33].

The brain exhibits emergent properties. That is, the brain's capabilities emerge from the complex network of neurons and synapses, rather than from the properties of the individual components [34]. Research has shown the brain exhibits small world properties [35], which means there are high degrees of connectivity between neighbouring neurons to form clusters, and short paths that connect distant clusters to one another. Additionally, the brain has a hierarchical structure [36] and a scale-free topology, which means the number of connections per neuron is distributed as a power law [17]. These properties have been linked to efficient global information transfer and minimal wiring costs [37].

1.1.3 Artificial Neural Networks

Artificial neural networks (ANNs) are software implementations of neuromorphic computing concepts, that model the function of biological neurons and synapses [38,39]. These networks are widely used for classification, prediction, and modelling tasks among others [40].

ANNs operate by 'learning' from previous data. For example, an ANN can be trained to identify dog breeds through observation of many images of dogs. Initially, the network is presented with dog images and the breed name. Every image provides information about the characteristic features of the dog breeds, and the ANN eventually learns to identify the images based on these features. Once the network is sufficiently trained, it can identify dog

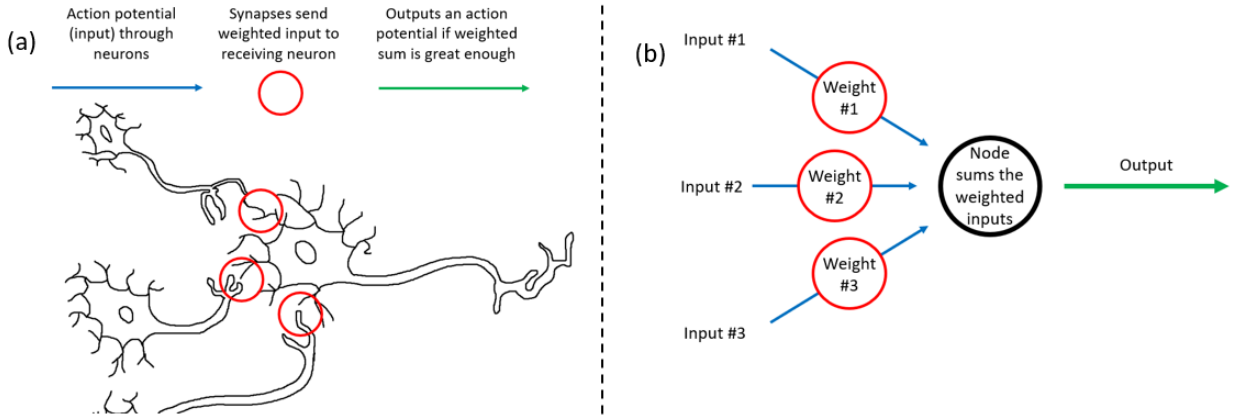

Figure 1.3: *(a) Schematic of a biological neural network. The action potentials from neurons on the left act as inputs for the neuron to the right. Synapses add a weight to the strength of each input. If the weighted sum is great enough, then the neuron to the right will fire an action potential towards even more neurons. (b) Schematic of an ANN. Inputs are received from nodes (not shown) and weighted. The weighted inputs are then summed at the receiving node and the sum determines the output.*

breeds from new images. A traditional algorithm could be coded that checks for predefined features until the image can be classified. However, this process is relatively slow, inflexible, and requires human presumptions about the key data features to work. In contrast, an ANN can learn extremely quickly and does not rely on predefined relationships in the data [41].

An ANN is composed of nodes (analogous to neurons) with weighted connections (analogous to synapses) between them. A node receives inputs from other nodes, and the weighted sum of these inputs determines the output. Figure 1.3 (b) shows the simplified structure of an ANN alongside the biological analogue (Figure 1.3 (a)). The simple structure in Figure 1.3 (b) is the building block of ANNs, and a practical ANN will have many layers of nodes connected to one another. The success of an ANN depends on how closely the final output matches the target output. The network is trained through adjustment of the weights between nodes. These weight adjustments can be viewed as mimicking plasticity in biological synapses [40].

Feed-Forward and Recurrent Neural Networks

There are many types of ANN, but nearly all of them consist of three layer groups. First is the input layer, which receives external information and transfers it to the rest of network. Second is the hidden layer, in which nodes communicate with other nodes to transform the input. Note that the hidden layer is typically comprised of many layers of nodes. Finally, there is the output layer, which receives the transformed signal from the hidden layer and produces the final output [40].

Information transfer varies greatly between different ANN types. For example, a feed-forward neural network only allows information to travel in one direction, whereas a recurrent neural network has information flowing both forwards and backwards. Figure 1.4 shows the three layers of ANNs with arrows representing the flow of information. The black arrows all point in the same direction and represent information flow in a feed-forward neural

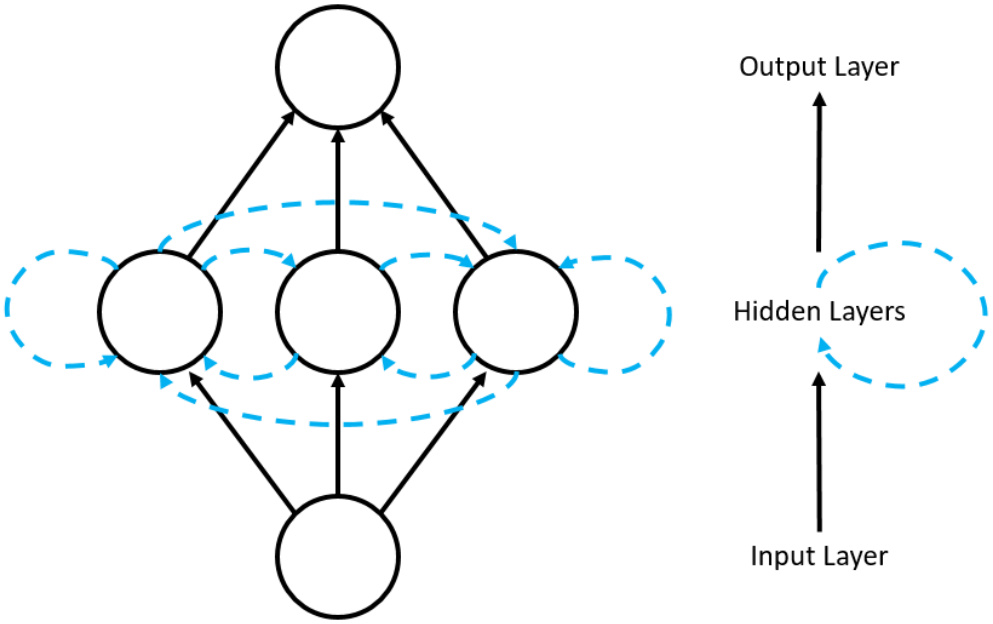

Figure 1.4: *Schematic of the layers in a neural network. The black arrows all point in the same direction and represent the transport of information in a feed-forward neural network. The blue arrows represent recurrence between layers and create feedback loops. Recurrent neural networks are represented by both the blue and black arrows. Note that the hidden layer typically holds many layers of neurons instead of the one layer shown here.*

network. The blue arrows can send information backwards to create feed-back loops, and the combination of blue and black arrows represents a recurrent neural network.

Feed-forward neural networks can excel at data classification tasks when the different data elements are independent of one another. Furthermore, they are relatively easy to train due to their simple structure and unidirectional information flow. However, these networks have no feedback or memory of past input, which means they struggle with tasks where the data elements are correlated, such as in time-series prediction tasks [42].

Recurrent neural networks overcome the limitations in feed-forward neural networks by sending information in multiple directions. This information flow introduces loops which can maintain some information from past inputs, and allows the network to process sequences of data [43]. Recurrent neural networks have been extremely successful in time-series prediction tasks and speech recognition [43]. However, the introduction of recurrent loops leads to significantly more complicated training processes, that are both computationally expensive and time consuming. One approach that maintains the benefits of recurrence while dramatically simplifying training is called reservoir computing.

Reservoir Computing

Reservoir computing (RC) has similar information flow to a recurrent neural network, but only the weights on the final layer are trained instead of the weights on all connections [44]. RC is incredibly simple, and results in significantly faster and computationally cheaper network training compared to training all weights in a recurrent neural network. RC has been successful in wave generation and time-series prediction tasks, which includes the bench-

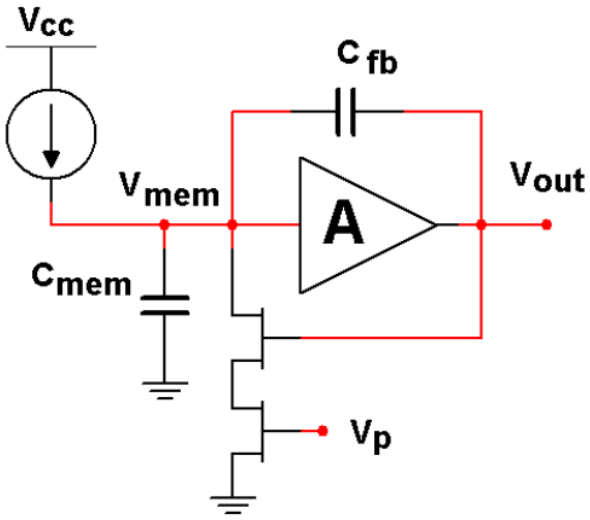

Figure 1.5: *Circuit diagram of Carver Mead's integrate and fire neuron model. Reproduced from [24] ©2016IEEE.*

mark Mackey-Glass prediction task [45, 46].

RC is an attractive option for physical networks with many connections that cannot be individually adjusted, as is the case for PASNs (Section 1.2.4).

1.1.4 Neuromorphic Architectures

Most neuromorphic architectures utilise silicon technologies that approximate biological neurons and synapses [24]. Some research also investigates the use of emerging materials, such as novel semiconductors, for neuromorphic applications [24, 47]. This section provides a brief introduction to some neuromorphic architectures. A comprehensive review can be found in [19].

Regular Arrays of Neurons and Synapses

The most common neuromorphic architectures are regular arrays of components that approximate neurons and synapses [24]. Neurons are often approximated by spiking models, which release an electrical signal that mimics an action potential. More complex spiking models, such as the Hodgkin-Huxley model, aim to be biologically realistic, whereas simple spiking models, such as the integrate-and-fire model, focus solely on emulating neuron function [48, 49].

Carver Mead designed a simple circuit for an integrate-and-fire neuron [50]. Since then, many other models such as log-domain low-pass filters have been proposed [51]. Figure 1.5 shows a circuit diagram of Mead's integrate-and-fire neuron [24]. Silicon electronics are the most common components in these neuron models [48].

Along with neuron models, several synapse models based on silicon technology have been used in neuromorphic architectures [52]. However, these artificial synapses consist of bulky, complex circuits, and so interest has shifted towards using memristors to emulate

synapses [24]. A memristor is a fundamental electrical component, which consists of two-terminals and relates magnetic flux to electric charge. In practical applications, memristors can behave as variable resistors that maintain their resistance even when they lose power [53].

The non-volatile and history dependent resistance of memristors is reminiscent of plasticity in biological synapses, which makes memristors attractive options to emulate synapses. Moreover, memristors are generally smaller, cheaper, and more energy efficient than silicon based synapse models [24, 54, 55]. Memristors can be positioned in-between model neurons in cross-bar arrays, so that the memristor controls the signal being transmitted between neurons [56, 57]. Cross-bar arrays of memristors have successfully performed classification tasks [58], efficiently solved differential equations [59], and can store complex binary data [60].

Neuromorphic architectures typically consist of artificial neurons and synapses arranged in regular arrays, such as the memristor cross-bar arrays [19]. Notable implementations of neuromorphic architectures include the silicon retina, which uses an array of CMOS-based neurons to produce a retina with lower power consumption and latency than conventional image sensors [61], and IBM's TrueNorth chip, which boasts over one million silicon neurons and 256 million CMOS synapses, and can recognise objects in video in real-time [61–64]. Despite their potential, these regular arrays lack the structural complexity of the brain, which may be essential to achieve truly brain-like computation [17].

Self-Assembled Nanowire Networks

Biological networks have intrinsically complex structures and exhibit emergent behaviours [17]. To mimic the structural characteristics of the brain, nanowire networks have been fabricated through bottom-up techniques [65]. These self-assembled nanowire networks possess complex structures that are linked to their dynamics in a similar way to the brain [25]. Moreover, the fabrication of nanowire networks is easily scaled, which eliminates a serious challenge faced by regular arrays of neurons and synapses.

Networks of Ag_2S-Ag (silver sulphide - silver) nanowires exhibit brain-like properties, and have shown success in signal classification tasks [65, 66]. Networks of Ag-PVP (silver - polyvinylpyrrolidone) nanowires have tunable conductivities, and have shown associative learning of spatial patterns [25, 67]. Other networks have been fabricated with metallic nanowires coated with metal oxides or other electrolytes [25]. Simulations and experiments of nanowire networks have shown the potential for reservoir computing [45, 68, 69].

Nanowire networks have demonstrated that self-assembled low-dimensional systems are promising candidates for neuromorphic applications. Percolating atomic switch networks are another promising self-assembled network that are discussed in detail in the following section.

1.2 Percolating Atomic Switch Networks

Percolating atomic switch networks are networks of nanoparticles poised at the percolation threshold that exhibit atomic switching dynamics [13]. This section establishes the key concepts of PASNs, and summarises the relevant research and results. Section 1.2.1 describes

the key properties of nanoparticles and nanoclusters. Section 1.2.2 introduces percolation theory and how it can model the conductance of PASNs as they are deposited. Section 1.2.3 discusses the mechanisms for atomic switching in PASNs. Finally, Section 1.2.4 highlights the current research into PASNs.

1.2.1 Nanoparticles and Nanoclusters

Nanoclusters are generally defined as aggregates of atoms or molecules with at least one dimension between 1-10nm [70]. Nanoclusters are a subset of nanoparticles (NPs) which can be as large as 100nm in each dimension [71]. In this thesis, nanoclusters describe agglomerations of atoms or molecules up to 10nm in each dimension, while NPs describe structures from 10-100nm in each dimension.

Nanoclusters and NPs have a very high surface-to-volume ratio, which means their properties vary greatly from their bulk counterparts [72]. For example, bulk gold is an inert metal, whereas gold NPs are highly reactive and can be used as catalysts [73]. Additionally, nanoclusters and NPs exhibit size dependent melting points and optical properties, and are small enough to exhibit quantum mechanical behaviours [70]. Overall, the unique properties of nanoclusters and NPs make them ideal candidates for novel materials and devices.

In this thesis, nanoclusters of tin (diameter ~7nm) were produced using inert gas aggregation (IGA) [74]. In IGA, sputtered atoms are added to a low-temperature flowing inert gas. The atoms aggregate into nanoclusters in a condensation like process with little risk of contamination due to the inert gas environment [75]. The nanoclusters are deposited on a substrate and coalesce together to form NPs which have dimensions ~20-50nm. The deposition system and IGA process are described in detail in Chapter 2.

1.2.2 Percolation Theory

The deposition of PASNs can be modelled with percolation theory. [76, 77]. There are many different percolation models, including bond, site, and continuum percolation [78, 79]. This section describes continuum percolation and then discusses how continuum percolation with tunnelling can model the conductance of PASNs.

Continuum Percolation

To intuitively understand continuum percolation, consider a square of concrete on a rainy day. Before any rain falls, the surface of the concrete is completely dry. Once the rain starts, droplets will begin to randomly fill the concrete square until the entire surface is covered. Continuum percolation is concerned with the proportion of square that must be covered before a path of rain drops connects two opposite sides.

The key parameter for this percolation problem is the fraction of surface covered by rain drops, p. Figure 1.6 (a-c) shows the concrete square for different values of p. For an infinitely large square, there will be a continuous pathway between opposite sides when p is greater than the critical coverage of $p_c \approx 0.68$ [76, 80]. p_c is referred to as the percolation threshold.

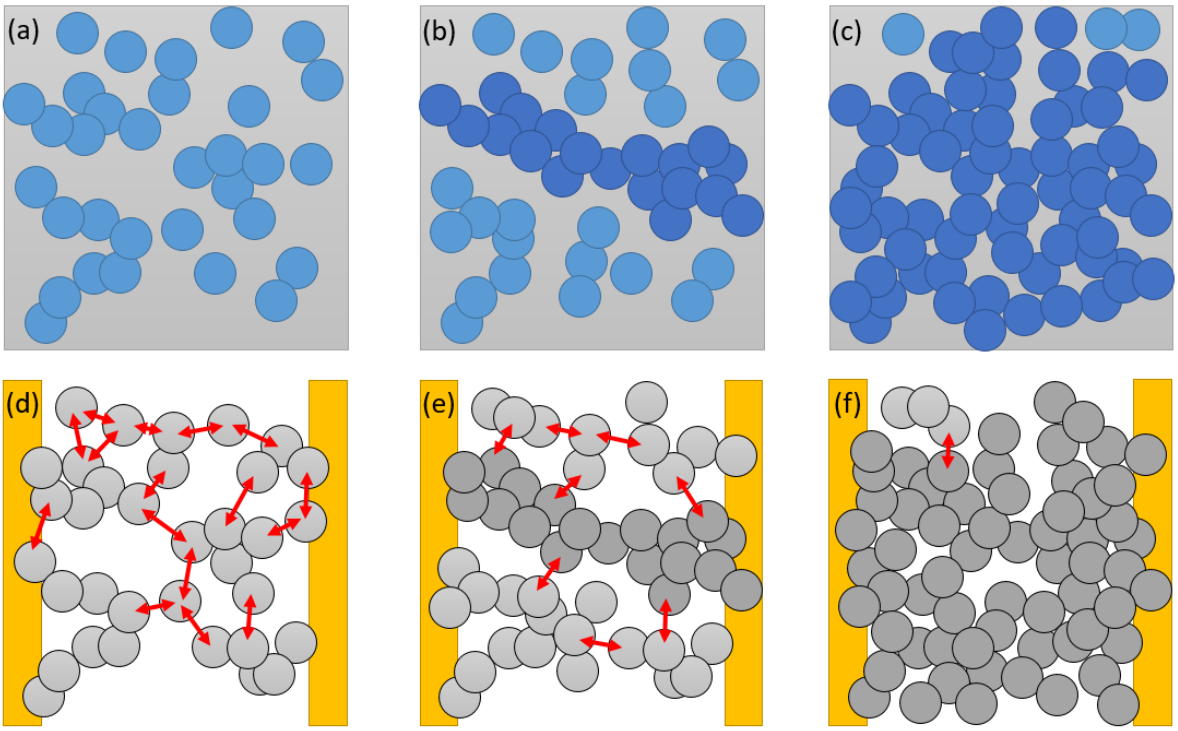

Figure 1.6: *(a-c) A concrete square with different proportions, p, of its surface covered by rain drops. (a) $p < p_c$, no pathway exists between two opposite sides. (b) $p \approx p_c$, two opposite sides of the square are connected. (c) $p > p_c$, many paths exist across the square. (d-f) Continuum percolation with tunnelling at various surface coverages, p. Red arrows indicate quantum tunnelling between nearby, unconnected NP groups. (d) $p < p_c$, there is lots of tunnelling and no pathway across the system. (e) $p \approx p_c$, a conductive path spans the network and there is less tunnelling. (f) $p > p_c$, there are many paths across the system and very little tunnelling.*

Formally, continuum percolation randomly places discs of diameter d (here, $d = 1$ for simplicity) throughout an $L \times L$ area. The critical feature of continuum percolation is the discs can overlap with one another, exactly as in the rain drop problem [79]. p remains the fraction of surface area covered by discs, and p_c is the percolation threshold.

Continuum Percolation with Tunnelling

Continuum percolation *with tunnelling* can model the conductance of PASNs as they are deposited [76, 77]. PASNs are fabricated through deposition of tin nanoclusters between gold electrodes on a substrate. Nanoclusters can coalesce with nearby nanoclusters to form NPs. Electrical conductance can occur through Ohmic connections between NPs that overlap. Additionally, conductance can occur through quantum mechanical tunnelling across small gaps (tunnel gaps) between NPs. Conductance is significantly greater across Ohmic connections than across tunnel gaps. The model approximates the NPs as 2D discs that can overlap, while the gold electrodes mark the boundary of the deposition region.

When the deposition begins, tin NPs arrive on the substrate and begin to overlap with one another as more material lands on the substrate. At this stage, $p < p_c$ and conductance between the electrodes is only possible through tunnelling (Figure 1.6 (d)). When p ~p_c, a

group of overlapping NPs connects the electrodes and the conductance is dominated by this pathway, however some tunnelling remains (Figure 1.6 (e)). At higher coverages, $p > p_c$, many conducting paths connect the electrodes while very few tunnelling paths exist (Figure 1.6 (f)).

When $p \approx p_c$, the network undergoes a phase transition from an insulating state to a conducting state, as a connected path of NPs now exists between the electrodes [13, 16, 71]. All PASNs reported in this thesis are poised slightly above the percolation threshold.

1.2.3 Atomic Switches

It has been demonstrated that atomic scale switches can be formed across a nanoscale gap between fixed silver sulphide and platinum electrodes [81]. Experimental and simulation results provide strong evidence that similar atomic bridges, or filaments, form in the tunnel gaps of a PASN when a sufficient bias is applied across the electrodes [13,18]. The formation of these atomic scale filaments creates new conductive pathways between NP groups, which leads to sudden changes in the network conductance. Furthermore, it has been shown that these filaments can break, which causes an Ohmic connection to become a tunnel gap, and for network conductance to abruptly change. The formation and destruction of atomic filaments in tunnel gaps is called atomic switching [13].

The mechanism behind the formation of atomic filaments in PASNs is attributed to electric field induced surface diffusion (EFISD) and electric field induced evaporation (EFIE) [13]. EFISD causes the surface atoms of a solid to migrate under sufficient electric fields (E $>$ 1 V/nm in tin) [82]. EFIE causes the ionisation and emission of surface atoms from a metal under strong electric fields (E $>$ 26 V/nm in tin) [83].

When sufficient voltage is applied between the electrodes of a PASN, the electric field in some tunnel gaps is strong enough to pull surface atoms into the gap via EFISD. These surface atoms form a protrusion which effectively shrinks the tunnel gap, and leads to stronger electric fields in the gap. When the electric field exceeds the threshold for EFIE, atoms begin to ionise and are ejected from the surface of one atom to form a protrusion on the opposite side of the tunnel gap. When the two protrusions connect, they form a single atomic scale filament that supports Ohmic conduction [71]. Figure 1.7 demonstrates the filament formation process.

The formation of atomic scale filaments replaces tunnel gaps with Ohmic conduction pathways. However, these filaments are extremely small and experience high current densities that cause filaments to break from electromigration [13]. Electromigration is the drift of atoms under high current densities due to the force of collisions with electrons. In tin, electromigration occurs when the current density exceeds ~2×10^8 A/m^2 [84], which frequently occurs in experiments on PASNs. The destruction of a filament due to electromigration changes an Ohmic conductance pathway into a tunnel gap.

Whenever a filament forms or breaks, the conductance (G) of the network changes. This change in G is referred to as a *switching event*, or simply as an *event* or *switch*. The change in conductance (ΔG) due to an event is called the size of the switching event. Every switch causes the redistribution of electric fields and current densities throughout the network, which stimulates switching events in other tunnel gaps. Therefore, switching events are correlated.

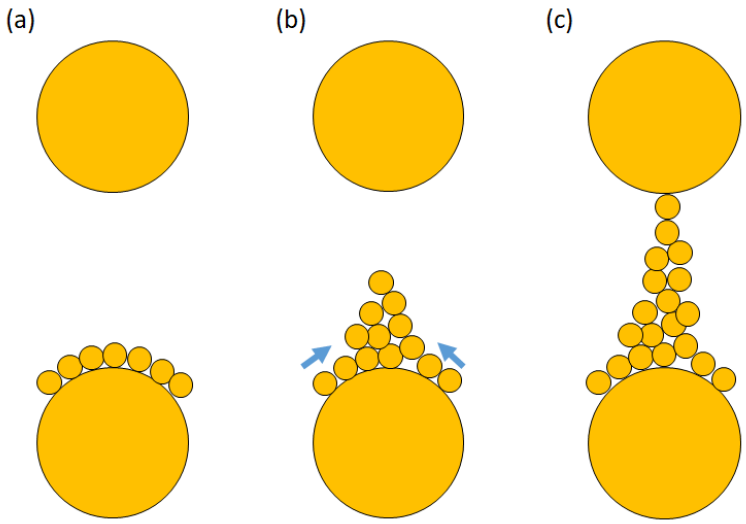

Figure 1.7: *Schematic of atomic filament formation. (a) Before threshold voltage is applied. (b) With a sufficient electric field across the gap, the surface atoms diffuse to form a protrusion (EFISD). (c) The protrusion decreases the gap size and increases the electric field to cause a jump to contact, which forms an atomic filament (EFIE).*

Studies on the dynamics of these switching events have drawn remarkable similarities to neuronal dynamics in the brain (Section 1.2.4) [15–17].

1.2.4 PASN Research

Significant research has been conducted into the properties of PASNs and their suitability for neuromorphic computing [13–18]. This section briefly summarises the key results to date.

Switching Activity Basics

Quantised conductance and switching events have been observed in PASNs [13]. Simulation and experimental analysis strongly suggest that the switching activity is a result of the formation and destruction of atomic-scale wires in tunnel gaps between nanoparticles (Section 1.2.3).

Switching events require a critical voltage to activate, and the rate of switching events increases as applied voltage exceeds the critical value [14, 15]. Figure 1.8 demonstrates the critical threshold voltage of a PASN when voltage pulses are applied across the electrodes. The switching dynamics are similar regardless of the polarity of the applied voltage [14]. This polarity independence rules out other switching processes such as Coulomb charging and redox reactions [65], and further supports the electric-field and current-induced switching processes described in Section 1.2.3.

Initial devices fabricated in [13] were unstable, and could only support switching activity for several hours. To improve device stability, oxygen and moisture are carefully introduced during nanocluster deposition [14]. The increased humidity accelerates the oxidation of tin to tin oxide, and this oxidation causes a reduction in nanocluster coalescence. Reduced

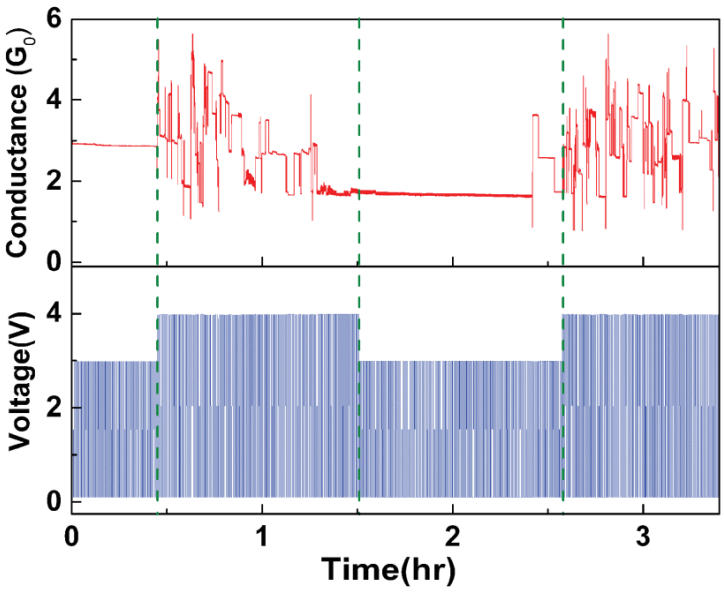

Figure 1.8: *Example of critical voltage for switching activity to activate in PASNs. Application of 3V pulses across the electrodes leads to very few switching events over several hours, whereas 4V pulses leads to many switching events. Reproduced from [14] ©2017IEEE.*

coalescence of nanoclusters leads to increased stability of the network morphology. These stable networks exhibit switching activity for several months [14].

The oxidation process introduces non-negligible resistance to Ohmic connections within the network [15]. As a result, whenever a switching event occurs the rest of the network can be approximated as an equivalent circuit with some series and some parallel resistance. Despite the switching event itself having quantised conductance, the overall change in network conductance is not necessarily quantised, because of the complex parallel and series connections in the network [15, 17, 18].

Network Structure

Scanning electron microscope (SEM) images of PASNs demonstrate the fractal geometry of the networks (not shown). Additionally, simulations of PASNs (see Section 2.5), show that the number of connections between NPs, or the degree of each NP, is distributed as a power law [17]. This distribution means several NPs form connections to many other NPs in the network, and can support global connections throughout the network. Further analysis of experiments and simulations indicate PASNs have high clustering coefficients, and low average path lengths in a hierarchical structure. All of these structural properties are similar to neural-networks in the brain (Section 1.1.2) [35, 36].

Network Characteristics

A histogram of the changes in conductance from switching events (Figure 1.9 (B,E)) is heavy tailed, and shows that the size of switching events varies over several orders of magnitude. The size of a switching event depends on the location of the switch, and the overall configuration of the network [17]. A switching event located at a 'low-order branch' of the network

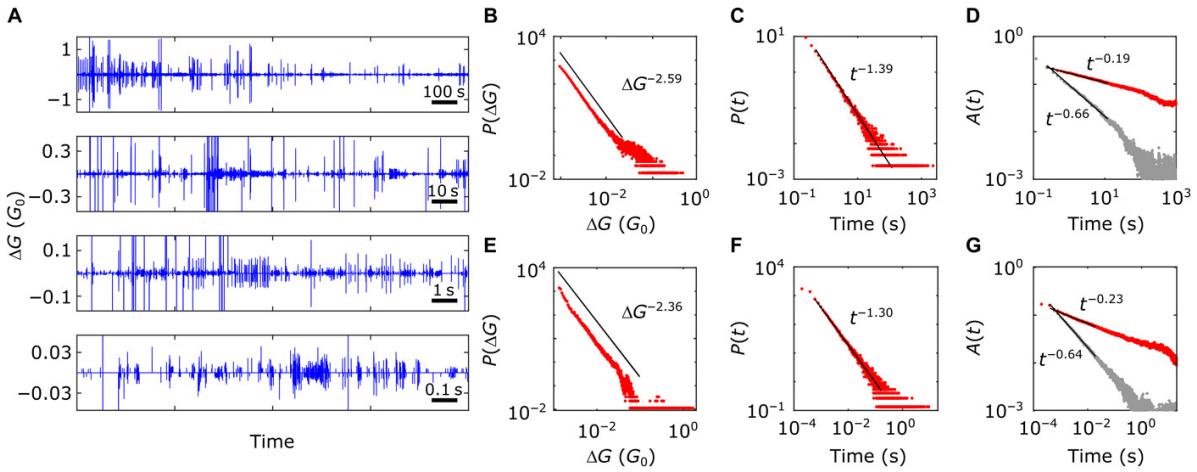

Figure 1.9: *Switching dynamics of PASNs. (A) PASNs exhibit qualitatively similar switching activity across many temporal scales. The top panel shows 2400s of data and each panel below has 10, 100, and 1000 times greater magnification in time, while the vertical scales have 3, 9, and 27 times greater magnification. (B-D) Measured from one sample while (E-G) are from a second sample with a 1000 times faster sampling rate. (B,E) demonstrate probability density functions for changes in total network conductance, P(ΔG). The distribution is heavy-tailed and ΔG varies over several orders of magnitude. (C,F) IEI distributions follow a power law, indicating PASNs demonstrate scale-free dynamics. (D,G) ACF for the real IEI data (red) decays as a power law over several orders of magnitude. In contrast, the ACF for shuffled IEIs (grey) destroys any correlations between IEIs and the ACF declines relatively steeply. These results strongly suggest there are long-range temporal correlations between switching events. Reproduced from [16] under creative commons licence (CCL): CC BY-NC (https://creativecommons.org/licenses/by-nc/4.0).*

- that is, a part of the network with few parallel pathways - will lead to large changes in the network conductance. Meanwhile, a switching event at a 'high order' branch - part of the network with many parallel connections - will cause a smaller change in network conductance. Moreover, each switching event causes the current through the network to redistribute, which can change the branch that a switching site is on. Therefore, a single switching site, or tunnel gap, can cause different changes in network conductance because of the affect of other switching events on the network. [18].

PASNs exhibit qualitatively similar switching activity across many different time-scales, as shown in Figure 1.9 (A) [17]. This self-similarity is a strong indicator of temporal correlations between switching events on a range of scales. An investigation of the times between consecutive events, referred to as the inter-event-intervals (IEIs), unveils the IEIs have a power law distribution (Figure 1.9 (C,F)), which indicates the network has scale-free dynamics [16, 85]. See Section 3.3.3 for further details of IEI analysis.

The auto-correlation function (ACF) measures the correlations between the IEIs of real data and a lagged version of itself. The greater the ACF amplitude, the greater the strength of correlations in the data [86]. In PASNs, the ACF (red line) is a power law (Figure 1.9 (D,G)) that slowly declines over several orders of magnitude. When the IEIs are shuffled (grey), all correlations are destroyed and the ACF declines significantly faster than the real data. The power law ACF with greater correlations than shuffled data strongly indicates

that PASNs exhibit long-range temporal correlations (LRTCs) [17].

Finally, PASNs exhibit dynamics that rigorously meet criteria for criticality [16]. Critical systems are characterised by avalanche dynamics, that is, any one event can cause a cascade of subsequent events. There is significant evidence that the brain is a critical system, and that this criticality optimises dynamic range, information transmission, and information capacity [87]. In PASNs, criticality was shown through analysis of avalanche sizes, durations, and shapes [16]. Criticality is required for RC and so these results show PASNs are a potential platform for RC [16]. See Section 3.3.4 for further information on the avalanche analysis.

1.3 Thesis Aims and Structure

This chapter has introduced the concepts of neuromorphic computing and described its potential to replicate the energy efficiency and computational capabilities of the brain (Section 1.1). Percolating atomic switch networks were then discussed in Section 1.2 as a promising neuromorphic architecture that demonstrates switching activity with brain-like dynamics. This section outlines the research goals for this thesis and presents the thesis structure.

The results discussed in Section 1.2.4 focus on PASN devices with two-electrodes (2T). These devices allow for easy measurement of the total network conductance and any switching events that occur. However, RC requires multiple inputs and outputs to succeed [16]. Therefore, PASNs with multiple electrodes (MC) are required, and are the focus of this thesis.

This thesis presents data for MC devices that I fabricated. The first aim of the thesis is to establish the switching activity of MC devices is similar to the switching activity of 2T devices. The second aim is to use data from the multiple electrodes to demonstrate that PASNs exhibit complex patterns of switching activity.

Chapter 2 details the materials and processes used to fabricate and analyse PASNs. Chapter 3 introduces MC device data and compares the switching activity to data measured with 2T devices. The remainder of the thesis investigates the complexity of PASNs with different tools. First, Chapter 4 presents a qualitative analysis of the correlations in switching activity measured on different electrodes. Next, Chapter 5 quantifies the complexity between switching events with neural complexity [1]. Chapter 6 summarises the results, outlines limitations of the analysis, and describes future research with PASNs.

Chapter 2

Materials and Methods

This chapter details the materials, equipment, and processes used to fabricate and analyse PASNs in this thesis. Section 2.1 describes the properties of tin and how these properties change in tin NPs. Section 2.2 details the silicon nitride substrates and how they are prepared for deposition. Section 2.3 discusses the deposition system and the process for PASN fabrication. Section 2.4 explains the equipment for electrical characterisation. Finally, Section 2.5 details how simulations of PASNs were generated for comparison to the physical networks.

2.1 Tin

PASNs in this thesis consist of nanoparticles of tin (Sn). Tin is a malleable metal that resides in group 14 of the periodic table. There are two main oxidation states for Sn, the +2 state and the more stable +4 state. It has the magic atomic number of 50 which provides enhanced stability, as evidenced by the 10 stable isotopes of Sn [88, 89]. There are two common allotropes of tin (at room temperature and atmospheric pressure) known as grey tin (α-Sn) and white tin (β-Sn). β-Sn is stable above 286.3K (13.2 °C), has a silvery-white colour, metallic behaviour, and a body-centred tetragonal structure. In contrast, α-Sn is stable below 286.3K, has a grey colour, exhibits no metallic behaviour, and has a diamond cubic structure. Below 286.3K, β-Sn spontaneously transitions into α-Sn.

Metallic tin oxidises in atmosphere to form a layer of SnO_2 on the surface. The oxide layer protects the bulk Sn from further oxidation [90], and it has been demonstrated that the oxidation process is accelerated in humid conditions [91]. In tin NPs, the thickness of the oxide layer depends on the size of the NPs, and NPs that are smaller than ≈20nm can be fully oxidised, leaving no Sn core behind [92]. Therefore, it is essential that oxygen partial pressure and humidity are controlled during deposition so the Sn NPs are partially oxidised. The partial oxidation creates stable networks with metallic behaviour [14].

2.2 Substrates

PASNs are deposited onto silicon (Si) wafers with a 200nm silicon nitride (Si_3N_4) passivation layer. Si_3N_4 is an excellent substrate for microelectronics due to its high thermal

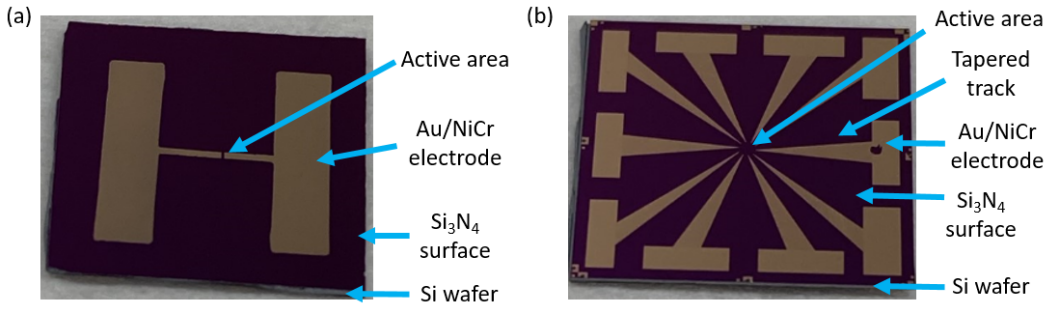

Figure 2.1: *(a) Photograph of a Si_3N_4 substrate with two electrodes (2T) fabricated in the shape of an 'H'. These substrates were used for previous PASN analysis. (b) Photograph of a Si_3N_4 substrate with 10 electrodes fabricated around the substrate perimeter. These multi-electrode (MC) substrates were used for the PASNs studied in this thesis.*

conductivity, chemical stability, and hardness [93]. Moreover, it is extremely smooth which allows for coalescence of Sn nanoclusters on the surface. Additionally, Si_3N_4 is an electrical insulator which prevents current flow to the Si wafer, thus ensuring all current flows through the PASN.

To sample the electrical conductivity of the PASNs, gold (Au) electrodes were deposited on the Si wafer. These electrodes are made from a 5nm thick layer of nichrome (NiCr) and a 45nm thick layer of Au. The NiCr layer is used to increase adhesion of the Au to the Si_3N_4. Previous devices had two electrodes (2T) in the shape of an 'H' (Figure 2.1 (a)) that were fabricated by thermal evaporation with a shadow mask [71]. The devices investigated in this thesis have 10 electrodes (MC) that are equally spaced on the perimeter of a circle with 600μm diameter (Figure 2.1 (b)). Each electrode has a track to a contact pad on the perimeter of the substrate. There is the potential for 20 electrodes with the substrate design in Figure 2.1 (b), however only 10 electrodes were used in this thesis as an initial study. The electrodes were fabricated with photolithographic processes, thermal evaporation, and lift-off techniques [94]. The additional electrodes aim to characterise different regions of PASNs. Further detail on the fabrication of the electrodes can be found in [95].

After electrode fabrication, the substrates were cleaned using acetone to remove surface contamination and then rinsed in isopropyl alcohol (IPA). Immediately after the IPA rinse, the substrates were blow dried with 99.99% nitrogen and checked under an optical microscope for any contamination. If the surface was clean, then the substrate was loaded onto the sample holder for deposition.

2.3 Deposition System

An ultra-high-vacuum (UHV) cluster deposition system was used to deposit tin nanoclusters onto the silicon nitride substrates [74]. Figure 2.2 shows the system with labels for the three main chambers: the source chamber, mass selection chamber, and deposition chamber. The system is connected to several pumps that create a pressure gradient that propels nanoclusters from the source chamber to the deposition chamber. The following sections describe each chamber and the types of pumps used. Further detail about the deposition system can be found in [96].

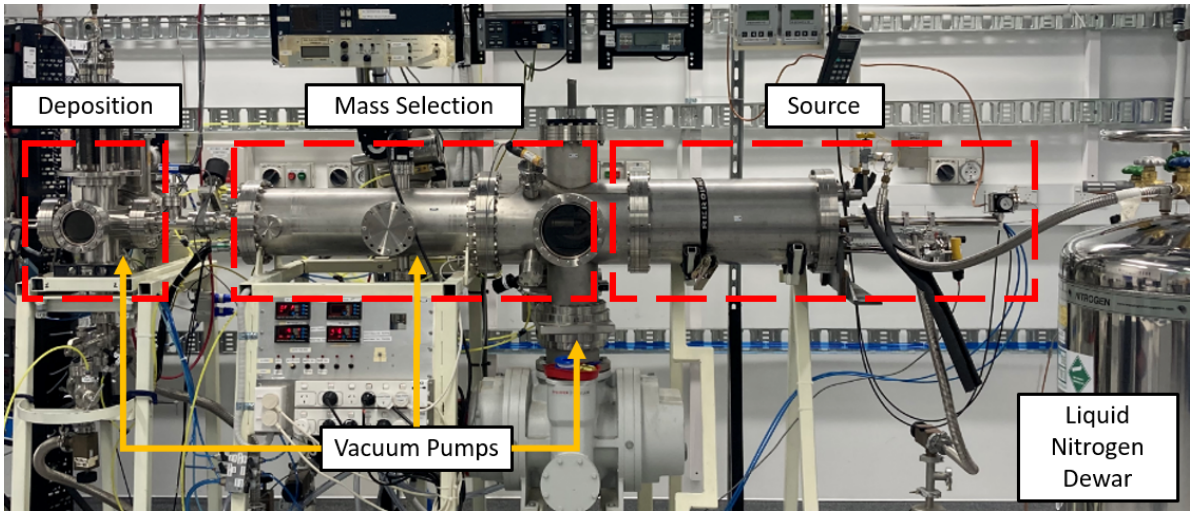

Figure 2.2: *Photograph of the deposition system. Tin NPs are produced at the source and travel towards the substrate in the deposition chamber. The vacuum pumps create the pressure gradient that facilitates movement.*

2.3.1 Pumping System

Nanoclusters travel from the source chamber to the deposition chamber because of a pressure gradient. Three pumping stages create this gradient and maintain an ultra clean environment for deposition. This section describes the different types of pumps used in the deposition system. Further details on pumps can be found in [97].

Rotary pumps are used to produce a rough vacuum ($\sim 1 \times 10^{-3}$ Torr) and are used for backing of the roots and turbo molecular pumps. Roots pumps are used to remove large volumes of gas very quickly and efficiently, which is required to remove the argon injected into the source (Section 2.3.2). Turbo molecular pumps are used to produce UHV as low as $\sim 1 \times 10^{-10}$ Torr. The turbo molecular pumps are water cooled to prevent overheating.

2.3.2 Source Chamber

The source chamber holds a magnetron sputter head [98], a liquid nitrogen (LN_2) cooling system, an inert argon (Ar) source, a nozzle, and a skimmer. Figure 2.3 shows a schematic of the source chamber. The magnetron sputter source houses a high-purity metallic disc, called a target, that produces the nanocluster material. In this thesis, a target of 99.999% pure β-Sn with a diameter of 50mm and depth 6mm was used. Note that other target materials can be used to produce nanoclusters [75].

Ar gas flows into the chamber near the target at a controlled rate. A high DC bias is applied to the target, and the Ar atoms are ionised by the electric field. The Ar^+ ions create a plasma near the target surface. The Ar^+ ions are rapidly accelerated towards the negatively charged target and bombard the its surface, which transfers energy to the surface atoms. If the transferred energy is greater than the binding energy, atoms will be sputtered from the target surface [99]. A permanent magnet is attached to the back of the target which produces a magnetic field. This magnetic field traps any secondary electrons that are produced from the target bombardment or the Ar ionisation, and forces them to move in

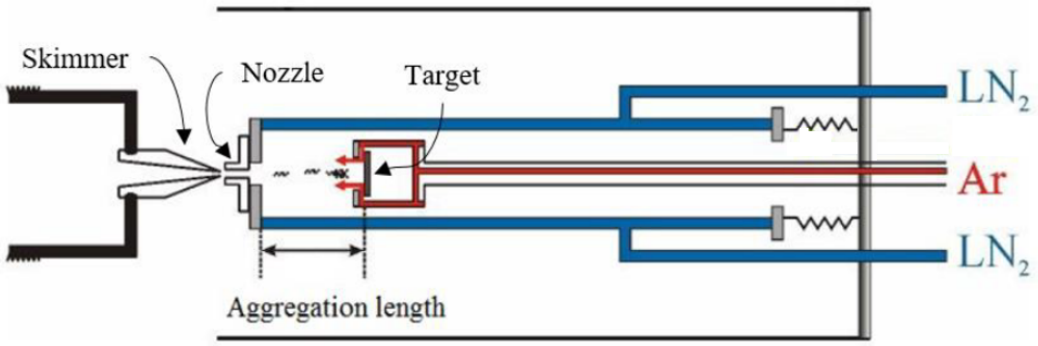

Figure 2.3: *Schematic of the source chamber. Ions and secondary electrons bombard the target to eject surface atoms. These atoms are carried by the inert gas to the nozzle and coalesce into nanoclusters by IGA as they travel the aggregation length [75].*

helical trajectories near the target. The confinement of the secondary electrons increases the rate of Ar ionisation and creates a dense plasma that can be operated at lower pressures and voltages than a plasma without the secondary electrons. The surface bombardment generates high temperatures, and so LN_2 flows through cooling lines to prevent the target from melting. Additionally, water lines run to the gasket at the back of the target to prevent it from freezing and developing a leak.

The Ar gas flows from the target to the nozzle because of the large pressure difference between the source chamber and the mass selection chamber. Sputtered atoms are carried by the Ar and coalesce together by IGA as they move towards the nozzle (labelled the aggregation length in Figure 2.3). The Ar gas is cooled by LN_2 which causes the Sn atoms to be rapidly cooled and supports nanocluster formation [74]. The aggregation length can be externally adjusted and is a key parameter in determining the size of the produced nanoclusters. A longer aggregation length allows more time for coalescence and therefore increases the size of the nanoclusters. The nanocluster size can also be tuned through adjustment of the Ar flow rate and the DC bias of the target.

2.3.3 Mass Selection Chamber

Nanoclusters produced in the source chamber exit through the nozzle to a differential pumping chamber before passing through a skimmer (Figure 2.3) to the mass selection chamber. The differential pumping stage is pumped by a roots pump that is backed by a rotary pump, which removes the majority of Ar gas. The nanoclusters have significantly more momentum than the Ar, and can continue with the same trajectory through the interconnecting stage.

The nanoparticles exit the nozzle in a cone shaped jet with the heaviest nanoclusters near the axis of the cone, due to the shape of the nozzle and the pressure difference between the source and interconnecting chambers. The skimmer [74] shapes the nanoclusters that enter the mass selection chamber into a collimated beam. It is essential the skimmer is correctly aligned with the nozzle, as small misalignments can dramatically change the nanocluster size distribution. The skimmer and nozzle alignment can be externally adjusted.

The mass selection chamber houses a Palmer-Issendorff mass selector [100], and is pumped down by a turbo molecular pump with a backing rotary pump. Figure 2.4 shows a schematic

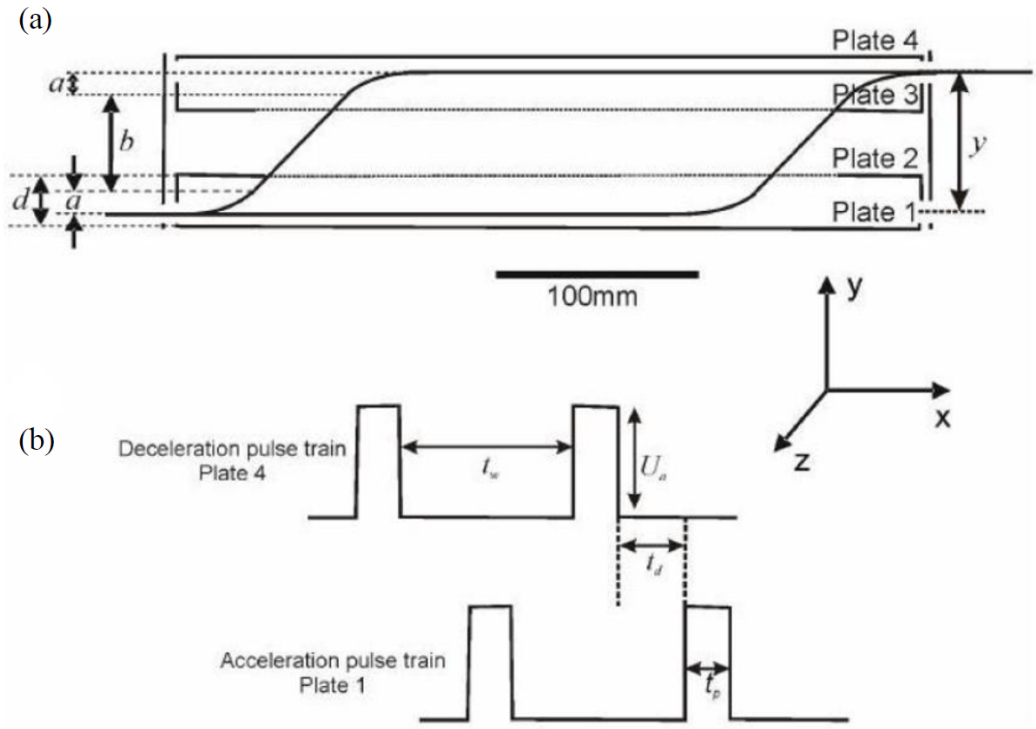

Figure 2.4: *(a) Schematic of the Palmer-Issendorff mass selector. The nanocluster beam travels in the x-direction between plates 1 and 2. A voltage pulse applied between these plates causes charged nanoclusters to accelerate in the y-direction. These nanoclusters travel upwards through holes in the plates until the y-direction velocity is removed by a voltage pulse between plates 3 and 4. The nanoclusters travel the distance a during the pulse and the distance b between pulses. (b) Applied voltage pulse timing. Pulse duration is t_p and delay between pulses is t_d [75].*

of the mass selector, which consists of four plates that are parallel to the nanocluster beam. The nanoclusters exit the skimmer and enter the space between plates 1 and 2. A fraction of the nanoclusters are ionised and are subject to Lorentz forces as they move through an electric field. A voltage pulse is applied between plates 1 and 2 which accelerates these ionised nanoclusters in the y-direction. The heavier nanoclusters gain smaller vertical velocities than the lighter nanoclusters. The ionised nanoclusters then travel in the y-direction through holes in plates 2 and 3. A second voltage pulse is applied between plates 3 and 4 which has equal magnitude and duration to the first pulse, except in the opposite direction. This second pulse removes the y-direction velocity of the nanoclusters and allows the nanoclusters to travel in the x-direction and leave the mass selector. Only nanoclusters of a narrow size range can exit the mass selector between plates 3 and 4 for any given set of pulse magnitude, U_p, time between pulses, t_d, and pulse duration, t_p.

In this thesis, the mass selector was used to analyse the size distribution of the nanocluster beam before deposition of each PASN. To achieve this, a Faraday cup was positioned at the end of the aperture after plates 3 and 4. The Faraday cup measures the number of nanoclusters that exited the aperture between plates 3 and 4, by measuring the induced current produced when charged nanoclusters make contact with the cup and become neutral. Adjustment of the time between voltage pulses changes the sizes of nanoclusters that reach the Faraday cup. A mass spectrum is generated by comparing the relative number of

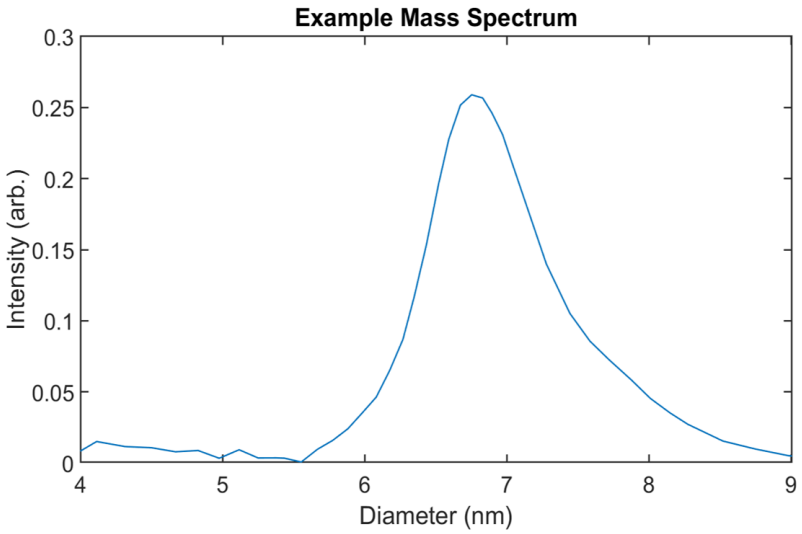

Figure 2.5: *Standard mass spectrum of the Sn nanocluster beam. The distribution has a peak centred around nanoclusters with 7nm diameter.*

nanoclusters for each time between voltage pulses. Figure 2.5 shows a typical mass spectrum for the nanocluster beam, with a peak centred near 7nm.

2.3.4 Deposition Chamber

The nanocluster beam exits the mass selection chamber, and enters the deposition chamber. Figure 2.6 shows a schematic of the deposition chamber. Inside, there is a Janis ST-400 cold finger cryostat with the prepared substrates (Section 2.2) mounted to it. Figure 2.7 shows a photograph of the cryostat. There is an external linear translator attached to the deposition chamber which allows the vertical position of the cryostat to be adjusted. The bottom of the cryostat has three sample mounts, two of which are designed for multiple electrode substrates while the other mount can only hold two-electrode substrates. Each mount has electrical contacts that are used for in-situ electrical characterisation of the devices.

There is a Sycon Instruments STM-100/FM film thickness monitor (FTM) positioned at the back of the deposition chamber. This FTM is used to measure the rate that Sn is deposited onto a substrate. However, the deposition rate cannot be measured during deposition because the FTM is blocked by the substrates. Instead, the rate is measured immediately before and after the deposition of each substrate. The rate can be tuned through adjustment of the target bias, and is typically set to ~0.2Å/s.

The deposition chamber is held at the lowest pressure in the system. A turbo molecular pump with a backing rotary pump maintain the UHV. During deposition, moist synthetic air is leaked into the chamber through a needle valve. Moisture is added to the synthetic air as it passes through a custom built bubbler that is filled with distilled water. The moist air oxidises the surface of the Sn and restricts coalescence. Careful control of the leaked synthetic air is essential to create stable PASNs that exhibit switching activity [14].

A gas-powered interlock can isolate the deposition chamber from the mass selection chamber and cuts off the nanocluster beam in-between depositions. The deposition process begins with the interlock closed. The cryostat is then lowered until one of the three substrate

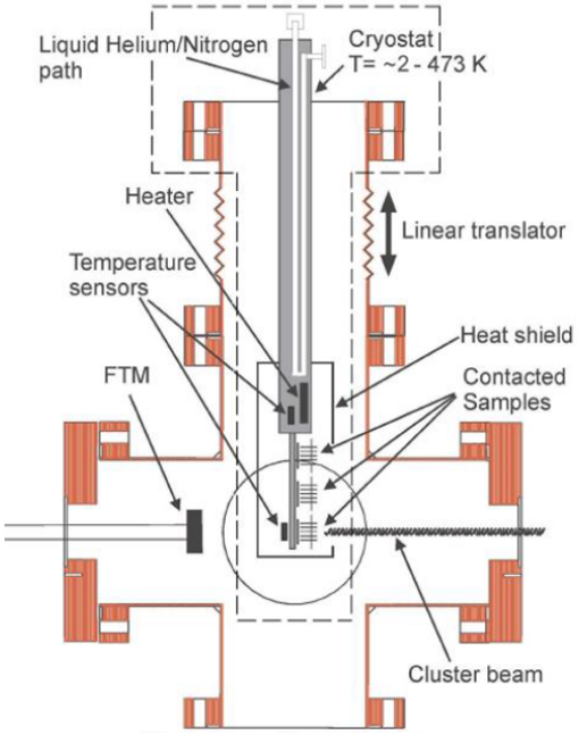

Figure 2.6: *Schematic of the deposition chamber. The nanocluster beam enters the chamber and is deposited onto the substrate [75].*

mounts is aligned with the centre of the nanocluster beam. Next, the interlock is opened and the nanoclusters are deposited between the electrodes of the substrate (active area in Figure 2.1). The resistance across the electrodes is measured throughout the deposition. For the MC substrates, one electrode has 100mV bias applied and the other nine electrodes are grounded. In the 2T substrates, one electrode is at 100mV bias while the other electrode is grounded. For both types of substrate, there is no current flow through the network until the surface coverage reaches the percolation threshold (Section 1.2.2). At the percolation threshold, the measured current sharply increases and this point is referred to as the onset of conduction. The deposition continues for 2T substrates until the measured network resistance is 2kΩ. For the MC substrates, each electrode is connected to the network (onsets) at a different time because the nanocluster deposition is random. However, the onset times are roughly similar for each electrode. The deposition is allowed to continue until either all electrodes have onset, or the resistance of one electrode is less than 500Ω. It is common for one or two electrodes to fail to connect to the network in a deposition. Deposition is stopped by closing the interlock and cutting off the nanocluster beam.

After all three depositions are completed, the interlock is closed and the PASNs remain in vacuum in the deposition chamber for electrical characterisation.

2.4 Electrical Measurements

This section describes the electrical measurement process for MC PASNs. Details of 2T PASN measurements with the same equipment can be found in [71]. The electrical prop-

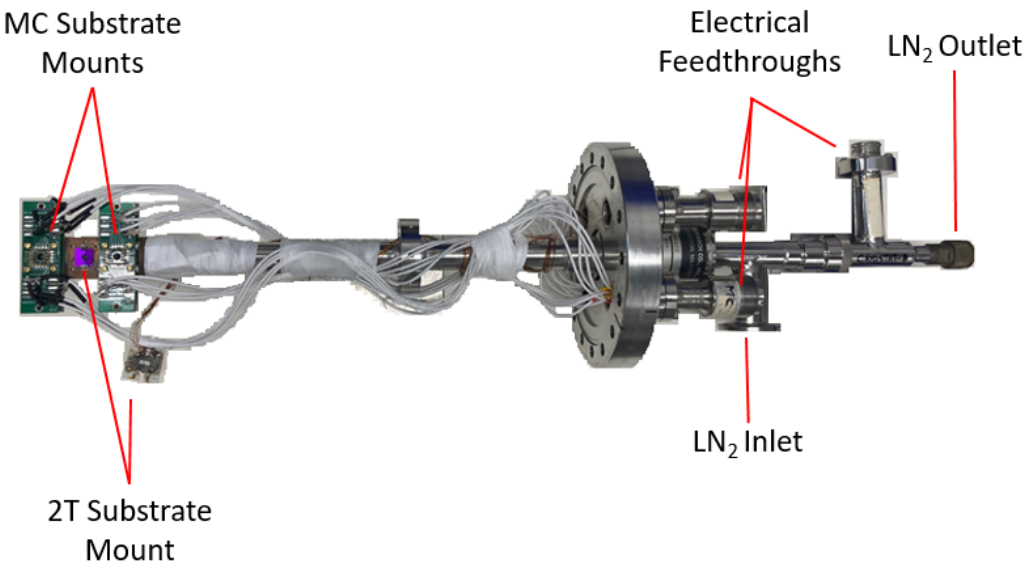

Figure 2.7: *Photograph of the Janis ST-400 cryostat used in this thesis with components labelled.*

erties of fabricated PASNs were probed *in-situ* by applying a voltage, V, to one (several) electrode(s) and measuring the current, I, through the other electrode(s). All measurements in this thesis were performed using a National Instruments PXIe-6378 ADC[1]/DAC[2]. This system is referred to as the *NI* throughout this section.

The PASNs were connected to the NI using 50Ω impedance coaxial cables with BNC[3] connectors. The NI has four DAC channels and 16 ADC channels that can measure voltage at up to 3.5 MHz. Each of the DAC channels can be programmed to output different voltage waveforms, although only DC voltage was used in this work. The NI is controlled using a custom LabVIEW GUI. The ADC channels have 16-bit resolution and measure within the range of -10V to +10V.

The input electrode(s) were connected to the DAC channels. An ADC channel was used to measure the input voltage (not a voltage across a resistor). All other electrodes (the output electrodes) were connected to 1kΩ resistors. The ADC channels were connected in parallel to the resistors and measured the voltage across the resistors. The measured voltage infers the current through the electrodes of the PASN by Ohm's Law $I = V/R$. Overall, the voltage of the input electrodes was measured simultaneously with the current through the output electrodes.

2.5 Simulation Overview

A detailed simulation of PASNs has been developed at the University of Canterbury [18]. Different simulation parameters can be quickly adjusted and measured for comparison to the experimental results. This section briefly describes how the simulations are generated and a

[1]Analogue to digital converter
[2]Digital to analogue converter
[3]Bayonet Neill-Concelman

more detailed description is provided in [101].

The simulation models PASNs as a 2D plane that is filled with randomly positioned discs of equal size that can overlap [76, 77]. These discs represent the tin NPs. The discs are placed according to a random seed, and continue to be placed until the desired proportion of the surface is covered by discs. Any discs that overlap are treated as a single group, analogous to coalesced NPs in the physical PASNs. If discs are not in contact but are sufficiently close then they are treated as connected by a switching junction. These junctions can alternate between a low conductance state and a high conductance state to model the filament formation/destruction in tunnel gaps of PASNs. Any groups that do not have a switching junction or physical connection to other groups, are considered isolated from the network and are ignored in the simulation. Groups that are only connected to one other group are considered to be part of the other group. The generated network models the structure of the PASNs.

Groups can be selected to act as input and output electrodes [102]. A group that acts as an input electrode has a voltage bias applied to it, whereas groups that act as output electrodes are grounded and the current through them is measured. The simulation calculates the electric field and current throughout the network and determines whether to adjust the conductance of the switching junctions. This process of calculating electric fields, currents, and updating switching junctions is called a single *time-step*.

A switching junction will shrink in size (representing filament growth) if the electric field in the junction is above a threshold value [18, 101]. The rate the junction shrinks is proportional to the electric field magnitude. When the switching junction has size zero, the conductance is changed from the low state to the high state. Similarly, a switching junction in the high state is considered to have a filament of width 1 in the gap. When the current flowing through the filament is above a threshold value, the filament width shrinks at a rate proportional to the current. The switching junction changes to the low conductance state when the filament width is zero.

Simulation parameters, such as system size, input voltage, and the electric field/current thresholds, all change the observed switching dynamics. In this thesis several simulations with different parameters are analysed for comparison with experiments. Specific details of these simulations is provided in Section 4.2.

Chapter 3

Basic Results

This chapter introduces multi-electrode (MC) device data, and establishes that the switching activity is qualitatively similar to two-electrode (2T) devices. Section 3.1 details the threshold procedure for switching event detection. Section 3.2 details the different devices, electrode configurations, and input voltages measured in this thesis. Section 3.3 briefly compares the switching activity and statistics of MC devices to 2T devices. Finally, Section 3.4 presents a short summary of this chapter.

3.1 Event Identification

When sufficient voltage is applied across a PASN, stepwise changes in the current (I) are observed (Section 1.2.4). These stepwise changes in I are attributed to the redistribution of current when a switching event occurs in the network [13]. Hence, the step-wise changes in I are called switching events, or simply events. A threshold is implemented in the analysis procedure to identify changes in I due to events, from changes in I due to noise.

Figure 3.1 (a) shows the current over 1s at two different electrodes of a typical MC device, and Figure 3.1 (b) shows the corresponding $|\Delta I|$. Each panel shows data for a different electrode. Note that the electrode identifiers ('P6', 'P20', etc.) refer to the location of each electrode on the MC device, and are explained further in Section 3.2.2. Near 301.1s and 301.5s, significant step-wise changes in I are observed at both electrodes. These changes in I are greater than the threshold in Figure 3.1 (b) (black dashed line), hence they are identified as events. All other changes in I are attributed to measurement noise.

The thresholds used for data analysis are determined with a threshold procedure. The following section describes the features of the noise which are used to motivate this threshold procedure. Section 3.1.2 then details the procedure and Section 3.1.3 shows examples of the threshold in practice.

3.1.1 Features of the Noise

Noise at Different Electrodes

Figure 3.2 (a) shows the current at three electrodes over 8s, and Figure 3.2 (b) shows the corresponding $|\Delta I|$ for the same data segment. No input voltage was applied, and so all

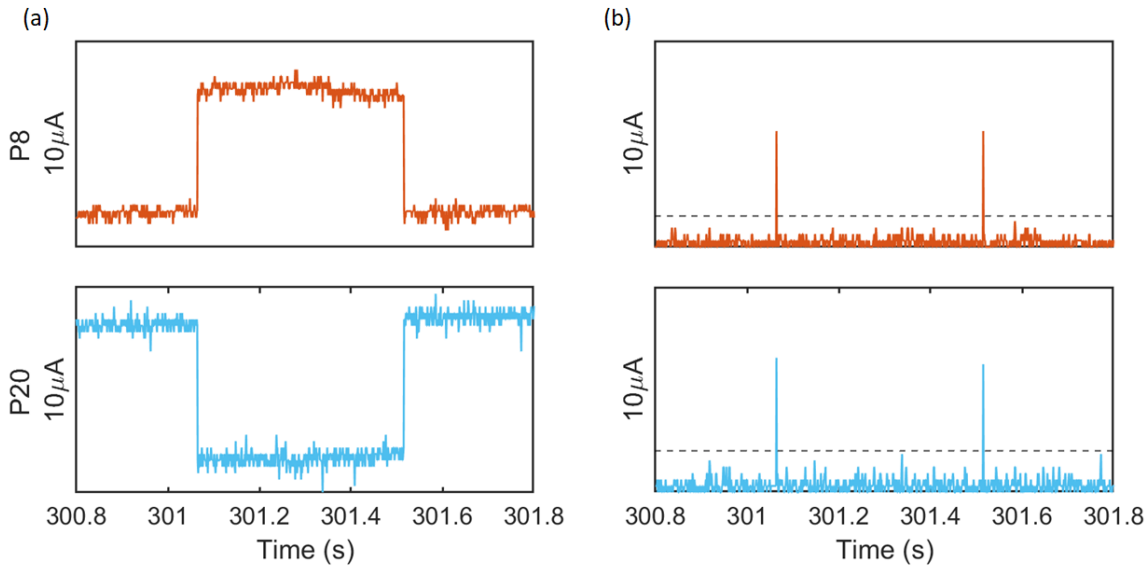

Figure 3.1: *Example of multi-electrode data at two different electrodes. All data is from a measurement of Device I with 9V DC bias applied to the input electrodes of configuration A (see Section 3.2 for device and configuration details). The sampling rate is 1kHz. (a) Each panel shows current at a different electrode with the range of I values labelled next to each panel. Additionally, the electrode identifier (e.g. 'P6') is shown next to the corresponding panel. (b) Each panel shows $|\Delta I|$ for each panel in (a), with the same labels that are used in (a). The black dashed line represents a threshold of ~2μA for each electrode.*

changes in I are due to noise.

The black lines in Figure 3.2 (b) show the largest noise fluctuation for each electrode in the data segment. Clearly, the noise is different at each electrode, with the largest noise fluctuation measured at electrode P14, and the smallest noise fluctuation at electrode P10. Therefore, a good event threshold for electrode P10 is unlikely to be a good event threshold for electrode P14. Hence, different event thresholds are required for each electrode. Note that the difference in noise between electrodes is likely due to slight differences in the resistance of each electrode, cable, and connection involved in the measurement.

Measurement Resolution

The threshold for each electrode is expressed in terms of the minimum measurable change in current (ΔI_{res}). As discussed in Section 2.4, the measurement system has 16-bit resolution across the range of -10V to +10V. Since 1kΩ resistors are applied in series, this voltage range is equivalent to a current range of -10mA to +10mA. Therefore, the minimum measurable change in current is given by

$$\Delta I_{res} = \frac{Range}{Resolution} = \frac{20mA}{2^{16}} = 0.3052\mu A \tag{3.1}$$

Figure 3.2 (c) and (d) show magnified data from the red and green rectangles in Figure 3.2 (b) respectively. Clearly, Equation 3.1 is very close to the value of ΔI_{res} in practice (~0.3126μA).

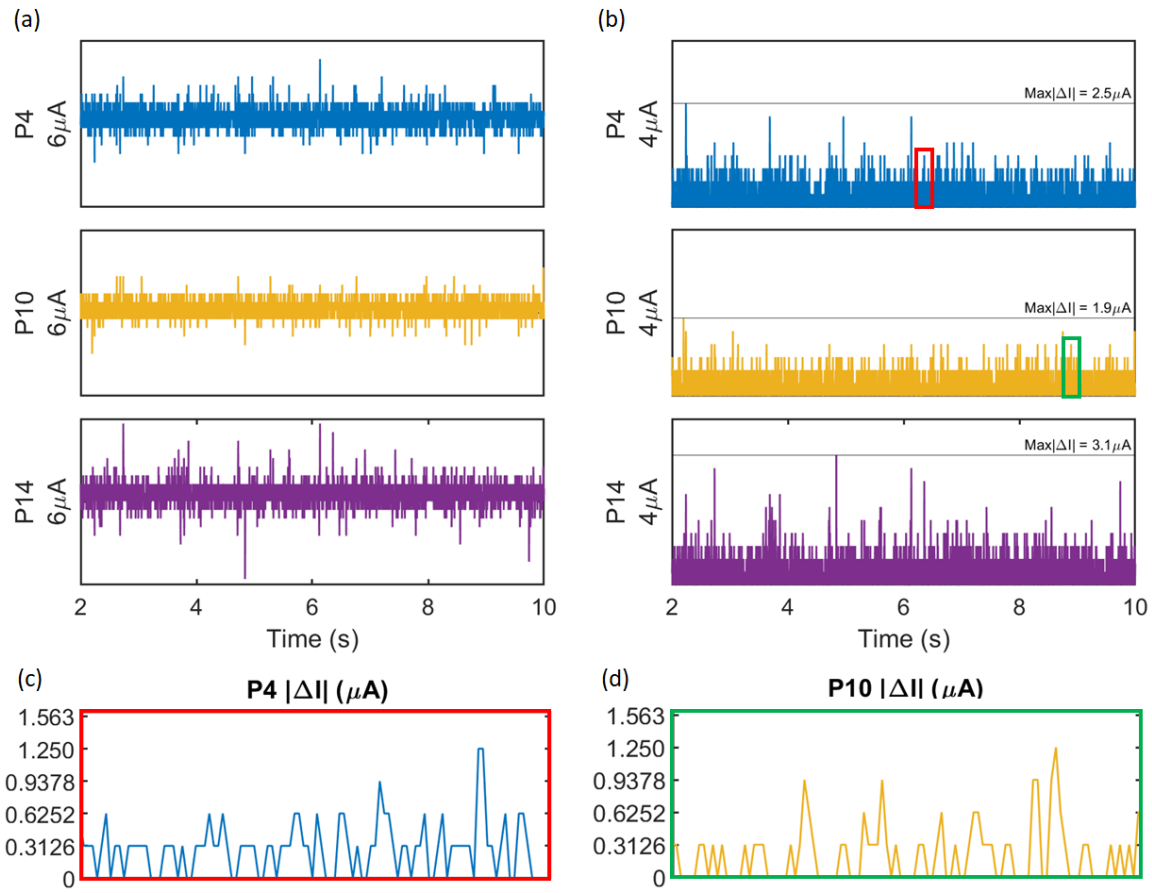

Figure 3.2: *(a,b) An 8s segment of current at three electrodes (a), with the corresponding $|\Delta I|$ (b). The data is for Device I in configuration A with no input voltage, hence all data is noise (see Section 3.2 for device and configuration details). The sampling rate of the data was 1kHz. The vertical range and electrode identifiers are labelled next to each panel. Note that the vertical scale in (b) is different to (a). In (b), the black line shows the maximum $|\Delta I|$ for each electrode. The red and green boxes are magnified in (c) and (d) respectively. (c,d) Magnification of $|\Delta I|$ for electrode P4 and electrode P10 respectively. The resolution of $|\Delta I|$ is ~0.3126μA for all electrodes.*

Voltage Dependence of Noise

Figure 3.3 (a) and (b) show $|\Delta I|$ measured for 10s at three different electrodes with an input voltage of 0V and 2V respectively. Both segments of data show only noise. The largest noise fluctuations at 2V for electrodes P10 and P14 are only very slightly larger than the largest noise fluctuations at 0V for the same electrodes. Furthermore, the largest noise fluctuation for electrode P4 is identical regardless of input voltage. Overall, Figure 3.3 (a) and (b) provide evidence that the noise does not significantly depend on the applied voltage.

3.1.2 Threshold Procedure

The threshold for a given electrode is determined by the noise observed at that electrode. Hence the threshold for event detection can be different at each electrode. Typically, the start or end of each measurement includes 2-10s of data with no input voltage (before the

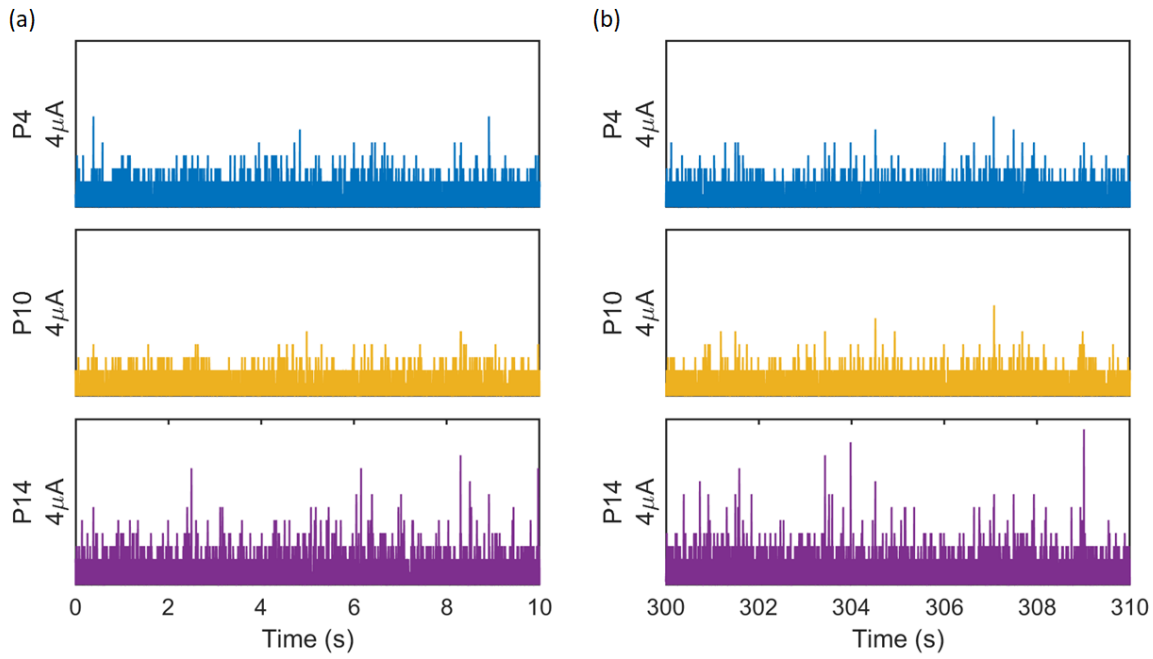

Figure 3.3: *Comparison of the measurement noise for 10s segments with different applied voltages. All data is from the same 10-minute measurement of Device I in configuration A (see Section 3.2 for device and configuration details). The sampling rate was 1kHz. (a) $|\Delta I|$ for three electrodes with no input voltage. (b) $|\Delta I|$ for three electrodes with 2V applied DC bias. The vertical scales are identical between (a) and (b).*

measurement). This 0V segment is entirely noise. Since the noise is independent of applied voltage, the maximum $|\Delta I|$ in the 0V data segment, $|\Delta I|_{0Vmax}$, is a good estimate for the maximum noise fluctuation for each electrode. Note that $|\Delta I|_{0Vmax}$ is different for each electrode. The threshold for the given electrode, $|\Delta I|_{thresh}$, is then given by

$$|\Delta I|_{thresh} = |\Delta I|_{0Vmax} + 0.5\Delta I_{res} \tag{3.2}$$

where the $0.5\Delta I_{res}$ ensures that all $|\Delta I| \leq |\Delta I|_{0Vmax}$ are treated as noise, while all $|\Delta I| > |\Delta I|_{0Vmax}$ are identified as events. This threshold procedure is consistent with the procedure implemented in [95].

The choice of threshold aims to maximise the number of true event detections, and to minimise the amount of noise incorrectly identified as events, which inevitably requires a trade off for real data. Therefore, a range of thresholds for analysis were explored. The next section shows examples of data with a range of thresholds applied to show that $|\Delta I|_{thresh}$ is a good threshold for event detection.

3.1.3 Threshold Examples

Figure 3.4 (a) shows the current at three electrodes of Device I over 3s, and Figure 3.4 (b) shows the corresponding $|\Delta I|$ for each electrode. $|\Delta I|_{thresh}$ is shown as a dashed red line in Figure 3.4 (b). The green and the black dashed lines indicate 67% and 50% of $|\Delta I|_{thresh}$ respectively. In Figure 3.4 (a), red circles indicate the detection of switching events with

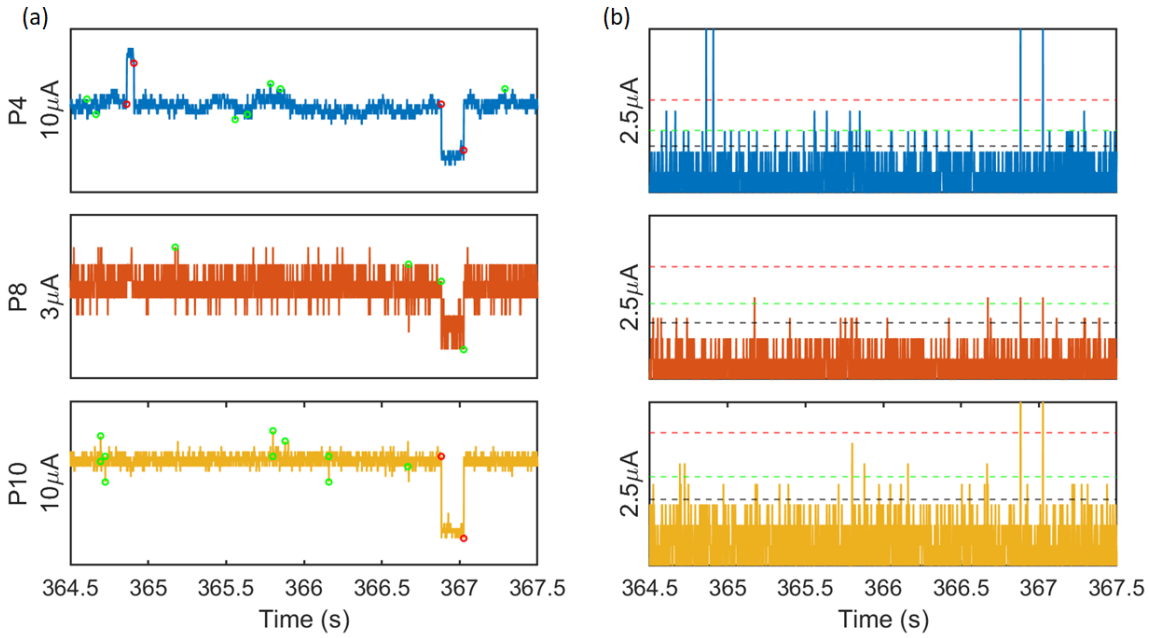

Figure 3.4: *(a) I and (b) $|\Delta I|$ at three electrodes of Device I in configuration A over 3s (see Section 3.2 for device and configuration details). The sampling rate was 1kHz, applied voltage was 10V. In (b), the red line indicates $|\Delta I|_{thresh}$, while the green and black lines indicate 67% and 50% of $|\Delta I|_{thresh}$ respectively. Note that $|\Delta I|_{thresh}$ is different for each of the electrodes. In (a), the red circles indicate events detected with a threshold of $|\Delta I|_{thresh}$, and the green circles indicate all $|\Delta I|$ between the green and red thresholds ($0.67 \times |\Delta I|_{thresh} < |\Delta I| < |\Delta I|_{thresh}$). Note that the scale for electrode P8 is different to the other vertical scales in (a).*

a threshold of $|\Delta I|_{thresh}$ ($|\Delta I| > |\Delta I|_{thresh}$). The green circles indicate events that would be identified with a threshold of 67% of $|\Delta I|_{thresh}$, but not identified with a threshold of $|\Delta I|_{thresh}$ ($0.67 \times |\Delta I|_{thresh} < |\Delta I| < |\Delta I|_{thresh}$).

All noise fluctuations in this segment are smaller than the red threshold. Moreover, events at electrode P4 and P10 are correctly identified with the red threshold near 366.9s and 367s. Two other events are observed with the red threshold at electrode P4 near 364.9s. Another two step-wise changes in I are observed at electrode P8 near 366.9s and 367s. However, these changes in I are below the red threshold and ignored. Therefore, while the red threshold is larger than all noise in this segment, it cannot identify events of a comparable size to large noise fluctuations.

The green threshold does identify the changes in I at electrode P8 near 366.9s and 367s. However, the largest noise fluctuations are incorrectly identified as events with the green threshold. For example, noise near 365.2s is incorrectly identified as an event at electrode P8 with the green threshold. Relatively little noise is larger than the green threshold, and so it is a reasonable threshold. In contrast, the black threshold is smaller than a significant amount of noise, which means it is a poor threshold for the data.

Overall, $|\Delta I|_{thresh}$ is the largest reasonable threshold for the data in Figure 3.4, and 67% of $|\Delta I|_{thresh}$ is the smallest reasonable threshold for the data. The main analysis in this thesis is completed with an event threshold of $|\Delta I|_{thresh}$ to minimise noise in the analysis. Later sections compare the analysis with $|\Delta I|_{thresh}$ to an analysis with an event threshold of

67% of $|\Delta I|_{thresh}$, to ensure the choice of threshold does not significantly change the results.

3.2 Measurement Details

All data in this thesis is characterised by the device measured, electrode configuration, DC bias applied to the input electrodes, and the sampling rate of the measurement. Hence, from this point onwards, the notation [a, b, c, d] is used to describe the measurement conditions for all presented data. Here, a represents the device, b represents the electrode configuration, c is the applied voltage, and d is the sampling rate in kHz. For example, [DI, A, 2V, 100] refers to a measurement at 100kHz of Device I in electrode configuration A with 2V DC bias applied to the input electrodes. The different devices and electrode configurations are described below. The effect of different input voltages and sampling rates are discussed separately in Section 3.3.2 and Section 4.1.1 respectively.

3.2.1 Devices Analysed

Many devices were fabricated and analysed. Results from two devices, referred to as Device I and Device II, are presented in this thesis. Note that all ten electrodes successfully connected to the PASN in Device I, whereas only nine electrodes were connected in Device II. Hence, most of the analysis focuses on Device I.

3.2.2 Electrode Configurations

Number of Input Electrodes

A key advantage of the MC devices is flexibility in the positions of the input and output electrodes, which are described by the electrode configuration. One of the important parameters of the electrode configuration is the number of input electrodes.

Figure 3.5 (a) shows data from Device II when one electrode is used as an input. Clearly, the observed switching activity is qualitatively identical at all electrodes. Hence, the multiple electrodes provide little extra information about the switching activity that cannot be obtained with a 2T device.

Figure 3.5 (b) shows data from Device II when four electrodes are used as inputs (identical to configuration D discussed below). The changes in I are similar between electrodes P4, P6, and P10. In contrast, the current at electrode P14 is different to all other electrodes, as is the current at electrode P16. Hence, the data is different and more interesting between electrodes when multiple input electrodes are used. Note that the data in Figure 3.5 (b) was obtained immediately after the data in Figure 3.5 (a), hence all differences between the figures can be attributed to the electrode configuration change.

The difference between measured data with one input electrode and multiple input electrodes can be explained as follows. When one input is used, most of the potential drops very close to the input electrode because it is surrounded by grounded electrodes. Hence, the voltage drop is very low at the opposite end of the device, and very few tunnel gaps will be activated. Therefore, most of the tunnel gaps are activated near the input electrode

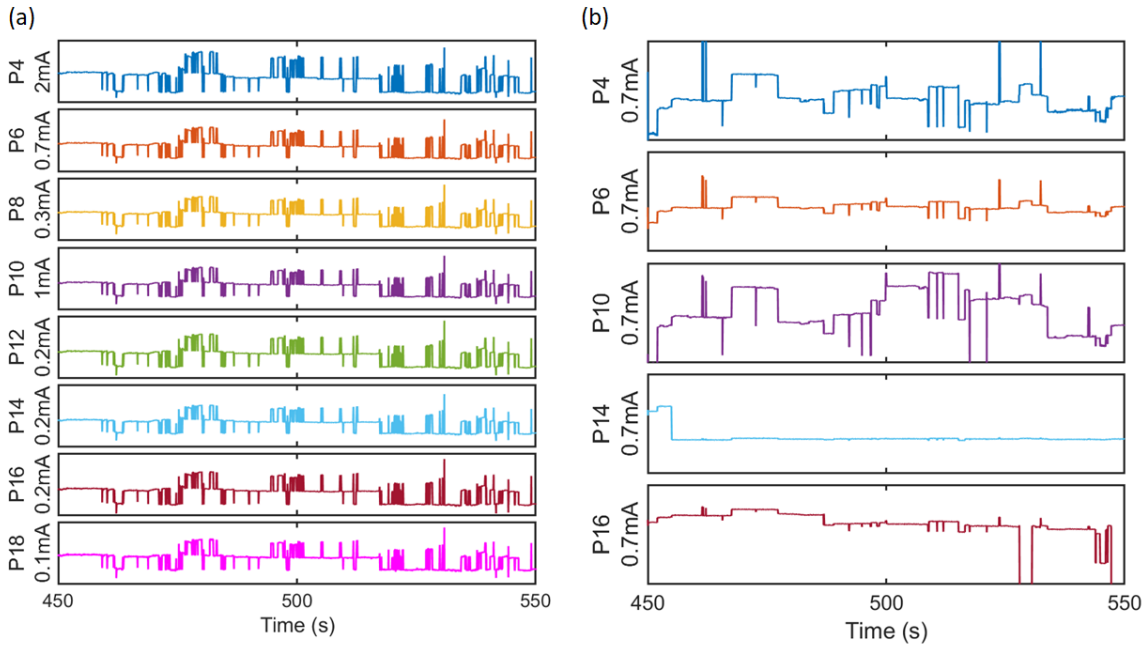

Figure 3.5: *Comparison of measured current with different numbers of input electrodes. All data is for Device II with 7V applied to each input electrode. (a) Current measured over 100s at eight connected output electrodes when electrode P2 is the only input. Qualitatively identical switching activity is observed at all electrodes. Note that the vertical scales are different for each electrode in (a). (b) Current measured over 100s at five connected output electrodes when electrodes P2, P8, P12, and P18 are input electrodes. This configuration is identical to electrode configuration D, as described below. All vertical scales are identical in (b). The switching activity is not identical at all output electrodes. Note that electrode P20 was disconnected from the network in Device II, hence it is not shown. The sampling rate is 1kHz.*

when one input is used. Hence, qualitatively similar switching activity is observed at all output electrodes because only a small group of tunnel gaps are active. In contrast, multiple input electrodes stimulate the tunnel gaps in multiple parts of the network. Hence, more complicated switching activity is observed with multiple input electrodes. All data analysed in this thesis was obtained with four input electrodes.

Configurations Analysed

Different electrode configurations were analysed to investigate whether the network activity changed with different input and output electrodes. Schematics of all configurations used in this thesis are shown in Figure 3.6. The electrode configurations are referred to by the letters shown in Figure 3.6. The analysis in Chapter 4 compares the analysis for different electrode configurations.

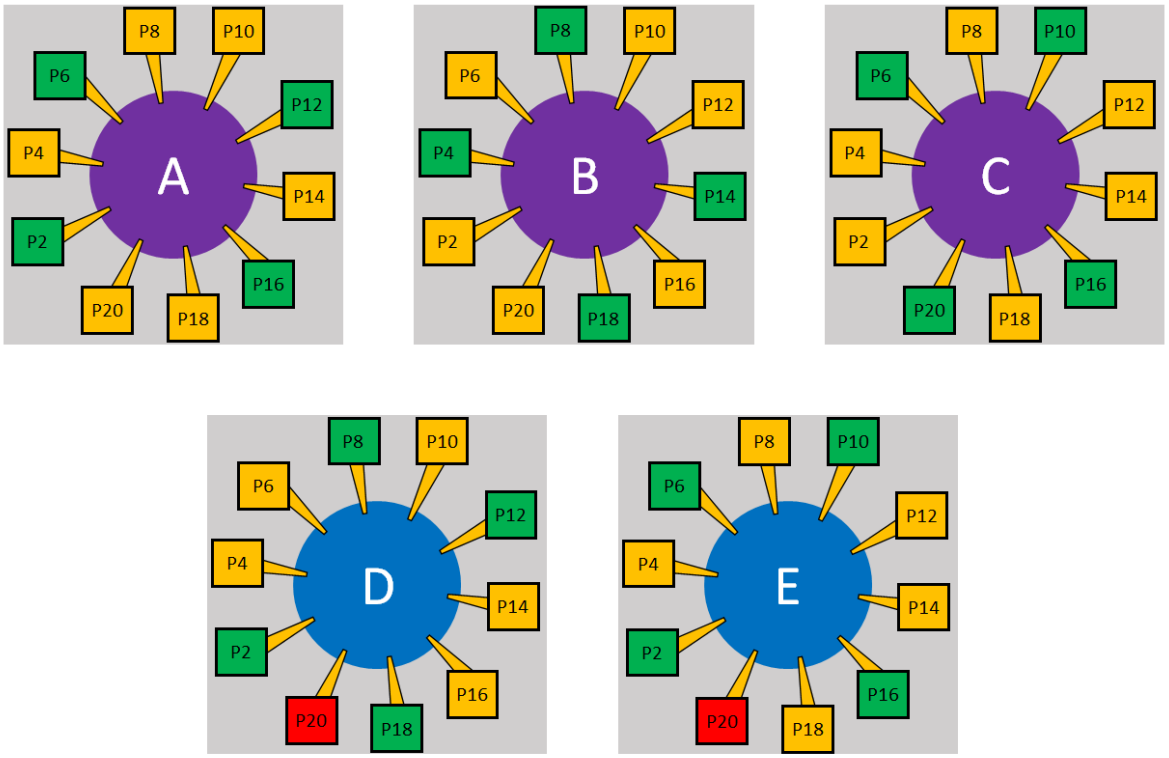

Figure 3.6: *Schematic of the five electrode configurations analysed throughout this thesis. The gold squares represent output electrodes that are grounded during measurement, and the green squares represent input electrodes. All measurements applied the same DC bias to the input electrodes. Configurations A, B, and C all correspond to configurations of Device I, whereas configurations D and E correspond to Device II. Note that the red squares represent electrodes that did not connect to the network.*

3.3 Comparison of MC and 2T Devices

Before focusing on a detailed analysis of the MC devices in Chapter 4 and Chapter 5, it is important to compare the switching dynamics of the MC and 2T devices. This section briefly explores some of the key differences and similarities between the switching behaviour of the two device geometries. A detailed comparison of the device morphology and switching activity is presented in [95]. Note that the analysis in this section was completed with data sampled at 100kHz unless otherwise noted.

3.3.1 Spiking Data

The MC devices show complex patterns of switching events, as shown in Figure 3.5, which are qualitatively similar to switching activity observed in 2T devices [13–15]. However, the measurement system of the MC devices allows for MHz sampling (Section 2.4) which has resolved new data features. Notably, it is possible to observe the same change in current for all switching events over a relatively long period in the MC devices. Such activity is referred to as 'spiking' behaviour. Previous research on 2T devices rarely showed spiking activity because a sampling rate of 5kHz or slower was typically used. It is high sampling rates (100kHz) that allow for frequent observation of spiking activity. A detailed description

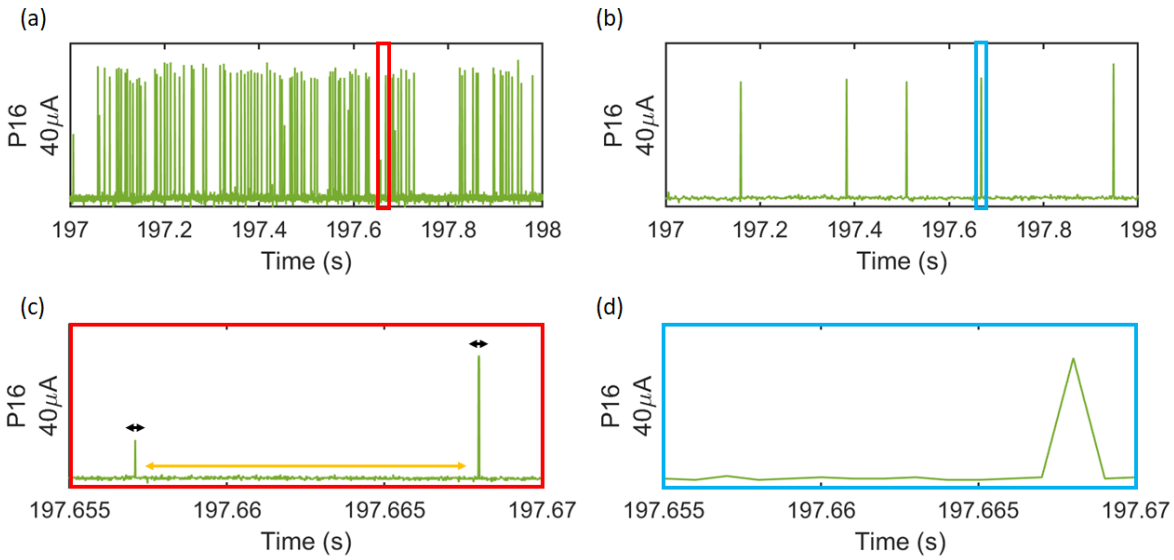

Figure 3.7: *Example of spiking data observed in MC devices. (a,b) Current measured at electrode P16 over the same 1s segment with a 100kHz (a) and 1kHz (b) sampling rate ([DI,B,10V]). Many more switching events are observed with the 100kHz sample rate. (c,d) Horizontal magnification of the 15ms segments in the red and blue rectangles respectively. The black arrows in (c) show the time between an increase in current and the subsequent decrease in current is ~20-50μs, while the gold arrows in (c) show the time between the decrease in current and subsequent increase in current can be ~10ms.*

of spiking can be found in [95].

Figure 3.7 (a) and (b) show the same example of spiking activity measured with a sample rate of 100kHz and 1kHz respectively. The 1kHz data was obtained by subsampling the 100kHz data, such that the 1kHz data is identical to every 100^{th} data-point of the 100kHz data (see Section 4.1.1). The spiking activity is very dense with the 100kHz sampling rate and ~800 events are detected in this segment. In contrast, the spiking is very sparse with the 1kHz sampling rate and only ~10 events are detected. Therefore, 100kHz sampling rates have many more events than 1kHz spiking rates.

Figure 3.7 (c) and (d) show magnified sections from the red and blue squares in Figure 3.7 (a) and (b) respectively. Each 'spike' is formed from an event that causes an increase in current, and an event that causes a decrease in current. The black arrows in Figure 3.7 (c) show the time between the increase and decrease in current is ~30μs, which clearly cannot be resolved with a sampling rate of 1kHz in Figure 3.7 (d). Additionally, the gold arrow indicates the time between the decrease and subsequent increase in current is relatively long at ~10ms. Note that the effect of spiking and subsampling on the analysis is discussed further in Section 4.1.1.

3.3.2 Voltage Dependence

Figure 3.8 (a) shows the total observed switching events when different voltages were applied to Device I in electrode configuration A for 10-minutes each. The number of events roughly increases with the voltage applied, similarly to previous voltage dependence results for 2T

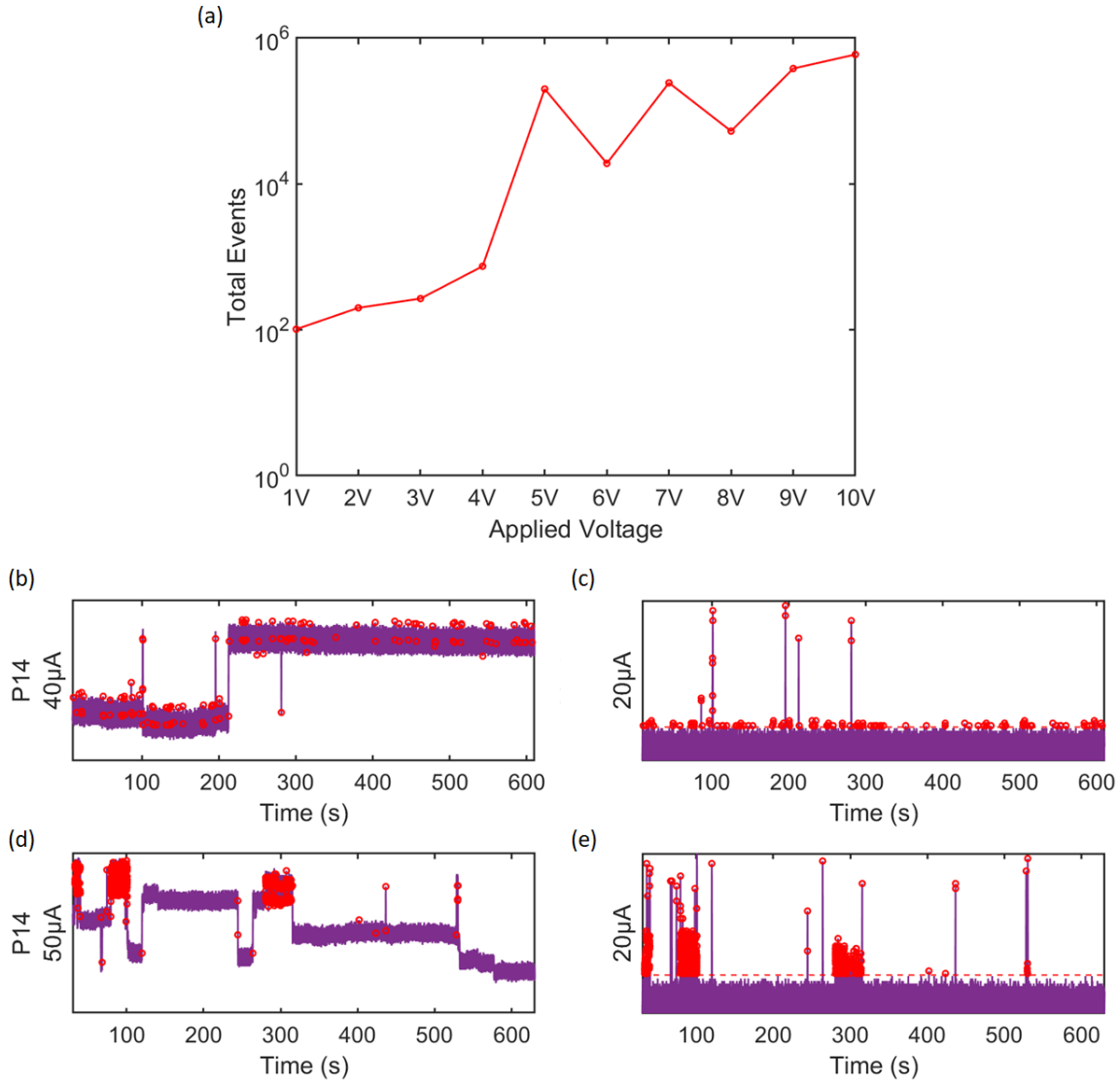

Figure 3.8: *(a) Voltage dependence of the switching rate of MC devices. Each data-point shows the total number of events across all output electrodes that were observed in 10-minutes with the given input voltage ([DI, A, 1V-10V, 100]). Total events roughly increases with voltage. Note that large noise fluctuations account for ~100-500 events at each voltage. (b) I and (c) $|\Delta I|$ over 10-minutes for electrode P14 with 4V input voltage. Switching events are shown as red circles. Most switching events are due to large noise fluctuations. (d) I and (e) $|\Delta I|$ over 10-minutes for electrode P14 with 5V input voltage. Many true switching events are observed. $|\Delta I|_{thresh}$ is shown as a red dashed-line in (c) and (e).*

devices [15].

Events were observed at all applied voltages in Figure 3.8 (a), whereas previous research shows a critical voltage is required for consistent switching activity in 2T devices [15]. To further investigate the critical voltage, Figure 3.8 (b) and (c) show I and $|\Delta I|$ respectively over 10-minutes for electrode P14 when 4V DC bias is applied. Approximately 140 events (red circles) are observed in Figure 3.8 (b). Only ~20 of these are due to switching events, while the other ~120 events are large noise fluctuations that are slightly above the threshold. Hence, consistent switching activity is not observed at 4V. Moreover, all data in Figure 3.8 (a) that is below ~500 counts (total events) should be considered non-significant due to noise

that is incorrectly identified as events.

Figure 3.8 (d) and (e) show I and $|\Delta I|$ respectively over 10-minutes for electrode P14 when 5V DC bias is applied. Many true switching events are identified, and relatively little noise is incorrectly identified as an event. A comparison of the 4V and 5V data shows that large switching events are consistently observed at ~4-5V, which acts as the critical voltage for this type of switching activity.

Note that it is expected for some noise to be above the threshold ($|\Delta I|_{thresh}$), because the threshold is determined from a relatively small segment of data compared to the 10-minutes of data analysed. Therefore, it is likely the threshold slightly underestimates the noise, and that the largest noise fluctuations in the measurement are incorrectly observed as events. Very little noise is larger than $|\Delta I|_{thresh}$ ($< 0.001\%$ of all data-points).

3.3.3 IEI Distribution

PASNs exhibit bursts of switching activity, which can be characterised by the time between consecutive events [16]. The times between events, or inter-event intervals (IEI), take on a wide range of values for bursty dynamics. Previous research of PASNs [71] established that the IEIs are distributed as a power law of the form

$$P(t_{IEI}) \sim {t_{IEI}}^{-\gamma} \tag{3.3}$$

where $P(t_{IEI})$ is the probability to observe an IEI of duration t_{IEI}. A power law distribution of IEIs indicates that most events occur very quickly after other events, however there is a distinct probability for very long times between events. To calculate the IEIs, we first convert the data at each electrode to a binary array that is referred to as the *event train*, and is defined by

$$E_i(t) = \begin{cases} 1 & \text{if an event is detected at electrode i at time } t \\ 0 & \text{otherwise} \end{cases} \tag{3.4}$$

where t is a time-step in the measurement. $E_i(t)$ represents the event train for the i^{th} output electrode. The IEIs for a given electrode are calculated as the time between consecutive events ($E_i(t) = 1$) in the event train.

Figure 3.9 shows the distribution of IEIs for electrode P2 of Device I ($E_{P2}(t)$). The IEIs approximately follow a straight line on the logarithmic axes, which indicates the IEIs are distributed as a power law. Moreover, the slope of the power law (γ in Equation 3.3) is ~1.7, which is similar to the power law slope for previous 2T devices [16].

3.3.4 Avalanche Statistics

Critical systems have many computational advantages and there is significant evidence the brain operates at a critical point [1]. Previous research into 2T devices found PASNs are critical systems that exhibit avalanches of activity. [16]. This section presents the avalanche analysis for electrode P2 over a 10-minute measurement of Device I. All methods are identical to those described in [16]. A brief background to the analysis is provided below.

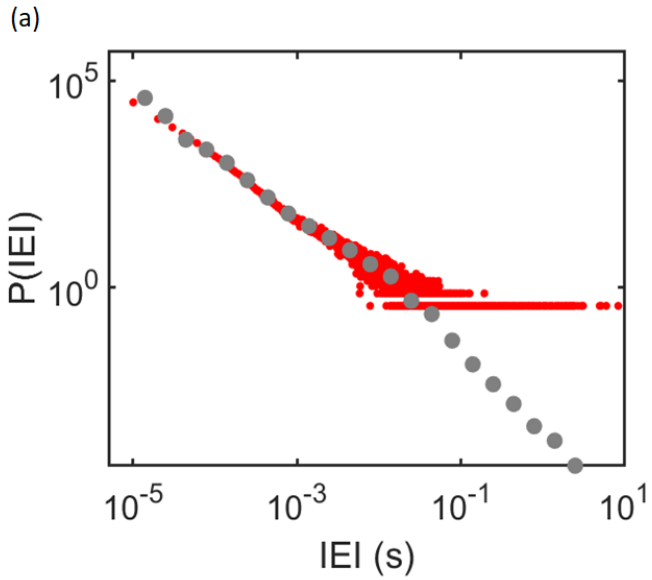

Figure 3.9: *Probability density function (PDF) of the IEIs recorded in 10-minutes for electrode P2 of Device I ([DI, B, 10V, 100]). Note that the IEIs are only for events detected at electrode P2 ($E_{P2}(t)$). The red dots correspond to the PDF with linear bin sizes, whereas the grey dots correspond to logarithmic bin sizes. The IEIs are roughly power law distributed with a slope of ~1.7. A small peak near 10ms is attributed to spiking data.*

Avalanches are defined by considering the event rate at the i^{th} electrode, $s_i(t)$, i.e. by counting the number of events per time bin [71]. The size of each bin is equal to the average IEI $\langle IEI \rangle$ for the i^{th} electrode [71]. Figure 3.10 (a) shows an example of the binning process when $\langle IEI \rangle = 3 time - steps$. Each time-bin holds the value of the total number of events in that bin. For example, time-bin 3 in Figure 3.10 (a) has a value of 2, because 2 events occurred within that time-bin in the event train before binning.

An avalanche is defined as a sequence of consecutive time-bins with at least one event detected [1]. The size, S, of an avalanche is the total number of events that occur in the avalanche, while the duration, T, is the number of time-bins between the start and end of the avalanche. The avalanche profile, or shape, is the size of the avalanche at each time-bin. Figure 3.10 (b) shows the avalanche profile for the avalanche of size 13 and duration 7 in Figure 3.10 (a).

Critical systems have avalanche sizes and durations which are distributed as power laws [16]

$$P(S) \sim S^{-\tau} \tag{3.5}$$

$$P(T) \sim T^{-\alpha} \tag{3.6}$$

$$\tag{3.7}$$

additionally, the average avalanche sizes are related to the avalanche duration according to

$$\langle S \rangle (T) \sim T^{1/\sigma\nu z} \tag{3.8}$$

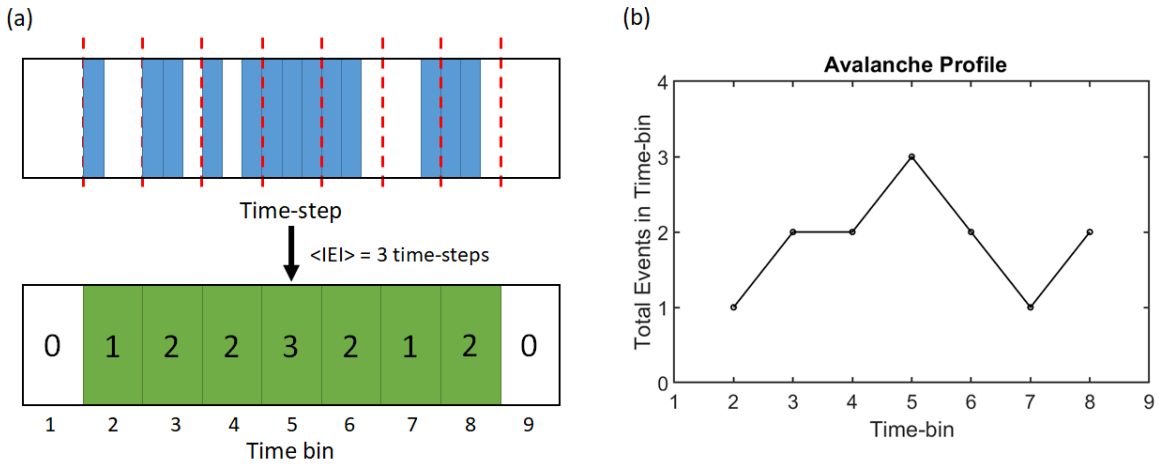

Figure 3.10: *(a) The event train is shown at the top with blue rectangles representing the detection of an event in a time step ($E_i(t) = 1$), and white rectangles representing no event detection in a time-step ($E_i(t) = 0$). The red dashed lines indicate bins of 3 time-steps. The event rate, $s_i(t)$, is shown at the bottom with green rectangles representing $s_i(t) > 0$. The value of $s_i(t)$ is labelled at each time-bin. $s_i(t)$ forms an avalanche of size 13 as 13 events were detected, and duration 7, as 7 consecutive time-bins include at least one event. (b) The avalanche profile for the avalanche shown in (a).*

where $1/\sigma\nu z$ is a characteristic exponent of the critical system [16]. The exponents of the size and duration distributions relate to $1/\sigma\nu z$ by the crackling relationship

$$\frac{1}{\sigma\nu z} = \frac{\alpha - 1}{\tau - 1} \tag{3.9}$$

A third measure of $1/\sigma\nu z$ is given by the characteristic 'collapse' of the avalanche profiles onto a universal scaling function [16]. Agreement between each measure of $1/\sigma\nu z$ is a strong indicator of criticality.

Figure 3.11 (a) shows the distribution of the avalanche sizes, and Figure 3.11 (b) shows the distribution of the avalanche durations for a electrode P2 in a 10-minute measurement of Device I. Both the avalanche sizes and durations are distributed as power laws with exponents $\tau = 1.93 \pm 0.03$ and $\alpha = 2.72 \pm 0.06$ respectively. Equation 3.9 then yields $1/\sigma\nu z = 1.8 \pm 0.1$. Figure 3.11 (c) shows the average avalanche size depends on the avalanche duration, and Equation 3.8 yields $1/\sigma\nu z = 1.69 \pm 0.03$. Finally, Figure 3.11 (d) shows the avalanche shapes (red lines) collapse onto a single curve (black line), which yields $1/\sigma\nu z = 1.79 \pm 0.07$ (see [16] for details of the shape collapse).

All three measures of $1/\sigma\nu z$ agree within the uncertainties, which strongly suggests the MC devices are critical. Note that all power laws were fitted with the methods described in [16], and the uncertainties are equal to one standard deviation.

3.3.5 Device Comparison Summary

Qualitatively similar switching activity is observed in both the 2T and MC devices. Furthermore, both device geometries show similar voltage dependence on the switching rate, the

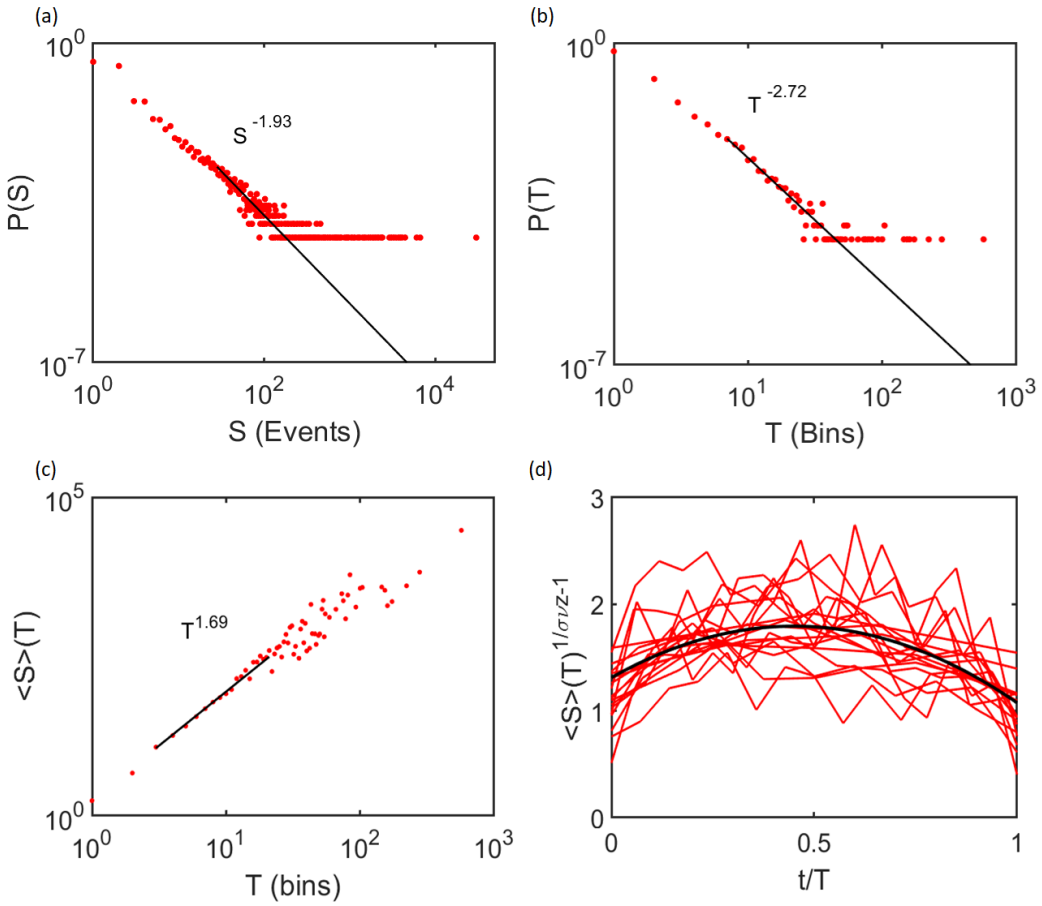

Figure 3.11: *Avalanche analysis for 10-minutes of data from electrode P2 of Device I ([DI, B, 10V, 100]). See [16] for details of the analysis. (a) PDF of the avalanche sizes, S. (b) PDF of the avalanche durations, T. Both (a) and (b) are distributed as power laws, and the exponents yield* $1/\sigma\nu z \sim 1.8 \pm 0.1$ *with Equation 3.9. (c) Average avalanche size,* $\langle S \rangle$*, depends on avalanche duration T with a slope of* $1/\sigma\nu z \sim 1.69 \pm 0.03$*. (d) The avalanche shapes (red lines) collapse onto a single curve (black line), and yield* $1/\sigma\nu z \sim 1.79 \pm 0.07$*.*

existence of a critical voltage, power law IEI distributions, and critical avalanches of activity. These results provide strong evidence that the same critical switching behaviour is observed independently of device geometry.

3.4 Summary of Basic Results

This chapter has introduced the threshold procedure for event identification (Section 3.1), and described the different measurement conditions (Section 3.2). Additionally, Section 3.3 showed that the device geometry does not significantly affect the switching activity of PASNs. Finally, subsampling was shown to reduce the amount of spiking data and to maintain the non-spiking events. The next chapters present a detailed analysis of the complexity of PASNs.

Chapter 4

Qualitative Complexity

The neurons in the brain form an incredibly complex network which generates equally complex dynamics. It is widely accepted that this underlying complexity supports the emergence of coherent physiological activity in the brain [35]. Among these emergent phenomena are the classification, pattern recognition, and learning tasks that neuromorphic computing aims to achieve [71]. Therefore, it is natural to attempt to emulate the intrinsic complexity of the brain in neuromorphic architectures as a route to achieve brain-like computational efficiency.

Complexity is a notoriously opaque concept, and no rigorous definition is accepted throughout the literature [103, 104]. However, several qualities of dynamical complexity are generally agreed upon. For example, entirely random or periodic dynamics are classed as simple, while complex dynamics exist in-between these cases [103]. Therefore, a first check for complexity is to identify whether the network dynamics are random, periodic, or somewhere in-between.

This chapter describes the qualitative analysis of switching event dynamics in multi-electrode (MC) PASNs. Each electrode is assumed to be most sensitive to different regions of the network. Therefore, the relationship between signals on different electrodes provides information on how switching events are correlated throughout the network. Data that is qualitatively complex should have patterns of correlations which change over time and cannot arise from random processes.

The remainder of this chapter is organised as follows: Section 4.1 shows the results and analysis from experiments on physical PASNs. Section 4.2 compares the analysis from experiments to an analysis of simulated PASNs. Finally, Section 4.3 summarises the presented results and highlights the next steps to identify complexity in PASNs, which are then discussed in Chapter 5.

4.1 Experimental Data

This section first discusses the effect of spiking data on the complexity and how it is reduced with subsampling throughout the remainder of the thesis (Section 4.1.1). Next, segments of typical switching activity for Device I and Device II are shown to demonstrate qualitative complexity (Section 4.1.2), and the results are briefly summarised (Section 4.1.3). The remainder of this section analyses key qualitative features of complexity in the MC data (Sec-

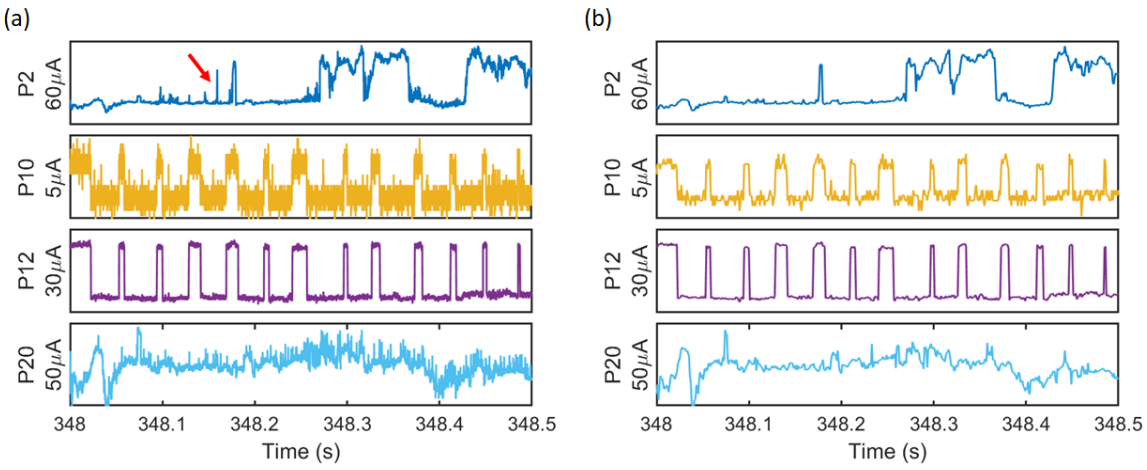

Figure 4.1: *(a) Current measured at four electrodes over 5s with a sampling rate of 100kHz ([DI, B, 10V, 100]). (b) The same segment of data as (a) but subsampled to 1kHz. (a) The red arrow indicates a pair of events with a sub-millisecond IEI which is not identified in (b). All switching events with IEIs longer than ~1ms are identified regardless of the sampling rate.*

tion 4.1.4), investigates how different parameters affect the qualitative complexity (Section 4.1.5, Section 4.1.6), and discusses the experimental analysis (Section 4.1.7).

4.1.1 Subsampling

Complexity depends on the combinations of electrodes that events are detected at simultaneously [1]. Typically, spiking data is observed at one or two electrodes, while other switching events are observed at many different combinations of electrodes (see below) [95]. Hence, non-spiking activity is more complex than spiking activity.

All data in the thesis was originally measured with a sampling rate of 100kHz for 10-minute measurements, or 1kHz for longer measurements. As discussed in Section 3.3.1, a sample rate of 100kHz allows for resolution of spiking data that can contain tens of thousands of switching events in relatively short periods. This is a significantly higher event rate than what is observed for non-spiking events. Therefore, the spiking activity can overwhelm the other switching events in a measurement.

As shown in Figure 3.7, the amount of spiking can be significantly reduced by subsampling the data. Hence, to reduce the impact of the spiking data on the complexity analysis, all 100kHz data used for future analysis is subsampled to 1kHz. The subsampling takes every 100^{th} data-point of the 100kHz data and ignores all other data-points. This process produces similar results to data that was originally sampled at 1kHz.

Figure 4.1 (a) shows the current measured at four electrodes for 5s with a 100kHz sampling rate, and Figure 4.1 (b) shows the same data after subsampling to 1kHz. Clearly, the switching activity is nearly identical regardless of the sampling rate. However, some events with IEIs less than ~1ms (red arrow in Figure 4.1 (a)) are typically not resolved in the 1kHz data. Therefore, subsampling the data reduces the amount of fast spiking activity, and does not significantly change the non-spiking activity.

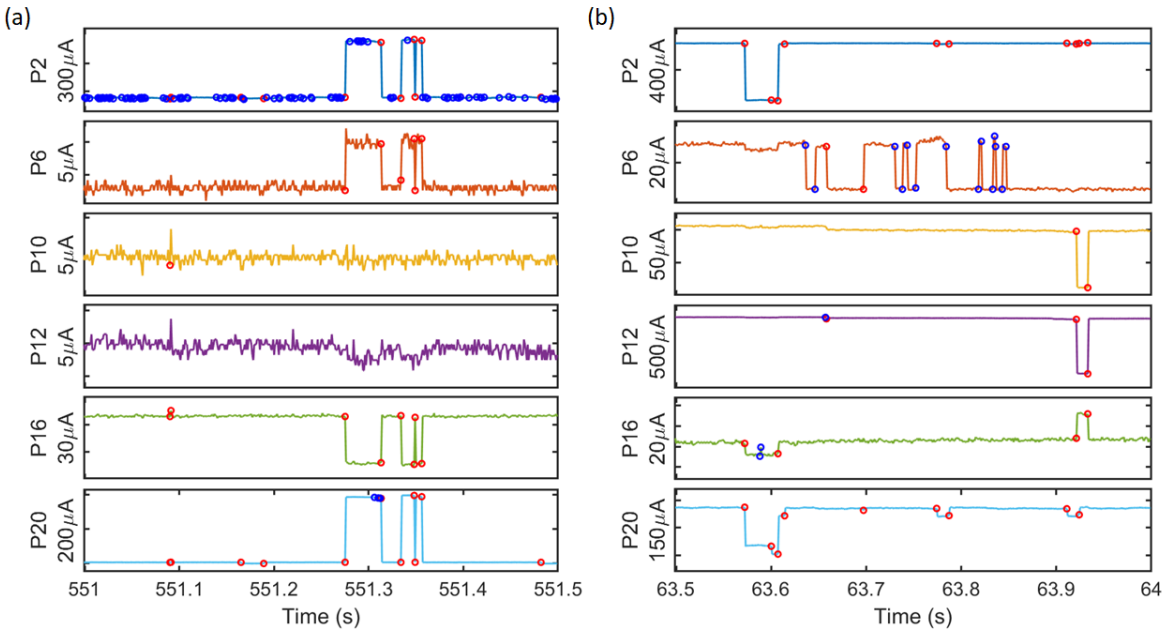

Figure 4.2: *(a,b) 0.5s of current data taken from different parts of the same 10-minute measurement ([DI, B, 10V, 1]). Each panel shows data measured at a different electrode. The electrode identifier and the vertical scale are shown next to each panel. Note that the scale varies by up to a factor of 100 between panels. The red circles indicate a switching event was detected at multiple electrodes simultaneously (correlated events). The blue circles indicate a switching event was detected at only one electrode (isolated events).*

We emphasise that the threshold procedure is applied after subsampling, so that the 1kHz data has a different threshold to 100kHz data. Note that, d in the notation [a, b, c, d] (Section 3.2) refers to the the sampling rate after subsampling.

4.1.2 Results

Device I

Figure 4.2 (a) and (b) show the current, I, for different 0.5s segments of typical data for a 10-minute measurement of Device I in electrode configuration B. Each panel shows the current measured at a different electrode. Additionally, the electrode label and the vertical scale are shown next to each panel. Below is a summary of the data features for each figure and the correlations between switching events. The segments are each 0.5s for simplicity.

Figure 4.2 (a) shows events were detected simultaneously at electrodes P2, P6, P16, and P20 from 551.27 to 551.36s. These events, and others that were detected at multiple electrodes simultaneously (red circles), are referred to as *correlated* events. Other correlated events were observed at electrodes P2, P10, P16, and P20 near 551.09s, and electrodes P2 and P20 from 551.16 to 551.19s, and near 551.48s. Many events were observed at electrode P2 in the 0.5s of data, that were not detected at other electrodes. The events that were detected at only one electrode (blue circles) are referred to as *isolated* events. Further isolated events were detected at electrode P20 near 551.31s.

Figure 4.2 (b) shows an example of typical device behaviour for which correlated events

were detected at different combinations of electrodes to the data shown in Figure 4.2 (a). Correlated events were observed at electrodes P2, P16, and P20 from 63.57 to 63.61s, and at electrodes P2, P10, P12, and P16 from 63.91 to 63.92s. Additional correlated events were detected at electrodes P6 and P12 near 63.66s, electrodes P6 and P20 near 63.7s, and at electrodes P2 and P20 near 63.6s, 63.68s, and 63.91s. Isolated events were also observed at electrodes P6, P12, and P16.

Figure 4.2 (a) and (b) show distinctly different patterns of isolated and correlated events. For example, correlated events were observed at electrode P12 with electrodes P2, P10, and P16 in Figure 4.2 (b), whereas no events were observed at electrode P12 in Figure 4.2 (a). Table 4.1 summarises the event patterns observed in Figure 4.2 (a) and (b).

	Figure 4.2 (a)	Figure 4.2 (b)
Combinations of electrodes that correlated events were detected at	(P2,P6,P16,P20), (P2,P10,P16,P20), (P2,P20)	(P2,P10,P12,P16), (P2,P16,P20), (P6,P12), (P6,P20), (P2,P20)
Electrodes that isolated events were detected at	(P2), (P20)	(P2), (P12), (P16)

Table 4.1: *Comparison of the patterns of correlated and isolated events observed in two 0.5s segments of data for Device I ([DI, B, 10V, 1]). The notation (a,b,c,...) corresponds to a combination of electrodes a, b, and c. For example, (P2,P20) corresponds to the combination of electrodes P2 and P20*

Device II

Figure 4.3 (a) and (b) show different segments of typical current data for a 10-minute measurement of Device II. Similarly to Figure 4.2 (a) and (b), each panel shows the current measured at a different electrode, with the electrode labels next to each panel. Note that the electrodes for Device II are different to the electrodes of Device II, hence P20 of Device I is unrelated to P20 of Device II. The same symbols from Figure 4.2 (a) and (b) are used to identify the correlated and isolated events detected on each electrode. Only five panels are shown in Figure 4.3 (a) and (b) because only five output electrodes were connected to the PASN for electrode configuration E (Figure 3.6).

Figure 4.3 (a) shows similar large changes in current were observed at all electrodes. Hence, correlated events were observed at all electrodes throughout the data segment. The only other correlated events were observed at electrodes P4 and P8 from 478.7s to 479.45s, and at electrodes P4 and P14 near 479.4s. Additionally, isolated events were observed at electrode P4, P8, and P14.

Figure 4.3 (b) shows another example of Device II data with different correlated events. Correlated events were detected at electrodes P4, P8, P12, and P14 near 24.6s, 24.72s, and 24.98s. Furthermore, a single correlated event was observed at electrodes P4, P12, and P14 near 24.72s. Isolated events were detected at electrode P4 near 24.54s, and at electrode P8 near 24.72s. Note that no events were detected at electrode P18.

Table 4.2 shows a summary of the combinations of electrodes that events were detected at in Figure 4.3 (a) and (b).

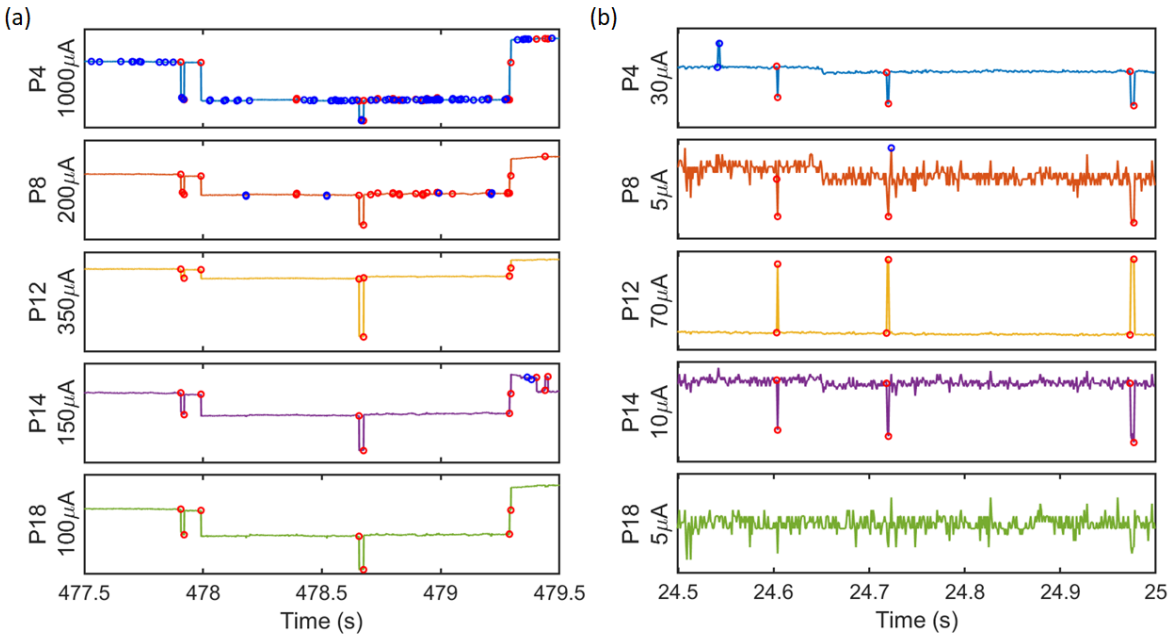

Figure 4.3: *(a,b) Current at each electrode for two different segments of the same 10-minute measurement ([DII, E, 8V, 1]). (a) Shows a 3s segment, and (b) shows a 0.5s data segment. The red and blue circles denote correlated and isolated events. Note the current scale has significant variation, especially between (a) and (b).*

	Figure 4.3 (a)	Figure 4.3 (b)
Combinations of electrodes that correlated events were detected at	(P4,P8,P12,P14,P18), (P4,P8), (P4,P14)	(P4,P8,P12,P14), (P4,P12,P14)
Electrodes that isolated events were detected at	(P4), (P8), (P14)	(P4), (P8)

Table 4.2: *Comparison of the patterns of correlated and isolated events observed in two different segments of data for Device II ([DII, E, 8V, 1]).*

4.1.3 Results Summary

As shown in Figure 4.3 and Figure 4.2, the switching activity changes significantly over time in Device I, and changes slightly over time in Device II. Moreover, the qualitative features of the data for Device II is similar at most electrodes. Hence, the current measured on Device I appears qualitatively complex, whereas the current measured on Device II appears less qualitatively complex.

The summarised data for Device I (Table 4.1) is roughly similar to the summarised data for Device II (Table 4.2). Hence, the basic summaries of the data in Table 4.1 and Table 4.2 do not adequately capture whether the qualitatively complexity of PASN switching dynamics. New analysis methods are therefore required to establish whether the correlations between switching events in each device are qualitatively complex. The next section describes such analysis methods which can accurately analyse the level of complexity in large amounts of measured data.

4.1.4 Detailed Qualitative Analysis

We begin by defining κ_n, which is the number of time-steps in a measurement for which an event is detected simultaneously at n electrodes. In Figure 4.4 (a), κ_1 ~28,000 means that an event was detected at only one electrode at ~28,000 different time-steps. Similarly, $\kappa_6 = 7$ means that an event was detected at all six electrodes at seven different time-steps of the measurement. A detailed description of Figure 4.4 (a) is presented in the next section.

Second, we define f_D as the number of time-steps for which events were detected simultaneously at a combination, D, of electrodes. Every possible combination of electrodes is assigned a decimal value, D, by converting the binary readout from the event train at each electrode (E_i, Equation 3.4). Note that the numerical order of the electrode labels corresponds to the order of the binary combination. Hence, the binary readout of 100111 $\equiv$ 39 corresponds to a correlated event observed at the first, fourth, fifth, and sixth electrodes of a given configuration. In Figure 4.4 (b), f_{39} (shown by the blue arrow) is the number of time-steps that an event was simultaneously detected at electrodes P2, P12, P16, and P20 in the measurement of interest (electrode configuration B). Note that time-steps with no event detections do not count as a combination and do not correspond to a value of D. Hence, D ranges from 1 to $2^N - 1$, where N is the total number of output electrodes.

Device I

Figure 4.4 (a) shows κ_n for a 10-minute measurement of Device I (blue curve). κ_n declines approximately exponentially as n increases, and is non-zero at all values of n. Hence, most observed events are isolated events, but a significant number of events are observed simultaneously at all six electrodes. To establish qualitative complexity, it is important to understand whether the observed κ_n is a signature of correlated events, or if the data can be obtained from random processes.

The red line in Figure 4.4 (a) corresponds to κ_n when the data is randomised. The randomisation process shuffles the event train at each electrode so that events occur at each time-step with equal probability. This process is completed independently for each electrode, and the total number of events detected at each electrode is conserved. The randomisation process was implemented by the MATLAB Neural Complexity and Criticality (NCC) toolbox developed in [105], and is discussed further in Section 5.2.2.

Clearly, κ_n decreases much faster for the randomised data than for the real data. Furthermore, $\kappa_n = 0$ for all $n > 3$ for the randomised data, which is significantly different to the real data. The randomisation process destroys any correlations between events. Since the real data is significantly different to the randomised data, it is clear that the observed events are correlated.

Figure 4.4 (b) shows f_D for the same 10-minutes of data as Figure 4.4 (a). The largest value of f_D is observed at $D = 33$, which corresponds to binary 100001. Therefore, events were simultaneously detected at electrodes P2 and P20 more often than any other combination of electrodes. Additionally, there were 47 unique values of D for which $f_D \neq 0$, which suggests complex switching activity as events were detected at many different combinations of electrodes throughout the measurement.

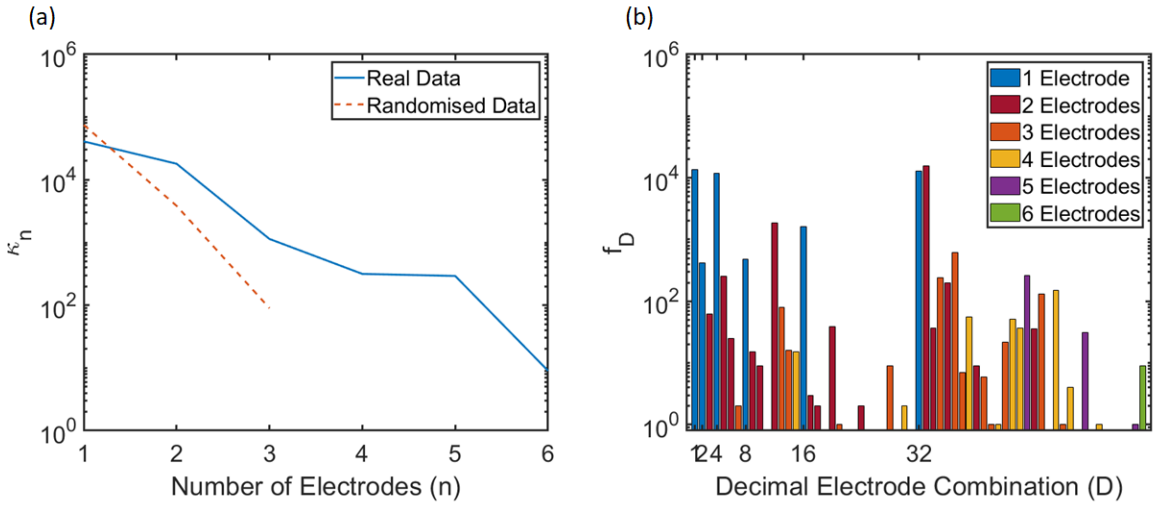

Figure 4.4: *(a) κ_n and (b) f_D for a 10-minute measurement of Device I ([DI, B, 10V, 1]). The measured configuration had six output electrodes, hence, n ranges from 1-6 and D ranges from 1-63. (a) The blue curve shows κ_n for the real data while the red line shows κ_n for a Poisson randomisation of the measured data. (b) Each value of D is colour-coded for the number of electrodes that an event was simultaneously detected at. The blue arrow indicates f_D at $D = 39$, which is the number of times a correlated event was detected at electrodes P2, P12, P16, and P20 for electrode configuration B.*

Device II

Figure 4.5 (a) shows κ_n for 10-minutes of data from Device II. Again, κ_n weakly decreases as n increases. Clearly, κ_n for the randomised data (red line) decreases much faster than κ_n for the real data. Note that the decrease in κ_n for the real data is not exponential like Figure 4.4 (a), because $\kappa_1 \sim \kappa_2$ (within one order of magnitude), and $\kappa_3 \sim \kappa_4 \sim \kappa_5$ (all within one order of magnitude of each other). Again, κ_n had a maximum at $n = 1$, which indicates many events in Device II were isolated events. These results are consistent with the data observed in Figure 4.3 (a) and (b), as many isolated events are observed and a relatively large number of events are observed at all electrodes.

Figure 4.5 (b) shows f_D for the 10-minute measurement of Device II in Figure 4.5 (a). A total of 27 values of D correspond to $f_D \neq 0$, and most of these are at $D \geq 16$. All values of $D \geq 16$ include electrode P4, hence events observed at electrode P4 can be simultaneously observed at many different electrodes.

4.1.5 Analysis Reproducibility

This section demonstrates the reproducibility of the analysis in Section 4.1.4 for different input voltages and electrode configurations. Furthermore, the variability over time is investigated. Note that all data in this section is from Device I as it had all electrodes connect to the network (Section 3.2.1).

Figure 4.6 (a) shows κ_n for 15 consecutive 10-minute segments from one measurement of Device I (grey curves). The total number of detected events varies by over half an order of magnitude, with the lowest event total in a segment at 12,200, and the largest

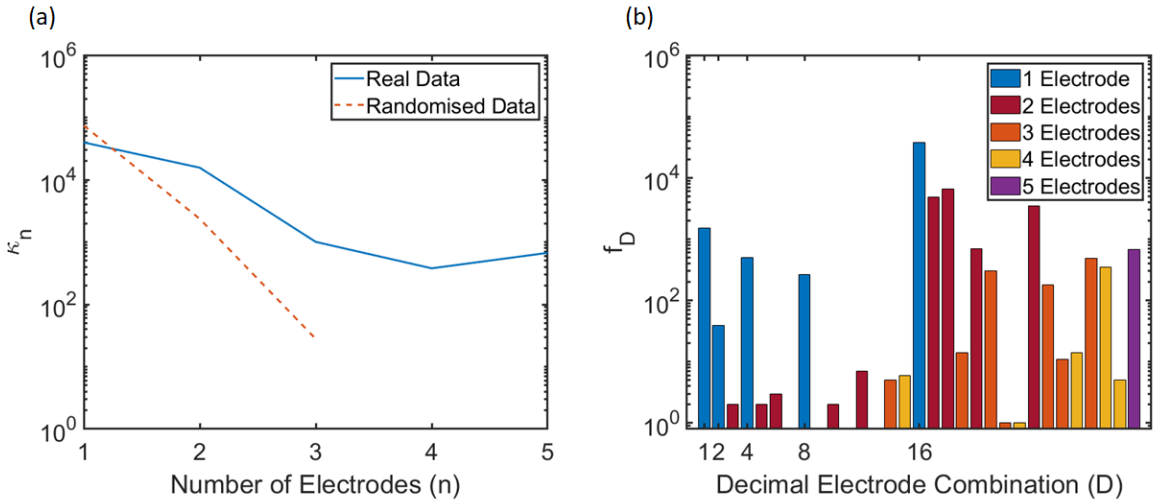

Figure 4.5: *(a) κ_n and (b) f_D for a 10-minute measurement of Device II ([DII, E, 8V, 1]). (a) κ_n for Poisson randomised data is shown in red.*

event total at 81,323. The minimum and maximum κ_n values (dashed red curves) have a qualitatively similar trend to the average κ_n (solid red curve). The scatter between 10-minute measurements is symmetrical on a log scale and covers a range of slightly less than one order of magnitude. Therefore, differences of one order of magnitude are treated as statistically significant for 10-minute measurements.

Figure 4.6 (b) shows κ_n for the same data as Figure 4.6 (a), except with the average of every 3 consecutive 10-minute measurements. The variation in κ_n for the average of 3 10-minute measurements is approximately half of an order of magnitude.

The distributions of f_D (not shown) for the same 10-minute and 30-minute data segments in Figure 4.6 (a) and (b) were analysed. For the 10-minute data segments, 40 ± 7 unique values of f_D were non-zero.

Figure 4.6 (c) shows the average κ_n of three 10-minute measurements at each of 8V, 9V, and 10V. The average κ_n at each voltage decreases approximately exponentially as n increases. Moreover, the average κ_n at each voltage is within the expected scatter for three 10-minute data segments (Figure 4.6 (b)). This result indicates the dynamics of the PASN are not significantly changed by the applied voltage.

Figure 4.6 (d) shows the average κ_n for three 10-minute measurements in each of electrode configuration A, B, and C. The value of κ_n is similar for all configurations at all values of n. Therefore, the configuration does not change the overall qualitative features of the analysis.

4.1.6 Threshold Dependence

As discussed in Section 3.1, the purpose of the event threshold is to maximise the number of events detected, while minimising the amount of noise that is incorrectly identified as events. The choice of threshold is a free parameter, and hence the effect of different thresholds on the analysis must be explored. This section presents a comparison of the qualitative analysis with an event threshold of $|\Delta I|_{thresh}$, to an event threshold of $0.67 \times |\Delta I|_{thresh}$.

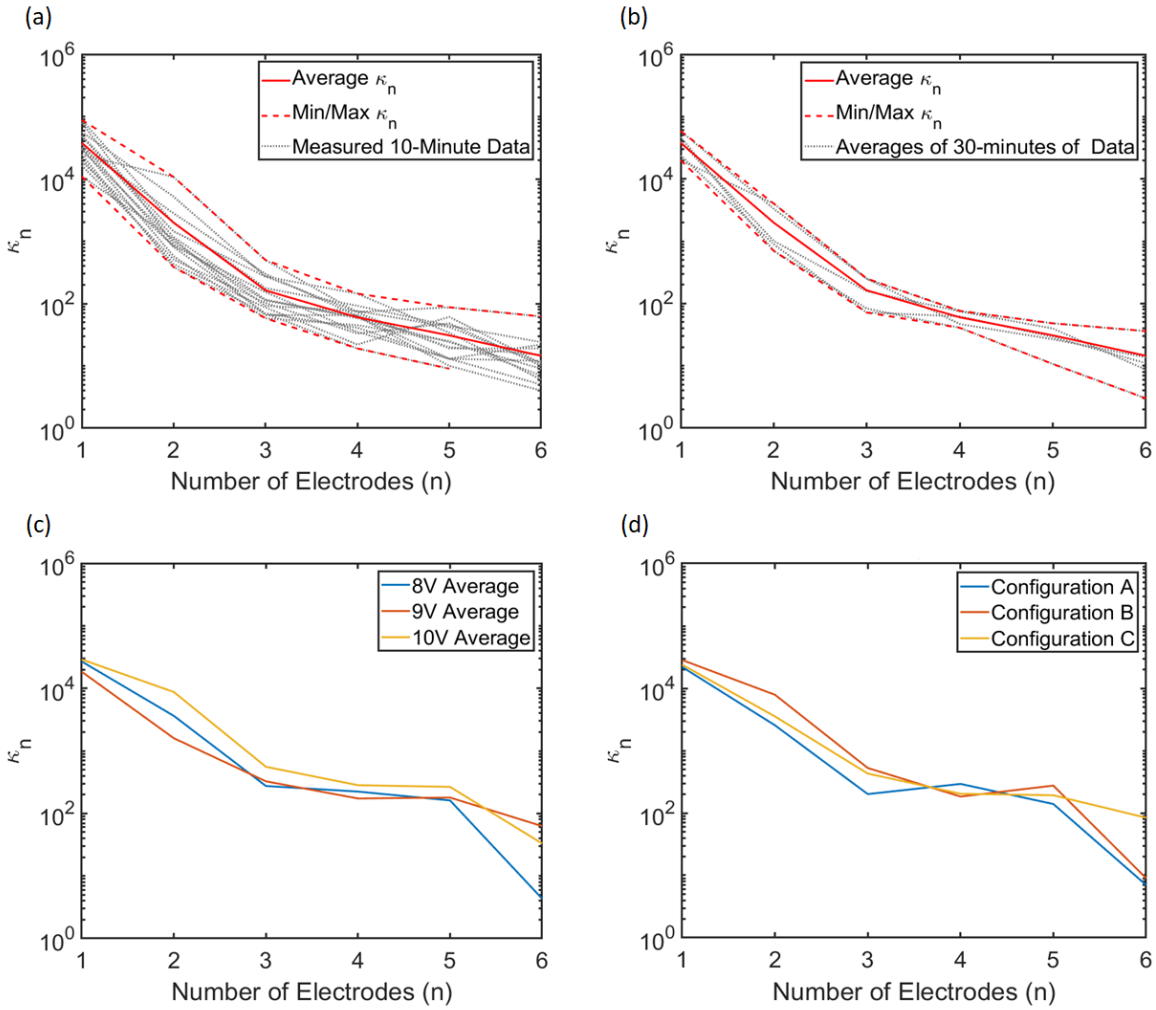

Figure 4.6: *(a) The grey curves show κ_n for 15 consecutive 10-minute segments of the same measurement ([DI, A, 10V, 1]). The solid red curve is the average of the 10-minute segments, and the dashed red curves are the minimum and maximum κ_n values across all 10-minute segments. (b) The 5 grey curves correspond to κ_n for the average of 3 consecutive 10-minute segments from (a). (c) Each curve corresponds to the average κ_n of three 10-minute measurements. Blue curve: [DI, A, 8V, 1], [DI, B, 8V, 1], [DI, C, 8V, 1]. Red curve: [DI, A, 9V, 1], [DI, B, 9V, 1], [DI, C, 9V, 1]. Yellow curve: [DI, A, 10V, 1], [DI, B, 10V, 1], [DI, C, 10V, 1]. (d) Each curve corresponds to the average κ_n for three 10-minute measurements with the same electrode configuration. Blue curve: [DI, A, 8V, 1], [DI, A, 9V, 1], [DI, A, 10V, 1]. Red curve: [DI, B, 8V, 1], [DI, B, 9V, 1], [DI, B, 10V, 1]. Yellow curve: [DI, C, 8V, 1], [DI, C, 9V, 1], [DI, C, 10V, 1].*

Device I Analysis

Figure 4.7 (a) shows κ_n for a 10-minute measurement of Device I with different event thresholds. Clearly, κ_n with a threshold of $0.67 \times |\Delta I|_{thresh}$ (red line) is slightly larger at all n, than κ_n with a threshold of $|\Delta I|_{thresh}$ (blue line). This slight increase in κ_n at a lower threshold is expected as more events (due to both small real switching events and large noise fluctuations) are observed when the event threshold is lower. Overall, the trend in κ_n is very similar for both thresholds, which indicates the choice of threshold within a reasonable range does not significantly change κ_n for Device I.

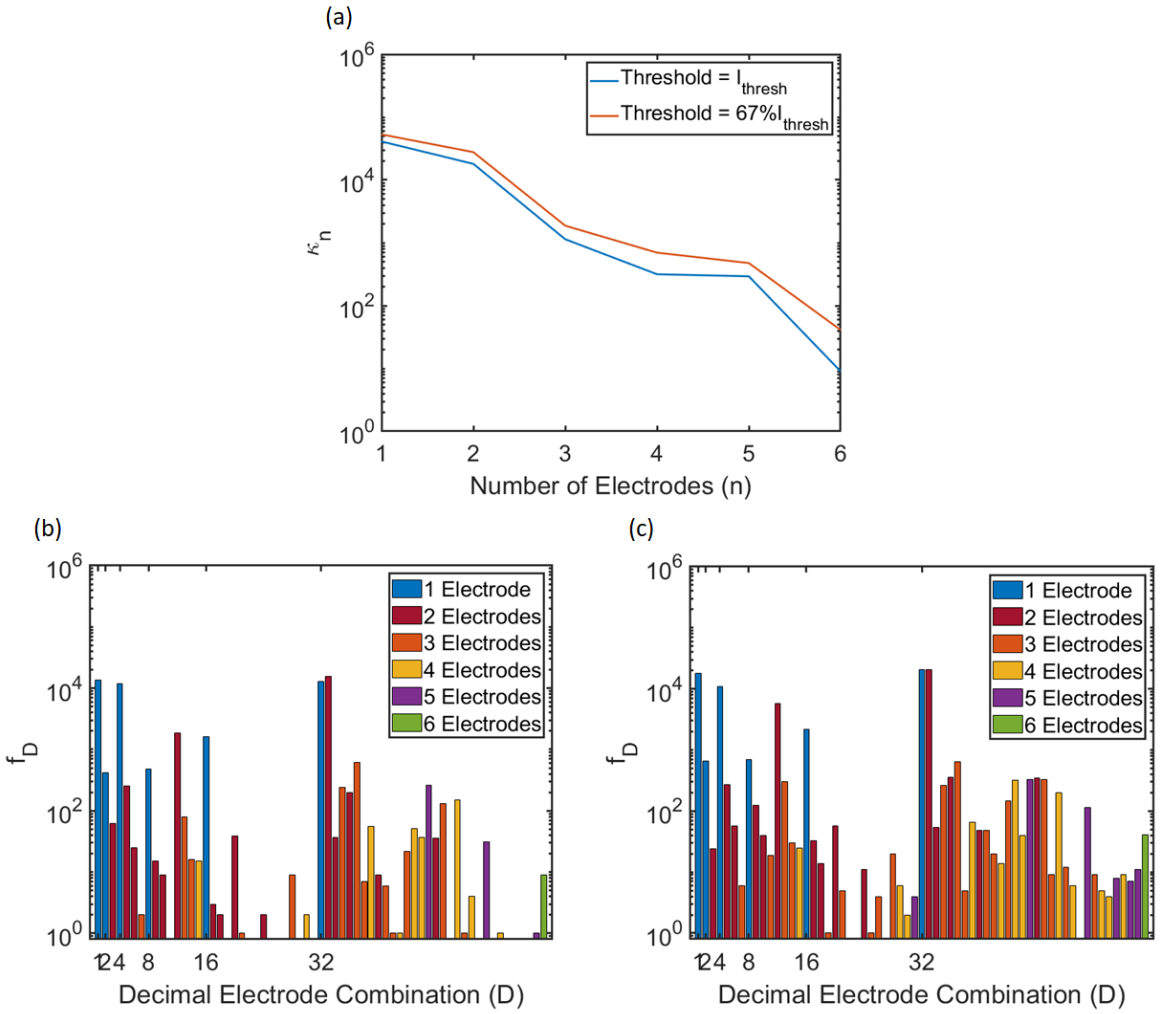

Figure 4.7: *All data is from a single 10-minute measurement of Device I ([DI, B, 10V, 1]). (a)* κ_n *with a threshold of* $|\Delta I|_{thresh}$ *(blue line), and a threshold of* $0.67 \times |\Delta I|_{thresh}$ *(red line). Clearly,* κ_n *is very similar for both thresholds. (b,c)* f_D *with a threshold of (b)* $|\Delta I|_{thresh}$*, and a threshold of (c)* $0.67 \times |\Delta I|_{thresh}$*.*

Figure 4.7 (b) and (c) show f_D for Device I with a threshold of I_{thresh} and $0.67 \times |\Delta I|_{thresh}$ respectively. Clearly, all f_D are larger when the threshold is $0.67 \times |\Delta I|_{thresh}$, compared to when the threshold is $|\Delta I|_{thresh}$. More values of f_D are non-zero when the threshold is $0.67 \times |\Delta I|_{thresh}$ (52 ± 4 non-zero f_D) than when the threshold is $|\Delta I|_{thresh}$ (40 ± 7 non-zero f_D). Therefore, events are detected at significantly more unique combinations of electrodes when the threshold is lower. This result is expected as the extra events and noise introduced to the analysis with the lower threshold are likely to lead to more events detected simultaneously at unique combinations of electrodes. Overall, the differences between Figure 4.7 (b) and (c) are relatively small, hence the threshold within a reasonable range only slightly changes f_D.

Device II Analysis

Figure 4.8 (a) shows κ_n for a 10-minute measurement of Device II with different event thresholds. Again, κ_n is slightly larger at all n for the threshold of $0.67 \times |\Delta I|_{thresh}$, than

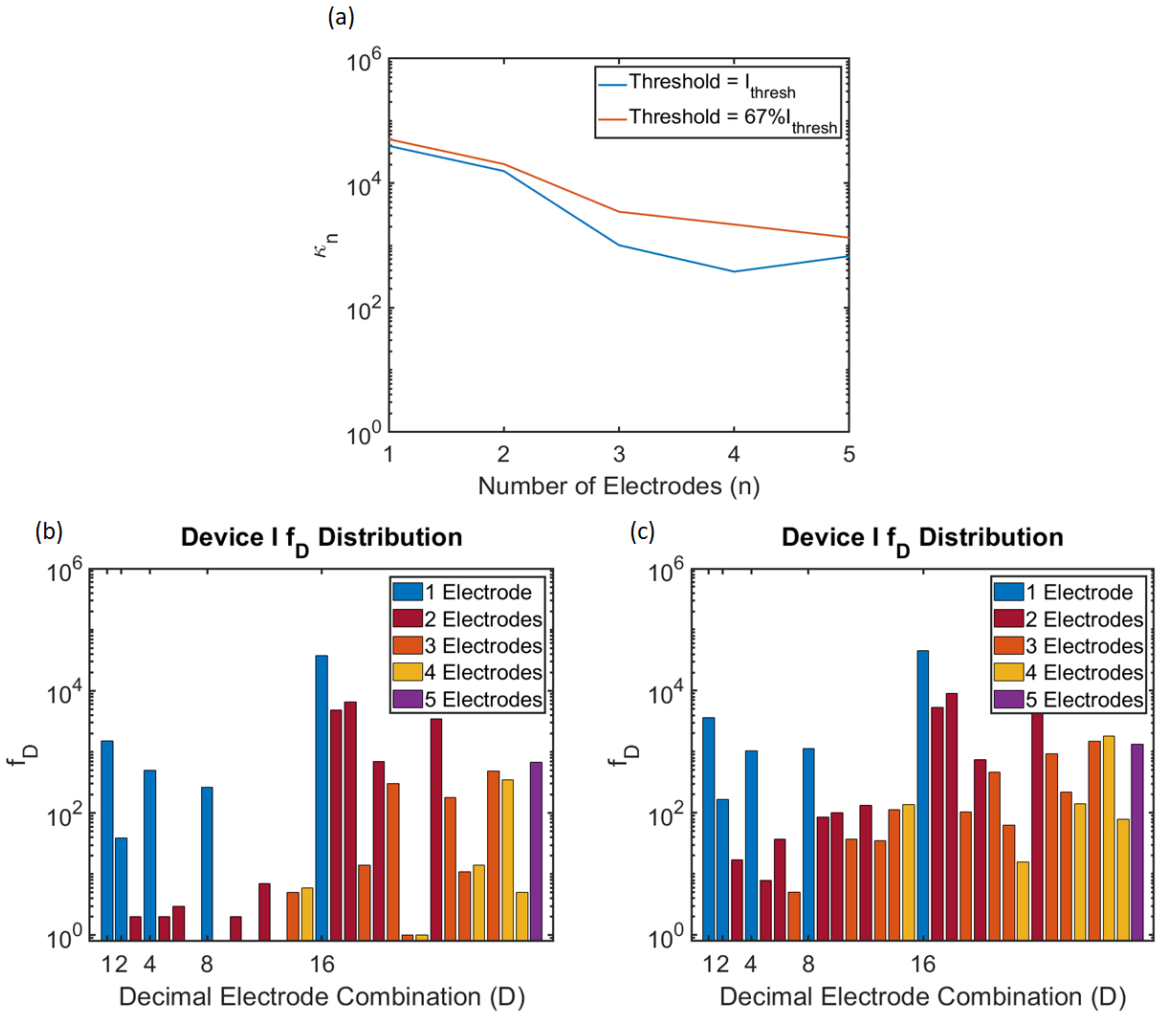

Figure 4.8: *All data is from a single 10-minute measurement of Device II ([DII, E, 8V, 1]). (a) κ_n with a threshold of I_{thresh} (blue line), and a threshold of* $0.67 \times |\Delta I|_{thresh}$ *(red line). (b,c) f_D with a threshold of (b) $|\Delta I|_{thresh}$, and a threshold of (c)* $0.67 \times |\Delta I|_{thresh}$.

for the threshold of $|\Delta I|_{thresh}$. Furthermore, the trend in the slope of κ_n is very similar for each threshold. These results strongly suggests the choice of threshold within a reasonable range does not significantly change κ_n for Device II.

Figure 4.8 (b) and (c) show f_D for 10-minutes of Device II data with event thresholds of $|\Delta I|_{thresh}$ and $0.67 \times |\Delta I|_{thresh}$ respectively. All values of f_D are noticeably larger for the lower threshold. Additionally 31 values of f_D are non-zero for the lower threshold, which implies events are detected at all possible combinations of electrodes when the threshold is $0.67 \times |\Delta I|_{thresh}$. A comparable 27 values of f_D are non-zero for data with the event threshold of $|\Delta I|_{thresh}$. Overall, f_D appears slightly more complex with the lower threshold, but the changes are not significant.

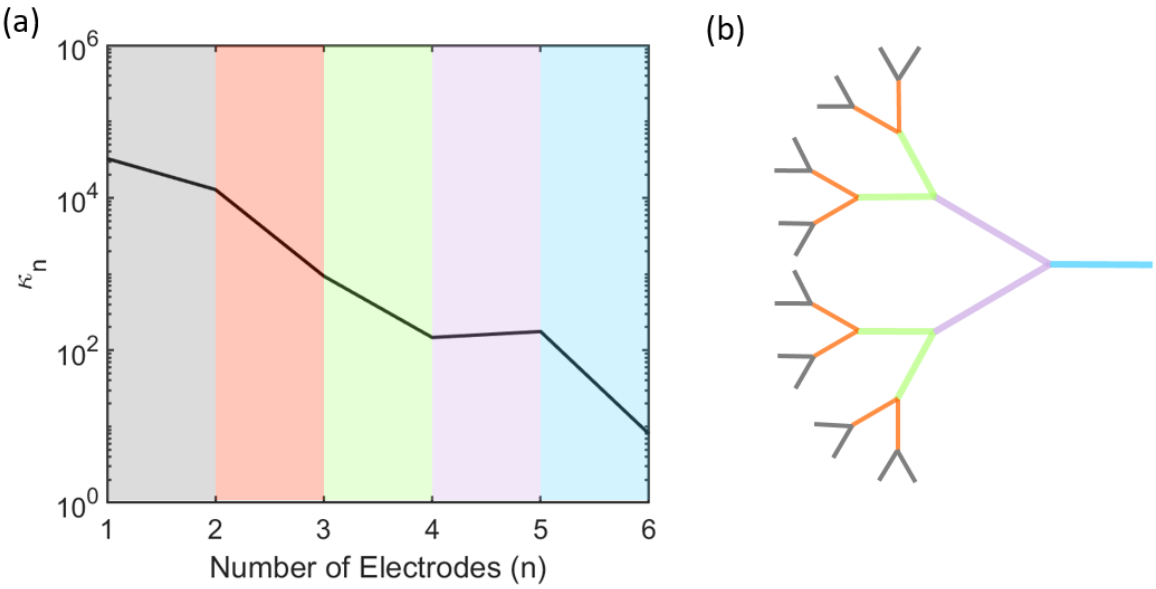

Figure 4.9: *(a) κ_n for 10-minutes of data ([DI, B, 10V]). (b) Schematic of fractal network structure. The blue branch is a low order branch, while the grey branches are high order branches. The colours correspond to the background of (a).*

4.1.7 Discussion of Experiment Analysis

Device I Summary

As shown Figure 4.4 (a), κ_n decreased approximately exponentially as n increased. Hence, many isolated events were detected, and relatively few events were simultaneously detected at all electrodes. The range of values of κ_n can be explained as follows. In principle, all switching events should be observed at all electrodes. However, a different magnitude change in I should be observed at each electrode due to differences in the connectivity between switching sites and the electrodes. In practice the noise and threshold prevent the observation of some events, and hence very few events are detected at all electrodes. The observed decrease in κ_n then relates to the fractal structure of PASNs. Many switching sites are on high-order branches of the fractal, while relatively few switching sites are on low-order branches [17]. Switching events on high-order branches cause small changes to the current throughout the network, hence these events are likely detected at relatively few electrodes and contribute to κ_n for small n. In contrast, events on low-order branches cause large changes in current throughout the network, thus these events are likely observed simultaneously at multiple electrodes and contribute to κ_n for large n. There are many more switching sites on high-order branches than low-order branches, hence the observed κ_n is consistent with the underlying fractal structure of PASNs. Figure 4.9 (a) shows κ_n for a 10-minute measurement of Device I with a colour coded background for each value of n. Figure 4.9 (b) shows a schematic of a fractal network structure that is colour coded to highlight the branch of the network each part of κ_n likely corresponds to.

As shown in Figure 4.6 (c) and (d), κ_n for Device I did not change significantly when different voltages were applied, or when different input configurations were used. The similarity between κ_n at different voltages indicates that the applied voltage does not significantly

change the relative number of events on high order branches, compared to the number of events on low order branches of the network. Additionally, the similarity between κ_n with different input configurations suggests the network structure is similar between different sets of electrodes. Overall, these results indicate that κ_n is characteristic of the network structure of PASNs.

As shown in Figure 4.4 (b), many values of f_D were non-zero. This result is expected because events occur in many different tunnel gaps of the PASN throughout a measurement [15]. Events in different tunnel gaps will cause the current in the network to redistribute differently. For example, a switching event on a high-degree branch will cause the current in the network to redistribute differently to an event on a low-degree branch of the network. Therefore, events that are detected at different combinations of electrodes likely occurred at different tunnel gaps. Hence, the many non-zero values of f_D indicate many different tunnel gaps were active in the measurement of interest. Moreover, a wide-range of active tunnel gaps is a sign that PASNs exhibit complex patterns of switching activity.

Device II Summary

For Device II, many values of f_D are non-zero, which is similar to f_D for Device I. This result suggests that different tunnel gaps are active in Device II.

As shown in Figure 4.5 (a), κ_n decreased relatively slowly compared to Device I (Figure 4.4 (a)), and a significant number of events were simultaneously observed at all electrodes. This result agrees with the measured current at each electrode in Figure 4.3 (a) and (b), which shows many events detected at many electrodes simultaneously. Furthermore, the change in current at each electrode of Device II is qualitatively similar, which is very different to the behaviour observed for Device I (Figure 4.2). These observed differences between Device I and Device II suggest that Device II is somewhat more connected than Device I. In a highly connected device, few tunnel gaps are present, and each electrode is well-connected to each tunnel gap. Hence, when an event occurs, all electrodes will measure a significant change in current. In contrast, a poorly connected network has many tunnel gaps, and each electrode is well connected to relatively few tunnel gaps. Hence, any given switching event will cause a significantly greater change in current at the electrodes that are well connected to the tunnel gap of interest, than the other electrodes. Therefore, a events will often be observed at many electrodes simultaneously in a highly connected device, whereas events will often be observed at relatively few events simultaneously in a poorly connected device. Hence, the qualitative results for Device I and Device II can be explained by Device II being better connected than Device I.

It is important to compare the experimental analysis with simulations to check the data is representative of PASNs. Hence, the next section analyses simulations of PASNs for comparison to the analysis presented in this section.

4.2 Simulation Data

This section presents a qualitative analysis of simulated PASNs, which will be compared to the experimental analysis in Section 4.3. All simulations in this section (general details in

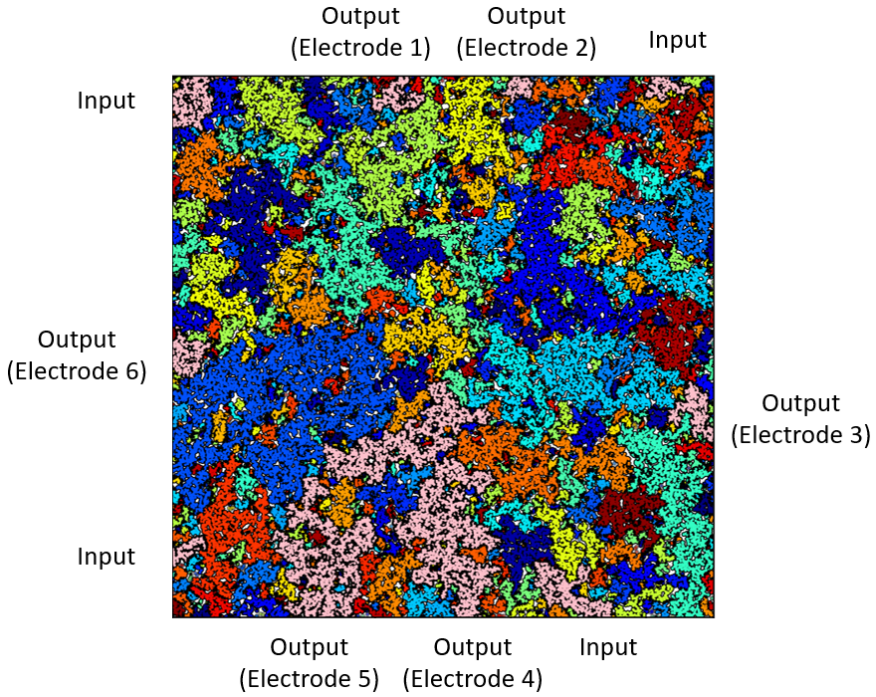

Figure 4.10: *Network structure for a simulated PASN. Each colour represents a group of nanoparticles that have Ohmic connections between them. The pink groups act as input and output electrodes and are labelled accordingly. The electrode configuration was chosen to mimic the input electrode configurations of Device I (Figure 3.6).*

Section 2.5) have a network size of 200×200 particle diameters. Four groups of nanoparticles (NP) act as input electrodes with an applied 3V DC bias, and six different groups of NPs act as output electrodes which are grounded. Figure 4.10 shows a diagram of the simulated network. Each colour corresponds to a group of NPs which have Ohmic connections between them. Neighbouring groups are separated from one another by tunnel gaps. The pink coloured groups are the input and output electrodes, which are arranged similarly to the electrodes in the experiments.

Several simulations were analysed with different parameters to change the event density. The event density for a segment of data is defined as the percentage of total time-steps in the segment with at least one event detection.

Section 4.2.1, Section 4.2.2, and Section 4.2.3 focus on the simulation with the best results (~10% event density with no threshold). The analysis of other simulations is briefly discussed to demonstrate the reliability of the analysis. Note that the data analysed is the current calculated at the output electrodes. The simulation is not subject to measurement noise, and so events are initially defined as a change in current of any magnitude. Later, a threshold is introduced for comparison to the experiments (Section 4.2.3). The first 100,000 time-steps of all simulations are ignored to avoid transient events while the simulation approaches steady-state activity [101].

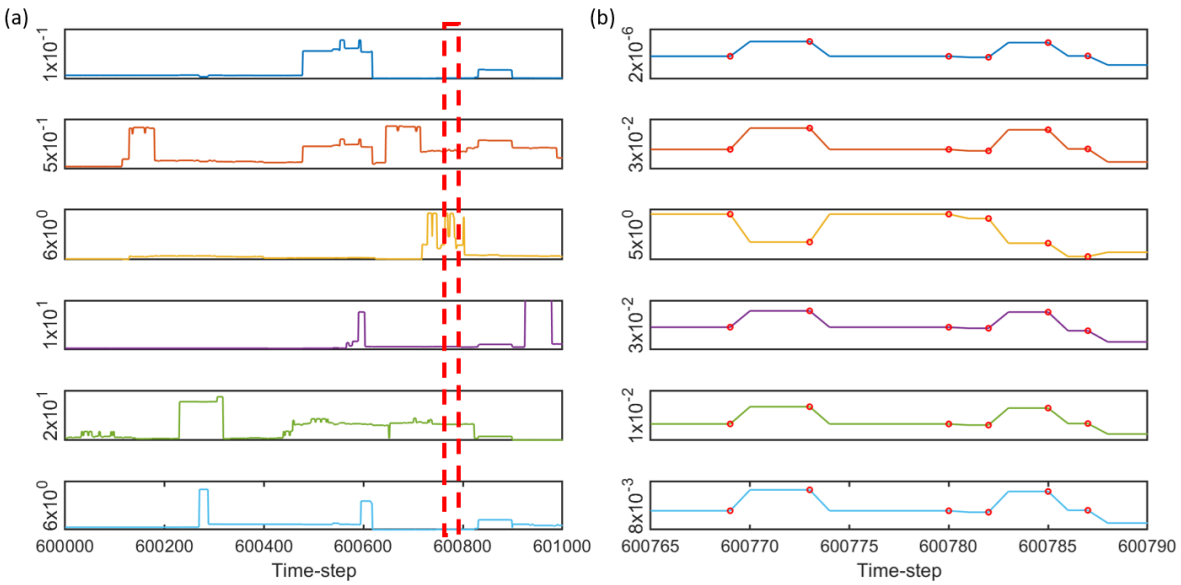

Figure 4.11: *Current (arbitrary units) for the simulated PASN across 1,000 time-steps (a) and 25 time-steps (b). Each panel shows the data from one electrode, with the vertical ranges labelled. (a) At the presented scale, the data appears complex. The red dashed region is magnified in (b). (b) Red circles indicate the detected events. Clearly, all events are observed on all electrodes which suggests the data is not complex. Note the range of vertical scales.*

4.2.1 Raw Data

Figure 4.11 (a) shows a 1,000 time-step segment of current data for the simulated PASN. The panels from top to bottom correspond to the current calculated at each electrode in numerical order. That is, the top panels show data for electrode 1 and the bottom panels show data for electrode 6. At the scale presented in Figure 4.11 (a), the majority of the changes in current are qualitatively different at each electrode. Note that there are a few exceptions where the measured changes at multiple electrodes are qualitatively similar. For example, the data calculated at electrodes 1 and 2 is similar between time-steps 600,480 - 600,620. However, such qualitative similarities are relatively infrequent in the simulated data.

The region within the red dashed box shown in Figure 4.11 (a) covers 25 time-steps and is shown in Figure 4.11 (b). Note that the vertical scales vary over six orders of magnitude in Figure 4.11 (b), therefore the changes in current calculated at electrode 1 are significantly smaller than the changes in current at electrode 3. Clearly, all events (red circles) were detected at all electrodes, despite the apparent differences between electrodes in Figure 4.11 (a). This result is evidence that all switching events cause a change in current at all electrodes.

4.2.2 Raw Data Summary

At the scale shown in Figure 4.11 (a), the switching activity of the simulation appears complex. However, the simulations are not subject to noise, and so all switching events are

detected at all electrodes, as shown in Figure 4.11 (b). Therefore, the analysis applied in Section 4.1 is trivial for the raw simulation data.

To analyse the simulation data for comparison to the experiments, a global event threshold is applied in the next section. The threshold emulates the noise as all events below the threshold (noise) are not detected. The threshold is the same for all electrodes. Different thresholds are referred to by the percentage of events across all electrodes that are below the threshold.

4.2.3 Analysis with Global Thresholds

Figure 4.12 (a) shows κ_n for 600,000 time-steps of simulated data with different global event thresholds (solid lines). Segments of 600,000 time-steps were analysed because 600,000 datapoints were analysed in the 10-minute experimental measurements with at a 1kHz sampling rate (Section 4.1.3). κ_n with a 20% global threshold (red curve), has a maximum at $n = 6$, which indicates many events are detected at all electrodes. When a 60% global threshold is applied, the slope of κ_n is roughly flat from $n = 3$ to $n = 6$, which is significantly different to κ_n for 10-minutes of experimental data (dashed lines). The slope of κ_n for data with an 80% global threshold is roughly similar to κ_n for the experiments. Hence, a good approximation to the experimental noise level is achieved by a global threshold that excludes the smallest 80% of events. κ_n for the 90% global threshold decreases slightly faster than κ_n for the experiments.

Figure 4.12 (b) shows κ_n for ten consecutive 600,000 time-step segments of the simulation with 80% global event thresholds (grey lines). The average κ_n (solid red line) and maximum and minimum κ_n (dashed red lines) are also shown. Clearly, there is very little variation between the 600,000 time-step segments. Furthermore, the variation in κ_n for the simulation is much less than for κ_n for 10-minutes of experimental data (Figure 4.6 (a)).

Figure 4.12 (c) and (d) show f_D for 600,000 time-steps of simulated data (same data as Figure 4.12 (a)) with an 80% and 90% global event threshold respectively. The 80% global event threshold had 62 ± 1 non-zero values of f_D, while the 90% global event threshold had 40 ± 2 non-zero values of f_D. The variation was calculated from the ten consecutive segments of simulated data shown in Figure 4.12 (b).

Analysis of Different Simulations

This section briefly investigates how the analysis changes for simulations with different overall event densities. New simulations were created that used the same NP groups and electrode configuration, but with different rates of filament formation and destruction, which changes the event density of the simulation. Note that each simulation is referred to by the event density with no threshold applied.

Figure 4.13 shows κ_n for 600,000 time-steps of simulations with ~5%, ~10%, and ~18% overall event densities. The presented data and the event densities are for an 80% global event threshold. Note that the ~10% overall event density simulation is the same simulation analysed in Figure 4.12. Clearly, κ_n is qualitatively similar for each of the simulations

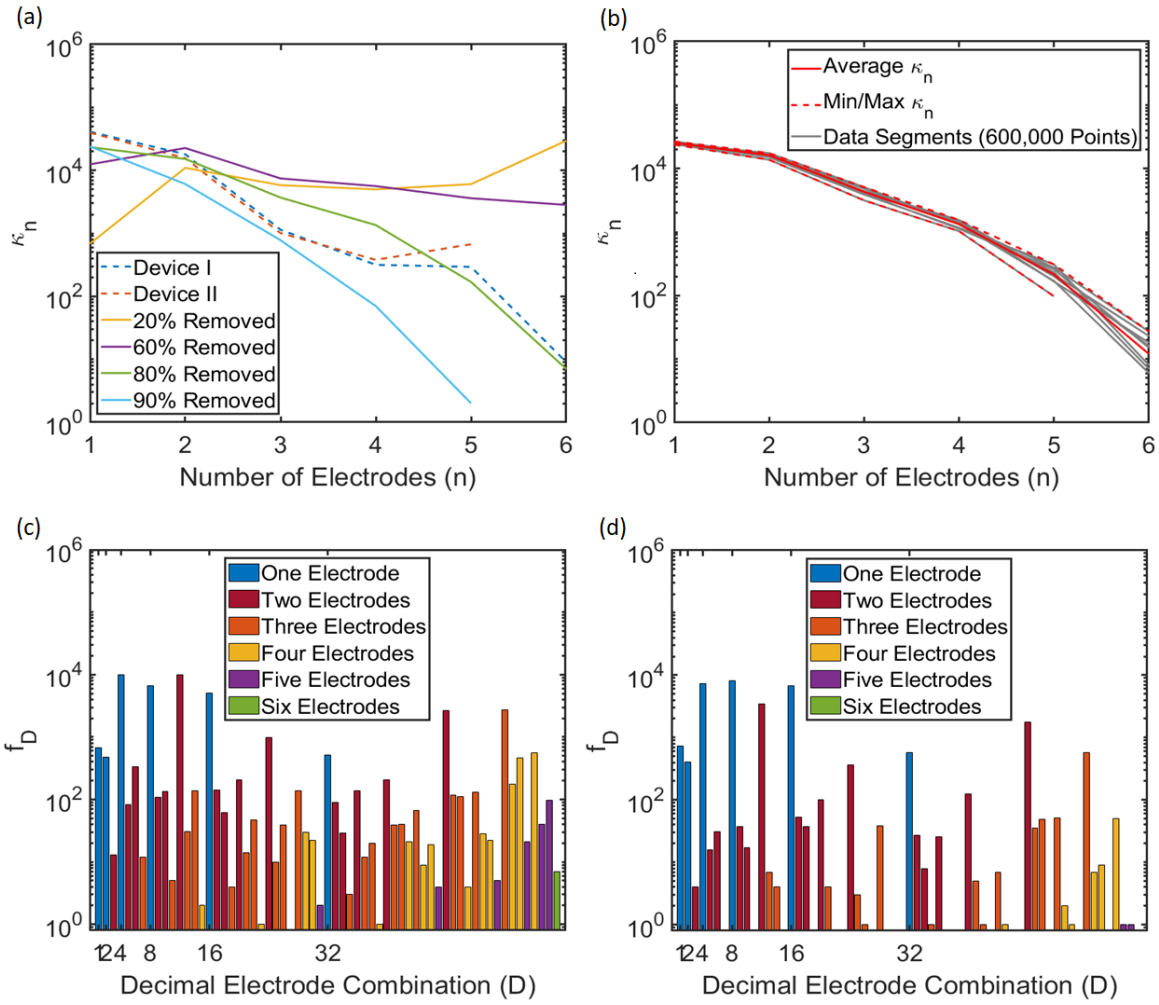

Figure 4.12: *Qualitative analysis of a simulated PASN (10% event density with no threshold) with different global event thresholds. (a) The blue and red dashed line correspond to κ_n for Device I ([DI, B, 10V, 1]) and Device II ([DII, E, 8V, 1]) respectively. The solid lines correspond to κ_n for 600,000 time-steps of the simulated PASN with the smallest x% of events removed by different global thresholds. (b) The grey lines show κ_n for ten consecutive segments of 600,000 time-steps with 80% global thresholds applied to the data. The red solid line shows the average κ_n of the grey segments, while the dashed red lines show the minimum and maximum κ_n values of the grey lines. (c,d) f_D for 600,000 time-steps of the simulation when the smallest 80% (c) and 90% (d) of events are removed by a global threshold. The data in (c) and (d) is the same as the data for (a).*

analysed, regardless of the event density. This result suggests the analysis in Section 4.2.3 is reliable and is representative of a range of simulation parameters.

4.2.4 Comparison of Simulations and Experiments

As shown in Figure 4.12 (a), κ_n for 10-minutes of Device I and Device II data is very similar to κ_n for simulated data with an 80% global threshold. This result strongly suggests that a global event threshold which eliminates 80% of events is a good approximation to the measurement noise in the experimental data. Furthermore, this approximate equivalence

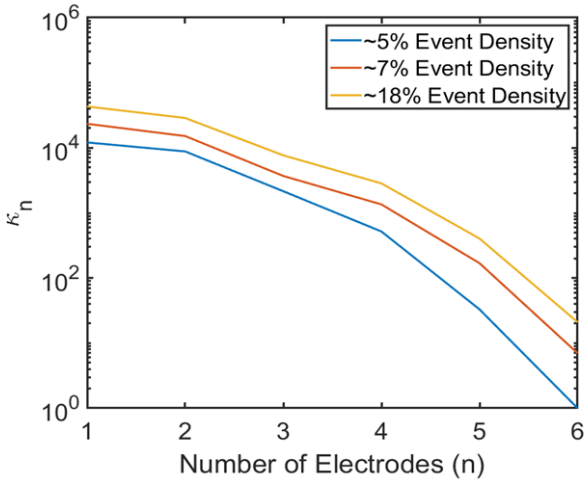

Figure 4.13: *κ_n for 600,000 time-steps of three different simulations with 80% global event thresholds. The red curve shows κ_n for the simulation analysed in (a), which has ~10% overall event density. The blue curve shows κ_n for a simulation with ~5% overall event density. The yellow curve shows κ_n for a simulation with ~18% overall event density. Note that each simulation had the same NP groups and electrodes, and that only the rate of filament formation and destruction were modified to achieve the new event densities.*

between global threshold and noise, implies that a significant proportion of the events in the experiments are obscured by the measurement noise. However, note that other factors, such as the size of the network for the simulation and the switching model, likely affect the size of the global threshold. Hence, the proportion of events in the experiments below the noise level is not necessarily 80%.

The number of non-zero values of f_D is in good agreement between the simulation with an 80% global threshold and Device I (Section 4.1.5). Therefore, a similar number of unique combinations of electrodes detected at least one event for the simulation and Device I data. This result further supports the use of an 80% global threshold to approximate the measurement noise. Overall, the analysis for the simulation was similar to the analysis for the experiments, which indicates the analysis of Device I and Device II is a good representation of PASNs.

4.3 Summary of Qualitative Complexity Analysis

The aim of this chapter was to determine whether PASNs exhibit qualitatively complex switching dynamics. The relationship between switching events observed on different electrodes was analysed through the κ_n and f_D values. κ_n for experimental data was clearly impossible to be produced by random processes. Additionally, κ_n was consistent with the underlying fractal network structure. Moreover, many values of f_D were non-zero, which suggests many tunnel gaps were active throughout the measurements. Furthermore, the patterns of correlations observed in the raw data for Device I changed over time. Therefore, the qualitative features of the data strongly indicate the switching activity of PASNs is complex.

The validity and reliability of the analysis in this chapter was tested through analysis of different measurement conditions, event thresholds, and by comparison to simulation data. Overall, the analysis of the experiments did not change significantly with different measurement conditions or thresholds. Furthermore, the simulation analysis was qualitatively similar to the analysis of the experiments. It will be important to analyse future devices for further evidence of the reliability of the analysis presented in this chapter.

The analysis in this chapter only provides a qualitative view of complexity in PASNs. In order to determine whether the complexity is similar to complexity in the brain, it is essential the complexity is quantified. Chapter 5 presents the quantitative analysis of the complexity in PASNs.

Chapter 5

Neural Complexity

Chapter 4 presented qualitative evidence for complexity in PASNs. It is essential to quantify this observed complexity in order to meaningfully compare PASNs with the brain. One promising metric is *neural complexity*, which was first proposed in [106]. Neural complexity is an information theoretic measure developed to quantify the global and local interactions of neurons in the brain [106, 107]. Note that slight revisions were made to neural complexity in [1], which is the definition followed in this chapter.

This chapter presents the neural complexity analysis of multi-electrode (MC) PASNs. Section 5.1 defines neural complexity and presents a simple model to provide intuition for the equations. Section 5.2 describes the key steps of the complexity analysis procedure. Section 5.3 shows the results of the analysis of experimental and simulation data. Section 5.4 compares the complexity of PASNs to the complexity of the biological data in [1]. Finally, Section 5.5 briefly summarises the results of this chapter.

5.1 Definitions

This section defines the relevant quantities required for the complexity analysis, and provides schematic examples to illustrate the procedure developed in [1]. At the end of the section, a simple model is used to illustrate types of data which have high and low neural complexity.

5.1.1 Event Raster

The complexity is calculated with the *event raster*, X, which is the set of all event detections at each electrode in the dataset of interest. Figure 5.1 (a) shows an example of X for a dataset with four output electrodes. Each row of X is the event train for a different electrode, and the coloured rectangles represent the detection of an event at time t ($E_i(t) = 1$).

The *combined state* of all event trains at time t is given by x. That is, x represents the combination of electrodes that simultaneously detected an event at time t. Figure 5.1 (b) shows four examples of x.

The complexity requires the calculation of relevant quantities for many subsets of the event raster. Each subset can be written as X_j^k, which refers to the j^{th} unique subset of k rows (event trains) from X. For example, X_1^2 is the first set of two rows, which is equivalent

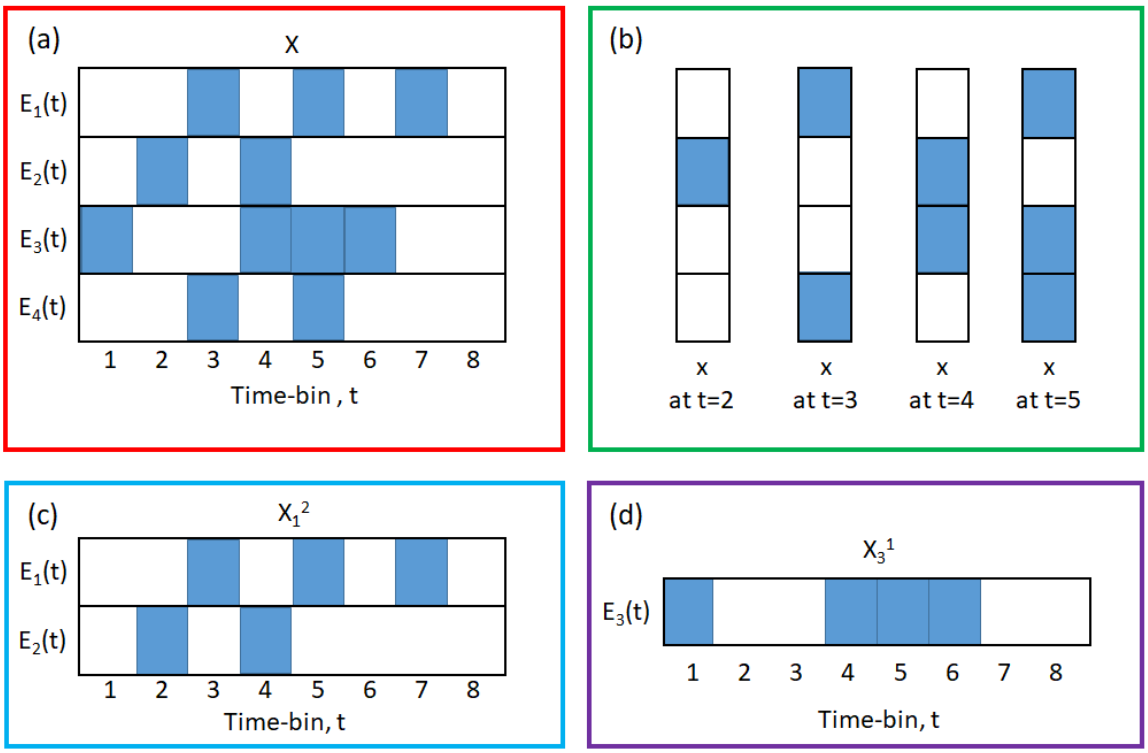

Figure 5.1: *Examples of the data used to define neural complexity. (a) Event raster, X, for four electrodes over 8 time-bins. Each blue rectangle represents a 1 (the detection of an event), and each blank rectangle represents a 0 (no event detection). (b) Four examples of combined states (x) of all event trains at a given time. (c) The subset of X given by the first two rows of X (X_1^2), i.e. the first two event trains. (d) The subset of X given by the third row of X (X_3^1), i.e. the third event train only.*

to the first two event trains in X. Similarly, X_3^1 is the third set of one row of X, which is equivalent to the third event train only. Figure 5.1 (c) and (d) show X_1^2 and X_3^1 respectively for X in Figure 5.1 (a). Note that j ranges from 1 to $C(N,k)$ (combinations of k objects in a set of N total objects). For example, for a set of 4 electrodes, there are 6 combinations of k=2 electrodes, hence j ranges from 1-6. In this way, X_j^k can define all subsets of electrodes in X.

5.1.2 Entropy

Neural complexity depends on the entropy [108, 109] of the event raster which is given by

$$H(X) = -\sum_{x \in X} p(x) log_2(p(x)) \tag{5.1}$$

where $p(x)$ is the probability that a given combined state of event trains is x. In the complexity analysis, $p(x)$ is calculated as the total number of occurrences of x in the dataset, divided by the total number of time-bins in the dataset. For example, $p(x) = 1/8$ for the combined state at t = 2 time-bins in Figure 5.1 (a). The value of $p(x)$ is assumed to be stationary for each dataset. Note that a base 2 logarithm is used in Equation 5.1 to ensure

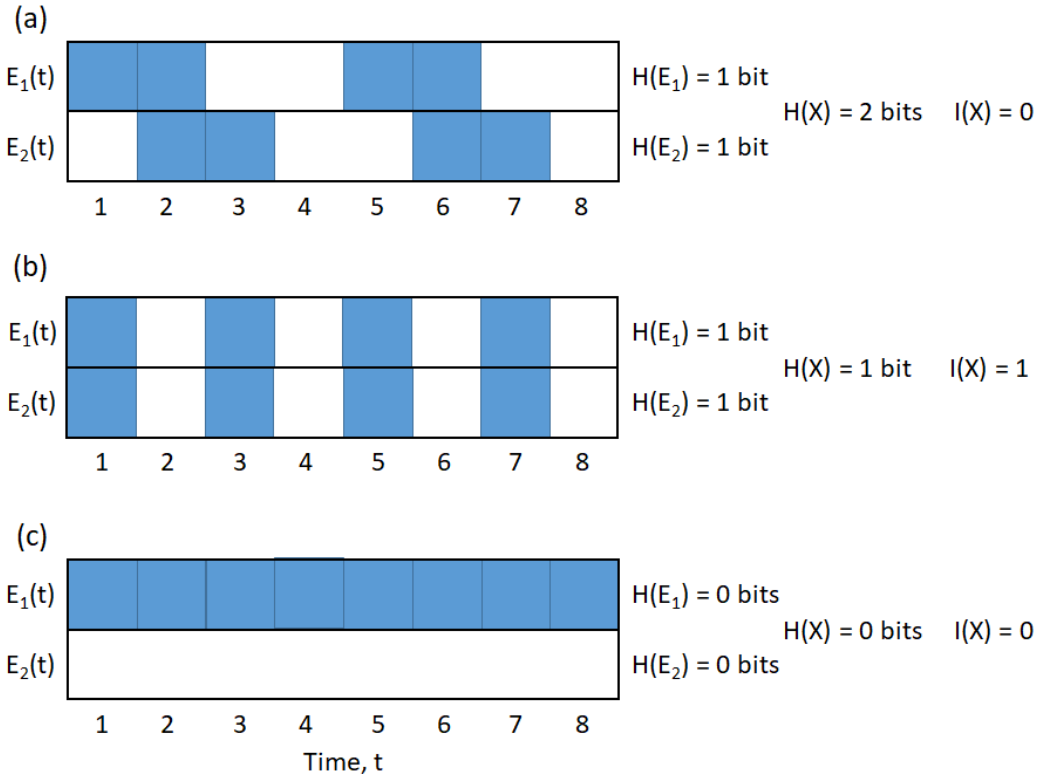

Figure 5.2: *Simple examples of event train rasters. A blue square represents an event at time t, and a blank square represents no event. The relevant entropies (Equation 5.1) and integrations (Equation 5.3) are shown next to each raster. (a) H(X) is maximised as each possible value of x has probability* $p(x) = 1/4$*. Moreover, the entropy of each event train* $H(E_i)$ *is maximised as* $p(x) = 0.5$ *for each possible value of x. (b) H(X) is low as* $p(x) = 0.5$ *for the two values of x shown. However,* $H(E_i)$ *is maximised as* $p(x) = 0.5$ *for each possible value of x. (c) H(X) is minimised as* $p(x) = 1$*. Additionally,* $H(E_i)$ *is minimised as only one value of x is shown for each event train with probability* $p(x) = 1$*.*

that the units of entropy are in bits [110].

The entropy of subsets of X can also be calculated according to 5.1

$$H(X_j^k) = -\sum_{x \in X_j^k} p(x) log_2(p(x)) \tag{5.2}$$

where x represents a given combined state of the subset of X.

H(X) is a measure of the disorder of X. H(X) is large when many different values of x are observed with similar frequency, and small when very few different values of x are observed. Figure 5.2 (a), (b), and (c) show simple examples of X for which H(X) is at a maximum, intermediate, and minimum value respectively. Note that entropy is large when many different combined states are observed. The entropies of the individual event trains, H(E_i), are also labelled in Figure 5.2 (a), (b) and (c).

5.1.3 Integration

The integration [1], I(X), is defined as

$$I(X) = \left(\sum_i H(E_i)\right) - H(X) \tag{5.3}$$

where the summation is over all event trains in X. Figure 5.2 (a) shows an example for which $I(X) = 0$, because H(X) is maximised, and each H(E_i) is maximised. Figure 5.2 (c) shows another example of $I(X) = 0$, because the entropy is zero for each event train. In contrast, Figure 5.2 (b) shows an example of non-zero I(X), because the entropy of each event train is maximised, while the entropy of X is at an intermediate value. Therefore, I(X) is high when individual event trains are highly disordered, but the combined state of several event trains is highly ordered. That is, integration measures the degree of coordination between groups of event trains compared to how random each individual event train is.

The integration of a subset of X can be calculated similarly to Equation 5.3

$$I(X_j^k) = \left(\sum_i H(E_i)\right) - H(X_j^k) \tag{5.4}$$

where the summation is only over the event trains in the subset X_j^k.

5.1.4 Neural Complexity

Neural complexity, $C_N(X)$, is a measure of the coordination of X across all subsets [1]. $C_N(X)$ is given by

$$C_N(X) = \frac{1}{N}\sum_{k=2}^{N}\left[\left(\frac{k-1}{N-1}\right)I(X) - \langle I(X_j^k)\rangle_j\right] \tag{5.5}$$

In Equation 5.5, the $\langle I(X_j^k)\rangle_j$ term is the average integration across all possible subsets of k event trains in X. The $(k-1)/(N-1)I(X)$ term in Equation 5.5 is a linear approximation to $\langle I(X_j^k)\rangle_j$ for each subset of k event trains (see red dashed lines in Figure 5.3 (c), (e), and (g)). Therefore, the summation compares a linear approximation to the integration for each subset of X with k event trains, to the true average integration for each subset of X with k event trains [1]. Equation 5.5 can be difficult to intuitively understand, hence the next section presents a simple model to clarify it.

5.1.5 Complexity of a Simple Chain Model

To understand Equation 5.5, we consider the simple chain model that is described in [1]. The model consists of 12 'neurons', arranged in a chain such that each neuron influences the next neuron in the chain. Figure 5.3 (a) shows a simple schematic of the chain model. Each neuron can either spike or not spike at any given time-step. The spiking state of the

ith neuron is referred to as a_i. The spiking state of the $i+1th$ neuron depends on the ith neuron according to

$$\begin{aligned} p(a_{i+1} = a_i) &= 0.5(1+c) \\ p(a_{i+1} \neq a_i) &= 0.5(1-c) \end{aligned} \tag{5.6}$$

where c is a parameter that determines the complexity of the model. When $c = 1$, all neurons mimic the spiking state of the first neuron, whereas, when $c = 0$, the spiking states are entirely random. Note that the chain model has no time dependence, and the state of the first neuron alternates between time-steps.

Figure 5.3 (b), (d), and (f) show representative segments of the event rasters (X) for the chain model when $c = 1$, $c = 0.8$, and $c = 0$ respectively. Note that each row represents the spiking of one neuron for this model. Clearly, Figure 5.3 (b) shows completely ordered data with no variability, while Figure 5.3 (f) shows completely random data. Figure 5.3 (d) shows each neuron is typically the same as the previous neuron in the chain (not in time), but there is sufficient variability for each neuron to be different to its predecessor. That is, Figure 5.3 (d) is an intermediate state between totally ordered and totally random.

Figure 5.3 (c), (e), and (g) show the linear approximations to the integration as a red line (first term in summation of Equation 5.5), and the average integration at each subset size as a blue curve (second term in summation of Equation 5.5), for the chain model with $c = 1$, $c = 0.8$, and $c = 0$ respectively. The complexity is the area between the red and blue curves (grey region).

Figure 5.3 (c) shows high I(X) because of the high degree of order in the data at $c = 1$ (similar to Figure 5.2 (b)). Note that the red and blue lines perfectly overlap, hence the complexity is zero. In contrast, Figure 5.3 (g) shows the integration is approximately zero for random data, because the entropy of X is maximised for all subsystem sizes (similar to Figure 5.2 (a)). The low integration causes the complexity to be approximately zero.

Figure 5.3 (e) shows I(X) is non-zero for $c = 0.8$, and that the integration increases non-linearly (blue curve) with subset size. This non-linearity suggests that the degree of coordination changes as the subset size increases. That is, larger subsets of X are increasingly coordinated, while smaller subsets of X are increasingly random. It is this non-linearity in the integration that leads to a non-zero complexity for the chain model when $c = 0.8$.

Overall, the chain model shows that neural complexity is approximately zero for both random data and ordered data. Hence, complex data requires a mix of coordination and variability, which results in a non-linear integration curve.

5.2 Analysis Procedure

This section details the procedure used to calculate the complexity of data from PASNs. The procedure is largely the same as that used in [1], to allow for the best comparison between PASN data and biological data.

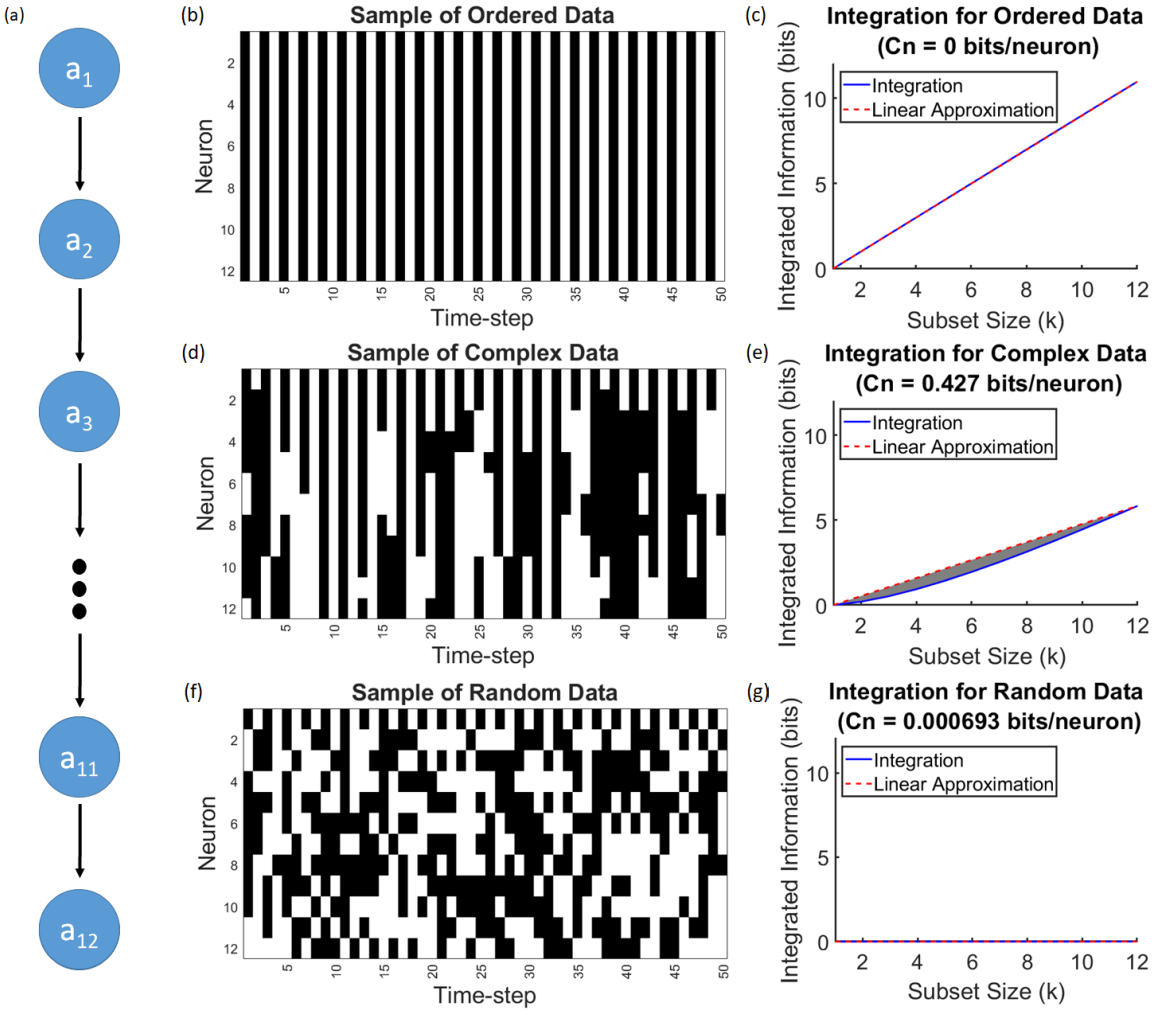

Figure 5.3: *(a) Schematic of the chain model. Each circle represents a neuron and the a_i represent the spiking state of the neuron. The arrows show how the neurons interact, hence a_{i+1} depends entirely on a_i. (b, d, f) Representative rasters of the chain model for $c = 0$, $c = 0.8$, and $c = 1$ respectively. A black square in row i column j means that neuron i spiked ($a_i = 1$) at time-step j, whereas a white square means that neuron i did not spike ($a_i = 0$) at time-step j. The state of a_i was chosen to alternate with each time-step. (c, d, e) Average subset integration (blue lines) and linear approximation to the integration (red dashed lines) for the chain model when $c = 1$, $c = 0.8$, and $c = 0$ respectively. The neural complexity, C_N is given by the area between the average subset integration and the linear approximation to the integration. The presented results in (c, e, g) are for the chain model with 12 neurons over 100,000 time-steps.*

5.2.1 Binning the Data

For experimental and simulation PASN data, the raster of event trains is binned before calculation of the complexity. The binning procedure here is the same as the procedure in [1]. The bin size is given by the average inter-event interval (IEI) for the overall event train, $E_0(t)$. The overall event train is defined by

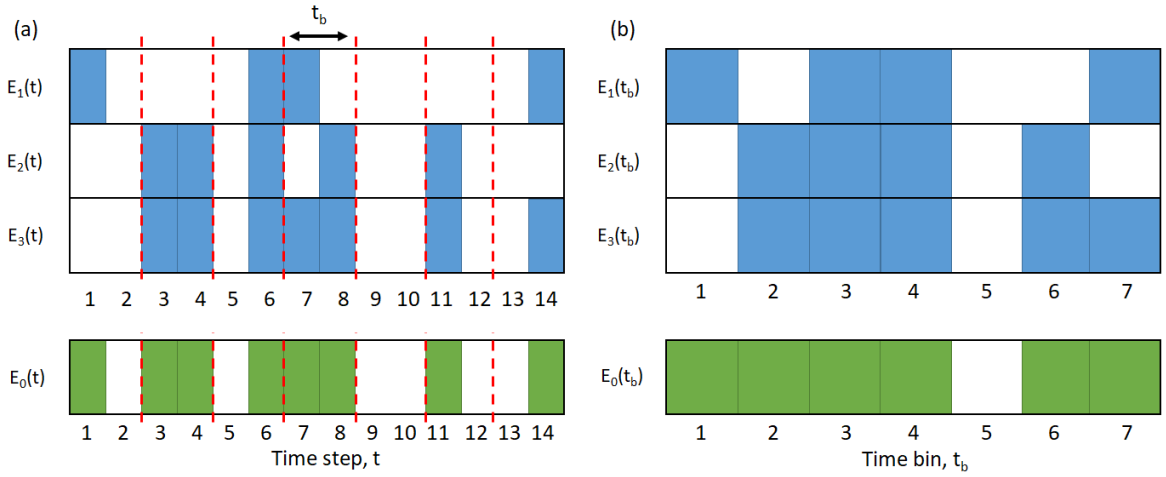

Figure 5.4: *Diagram of the event train binning process. The coloured squares represent the detection of an event at a given time-step or time-bin. (a) At the top, the event trains for three electrodes, $E_i(t)$ are shown. These event trains are converted into the overall event train, $E_0(t)$, defined by Equation 5.7. The average IEI for $E_0(t)$ is 2 time-steps as shown by the red dashed lines. (b) The binned event trains corresponding to (a). $E_i(t_b) = 1$ if $E_i(t) = 1$ for any t within the time-bin t_b. Note that all time-bins with no events are ignored in the complexity analysis, hence time-bin 5 is removed before the next step of the analysis procedure.*

$$E_0(t) = \begin{cases} 1 & \text{if} \sum_i E_i(t) > 0 \\ 0 & \text{otherwise} \end{cases} \tag{5.7}$$

Figure 5.4 (a) shows a set of three event trains, $E_i(t)$, and the corresponding overall event train, $E_0(t)$ (green rectangles). Note that the maximum value of $E_0(t)$ is 1. Hence, $E_0(1) = 1$ and $E_0(3) = 1$, despite $\sum_i E_i(1) = 1$ and $\sum_i E_i(3) = 2$. The average IEI of the overall event train (i.e. average time between $E_0(t) = 1$) is 2 time-steps and is indicated by the red-dashed lines.

Figure 5.4 (b) shows the binned event trains corresponding to Figure 5.4 (a). Each binned event train is defined according to

$$E_i(t_b) = \begin{cases} 1 & \text{if} \sum_{t \in t_b} E_i(t) > 0 \\ 0 & \text{otherwise} \end{cases} \tag{5.8}$$

We emphasise that this binning procedure is different to the binning procedure used for the avalanche statistics of a single event train (Section 3.3.4), to ensure consistency with the procedure used in [1].

After binning, the time-bins with no events (time-bin 5 in Figure 5.4 (b)) are removed to eliminate bias in the analysis [1]. Note that the analysis of the chain model above was not binned and did not have time-bins removed as per [1].

5.2.2 Data Randomisation

A key conclusion in [1] is that neural complexity in biological systems is heavily dependent on the total number of events at each neuron (electrode), and on the total number of events in each time-bin. This conclusion was reached through analysis of the effect of different randomisation methods on the data.

These randomisation methods were also implemented here using the MATLAB NCC toolbox [105]. Each randomisation method is applied after the data was binned and is briefly summarised below. Table 5.1 shows the effect of each randomisation method. Figure 5.5 shows schematic illustrations for each of the randomisation methods.

Jitter: Each event in each binned event train ($E_i(t_b)$) is repositioned to a new time-bin according to a Gaussian distribution centred on the original event, and with a standard deviation of 1, 10, or 100 time-bins. No two events were moved to the same time-bin, hence the total number of events is conserved. The total events in each time-bin are changed with the jitter method. Note that the jitter method does not move events between event trains.

Wrap: Each event train is 'cut' at a random time-bin and the two halves are swapped. The total events in each time-bin are severely changed by this randomisation. The total number of events is conserved in each event train. Note that each event train is cut at a different random time-bin.

Poisson: All events for each event train are randomly placed into empty event trains. This process destroys all correlations between event trains, and severely changes the total events in each time-bin. The total number of events in each event train is conserved. Note that the same Poisson randomisation was previously used in Section 4.1.4.

Swap: Events are swapped between event trains such that an event at time t_1 in event train A was swapped with an event at t_2 in event train B. This process only occurs if event train A does not already have an event at t_2, and event train B does not already have an event at t_1. The total events in each event train and in each time-bin are unchanged by the swap method. However, relationships between event trains are changed. Note that the NCC toolbox attempts to swap every event at least once, however some events cannot be swapped. For example, an event detected at all electrodes cannot be swapped without changing the total number of events in at least one event train (see Figure 5.5).

Shuffle: All events in a time-bin are shuffled randomly between the event trains. The total events in each time-bin is conserved, however the total number of events in each event train, and relationships between event trains are changed. Note that the overall number of events was not changed by the shuffle randomisation.

5.2.3 Subsampling Correction

The complexity of random data in Figure 5.3 (g) is not exactly zero, which contradicts the theory that random data has zero neural complexity [106]. This apparent contradiction is due to subsampling of the possible states of the system at any given time-bin [105]. For example, plenty of data is available in a measurement to accurately estimate the entropy of one event train ($H(E_i(t))$), whereas comparatively little data is available to estimate the entropy for large subsets of event trains ($H(X_j^k)$, large k). Therefore, subsampling can lead

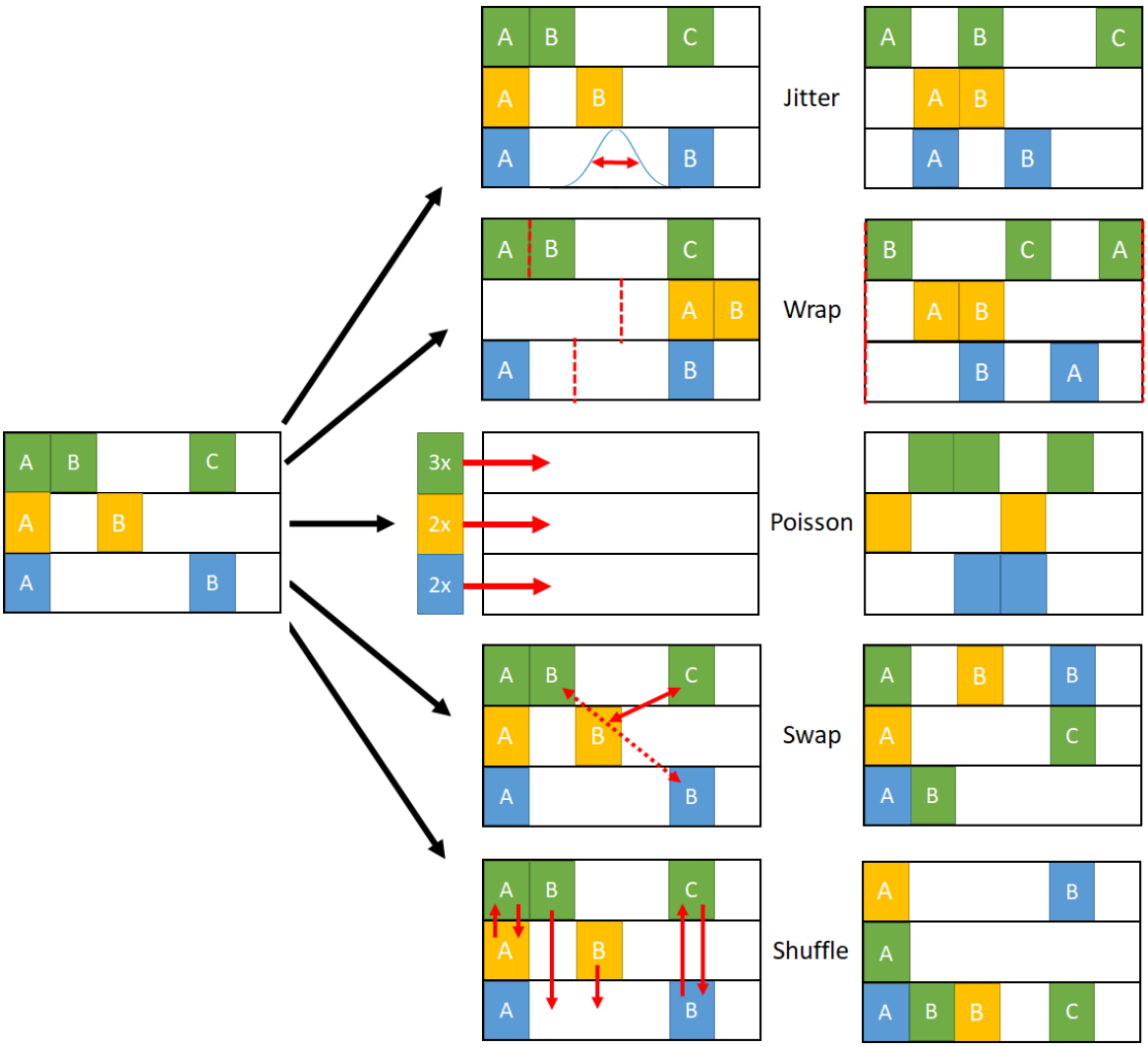

Figure 5.5: *Schematic of the five randomisation methods used for the neural complexity analysis. Each coloured square indicates an event was detected at that time-bin. The different colours correspond to the event train for which the event originally occurred in the real data (left-hand column). The letters indicate the original time order of the events for each event train. The red arrows in the middle column signal the change that occurs for each method. The right-hand column shows the result of randomisation. Jitter: moves events in time by a normal distribution of the current position. Wrap: cut each event train at a random time-bin (dashed red lines) and swap the halves. Poisson: count the events per event train, then randomly place these into empty event trains. Swap: swap pairs of events between event trains (red arrows) so that the event count is conserved for each event train. Note that the solid red arrow is swapped first and then the dashed red arrow. Events are not swapped if it is impossible to move them without changing the event count in each electrode. Shuffle: randomly move events within a time-bin to any event train.*

to poor estimates of the entropy, and hence poor estimates of the complexity. The NCC toolbox implements a subsampling correction, in which the integration is calculated for the real data (I_{real}) and for Poisson randomised data ($I_{Poisson}$). The integration used to calculate complexity is then given by

Randomisation Method	Total Events in each Event Train	Total Events in each Time-Bin
Jitter	Conserved	Altered
Wrap	Conserved	Altered
Poisson	Conserved	Altered
Swap	Conserved	Conserved
Shuffle	Altered	Conserved

Table 5.1: *Summary of the data features changed by each randomisation method.*

$$I = I_{real} - I_{Poisson} \tag{5.9}$$

The subsampling correction in Equation 5.9 was applied to find the integration throughout Section 5.3. Note that the correction was also applied to data after randomisation with the methods described above.

Therefore, the full process for the complexity analysis is:

1. Bin the event trains by the average IEI of the overall event train.
2. Remove all time-bins with no events.
3. Randomise the data if calculating the complexity of random data (ignore this step for calculating neural complexity of real data).
4. Calculate the integration for the binned event trains.
5. Poisson randomise the event trains.
6. Calculate the integration for the randomised event trains.
7. Calculate the complexity from the corrected integration: $I = I_{real} - I_{Poisson}$.

The next section presents the analysis of experimental and simulation PASN data with the above procedure.

5.3 Neural Complexity Analysis

5.3.1 Complexity of Experiments

Figure 5.6 (a) and (b) show the linear approximation to the integration (red line) and the average integration for all subsets of k event trains (blue curve), for typical measurements of Device I and Device II respectively. The integration increases non-linearly for both devices, which indicates the switching activity of PASNs is complex. The complexity of Device I (0.134 bits/electrode) is much larger than the complexity of Device II (0.038 bits/electrode).

Figure 5.6 (c) and (d) show segments of the event raster analysed in Figure 5.6 (a) and (b) respectively. The event raster for Device I appears more complex than Device II. This

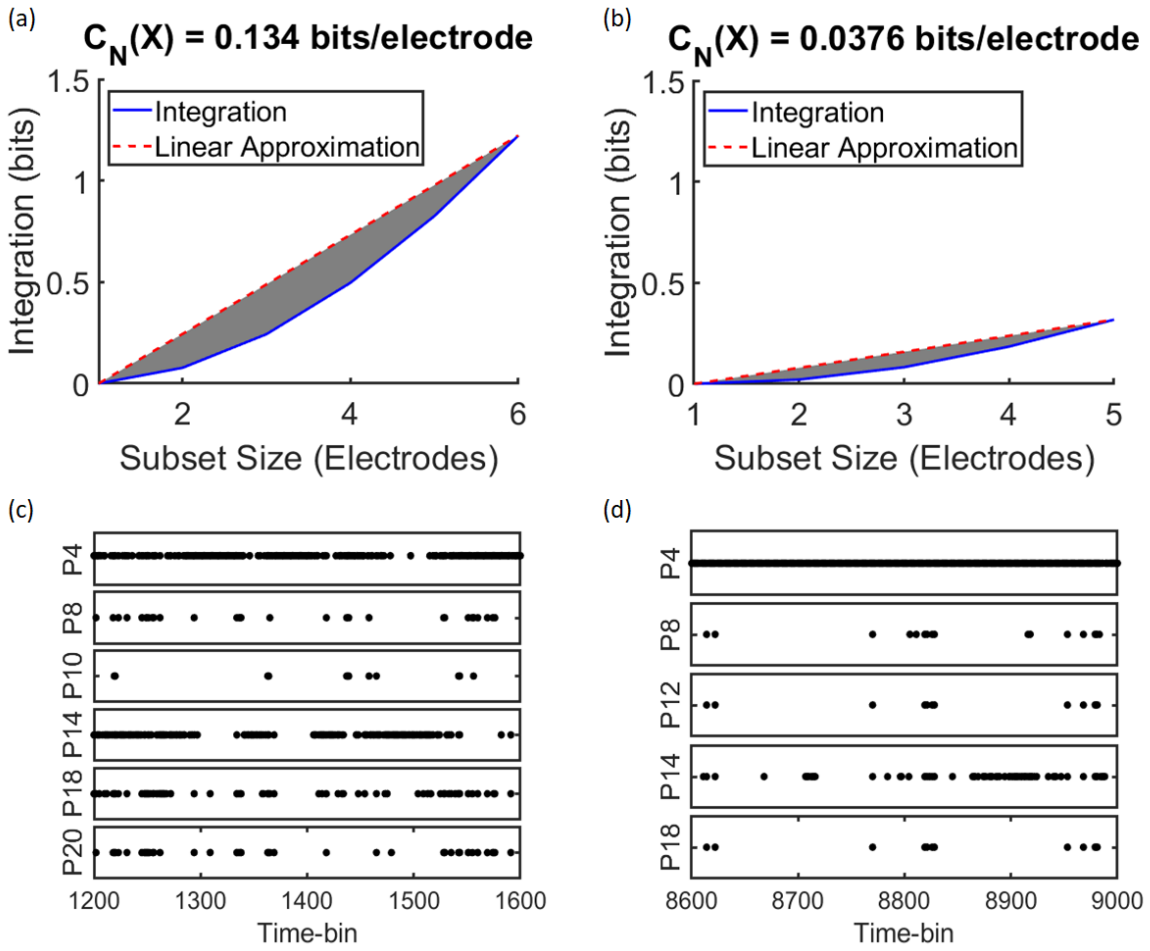

Figure 5.6: *(a,b) The linear approximation to the integration (red line), and the average integration for each subset of k event trains (blue curve) for a typical 10-minute measurement of Device I ([DI, A, 10V, 1]) and Device II ([DII, E, 8V, 1]) respectively. (c,d) Representative segments of the event rasters analysed in (a) and (b) respectively.*

data is consistent with the qualitative features of Device I data and Device II data observed in Section 4.1.3. Moreover, the integration and resulting complexity reflect the qualitative complexity of each event raster.

Time Dependence and Variation

Figure 5.7 (a) shows the complexity of 15 consecutive 10-minute measurements of Device I. The average complexity is 0.108 bits/electrode, and most of the segments have similar or larger complexity to this average. However, two time-segments (30-40 minutes, and 80-90 minutes) have much lower complexity (0.0597 bits/electrode and 0.0233 bits/electrode respectively) than the other segments. Therefore, the complexity of 10-minute segments can vary greatly.

Table 5.2 shows the number of observed events at each electrode of select 10-minute segments from Figure 5.7 (a). The segments with the lowest complexity (30-40 minutes, 80-90 minutes) have more total events than other segments, with most of these observed events at one electrode (electrode P4 and electrode P20 in the 30-40 and 80-90 minute

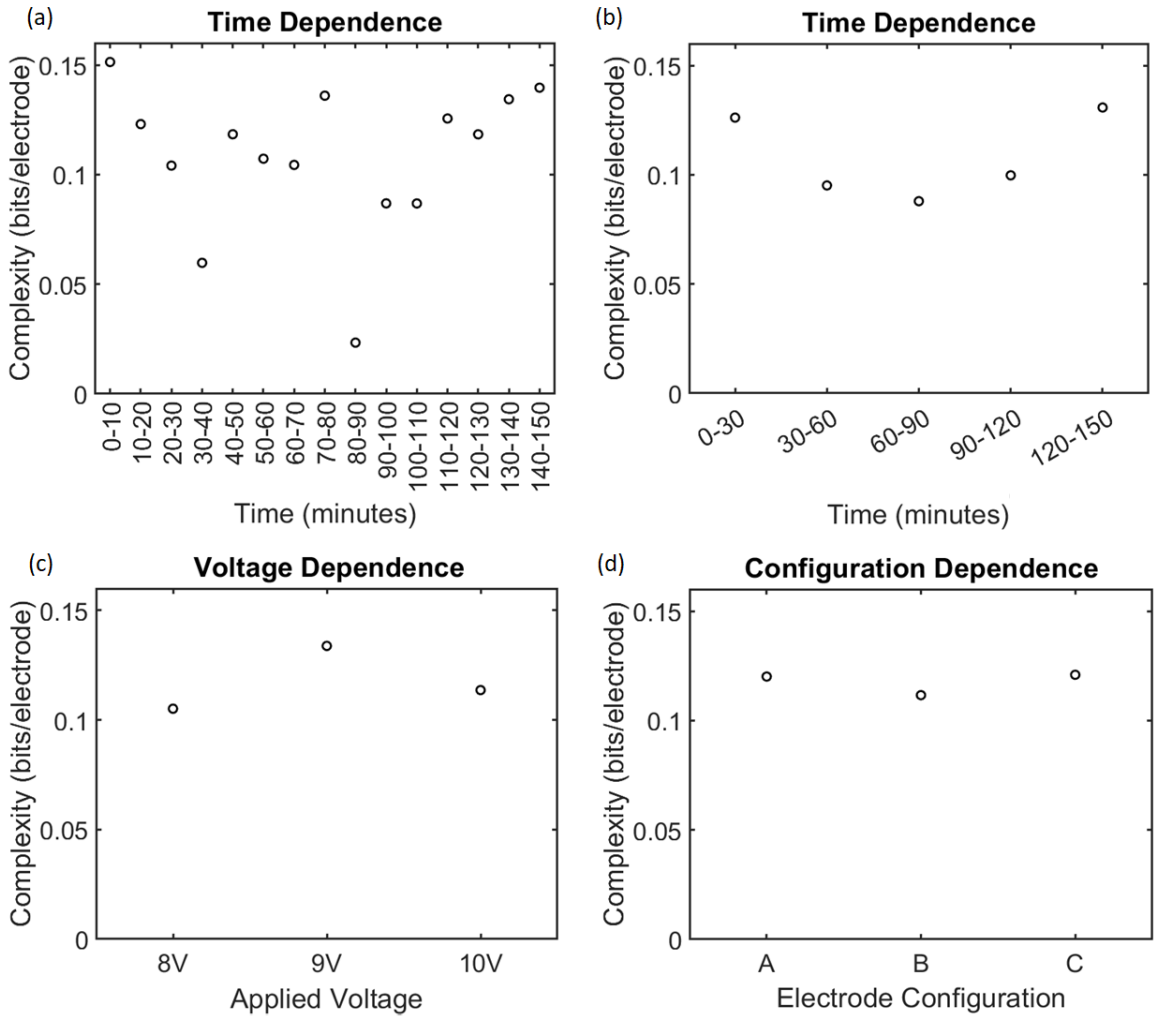

Figure 5.7: *(a) Neural complexity of 15 consecutive 10-minute measurements of Device I ([DI, 10V, A, 1]). The average complexity is 0.108 bits/electrode, and the minimum is 0.0233 bits/electrode. (b) Average complexity of three consecutive 10-minute measurements from (a). The complexity has a range of ~0.5 bits/electrode. (c) Each data-point is the average complexity of three 10-minute measurements at the same voltage. 8V data-point: [DI, A, 8V, 1], [DI, B, 8V, B], [DI, 8V, C, 1]. 9V data-point: [DI, A, 9V, 1], [DI, B, 9V, 1], [DI, C, 9V, 1]. 10V data-point: [DI, A, 10V, 1], [DI, B, 10V, 1], [DI, C, 10V, 1]. (d) Each data-point is the average complexity of three 10-minute measurements with the same electrode configuration. Configuration A data-point: [DI, A, 8V, 1], [DI, A, 9V, 1], [DI, A, 10V, 1]. Configuration B data-point: [DI, B, 8V, 1], [DI, B, 9V, 1], [DI, B, 10V, 1]. Configuration C data-point: [DI, C, 8V, 1], [DI, C, 9V, 1], [DI, C, 10V, 1].*

segments respectively). In contrast, the segments with relatively high complexity (0-10 minutes, 140-150 minutes) do not have most of the event detections at one electrode. Hence, the complexity is relatively low when activity at one electrode is dominant, and complexity is higher when comparable numbers of events are observed at all electrodes (provided that multiple combined states (x) are still observed).

Figure 5.7 (b) shows the average complexity for every three consecutive 10-minute segments in Figure 5.7 (a). The variation in complexity is significantly less for the averaged data segments, as the largest complexity value (0.131 bits/electrode) is within 0.05 bits/electrode

of the smallest complexity value (0.0879 bits/electrode). Hence an estimate of significant differences in the complexity for the average of three 10-minute measurements is ~0.05 bits/electrode.

Electrode	0-10 minutes	20-30 minutes	30-40 minutes	80-90 minutes	110-120 minutes	140-150 minutes
P4	3358	18760	79081	12266	5670	16962
P8	100	35	3067	18	1221	12857
P10	2124	571	1275	322	437	706
P14	1035	3161	932	388	927	4243
P18	3092	7689	4163	3271	7024	7671
P20	4061	2524	4911	77434	7396	5316
C_N	**0.151**	**0.104**	**0.0597**	**0.0233**	**0.126**	**0.140**

Table 5.2: *Events observed at each electrode in select 10-minute segments corresponding to Figure 5.7 (a). The bottom row shows the complexity for each of the segments in bold.*

Voltage Dependence

Figure 5.7 (c) shows the average complexity of three 10-minute measurements with the same applied voltage at each data-point. The complexity at each voltage is within 0.03 bits/electrode of the complexity at the other voltages, which is less than the variation observed over time for the average of three 10-minute measurements. Therefore, the complexity does not significantly change with applied voltage.

Configuration Dependence

Figure 5.7 (d) shows the average complexity of three 10-minute measurements in each of three different electrodes configurations. The complexity of the events observed with each electrode configuration are all within 0.01 bits/electrode. Hence, the complexity is not significantly affected by the electrode configuration.

Threshold Dependence

As discussed in Section 3.1.3, the impact of the threshold choice on the analysis must be explored. Figure 5.8 (a) and (b) show the integration curves for a typical 10-minute measurement of Device I with an event threshold of $|\Delta I|_{thresh}$ and $0.67 \times |\Delta I|_{thresh}$ respectively. The integration is very similar for data with each threshold. Furthermore the complexity of the data with a threshold of $|\Delta I_{thresh}|$ (0.134 bits/electrode) is similar to the complexity with a threshold of $0.67 \times |\Delta I_{thresh}|$ (0.120 bits/electrode). Therefore, the analysis does not significantly change with different event thresholds across a reasonable range.

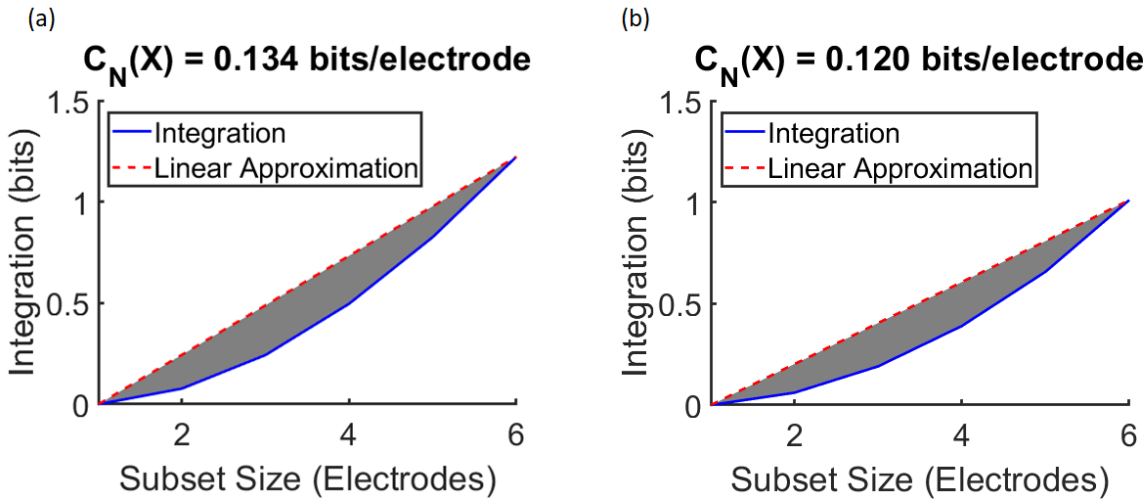

Figure 5.8: *(a, b) Linear approximation (red line) and average integration for all subsets of k electrodes (blue) for 10-minutes of Device I data ([DI, A, 10V, 1]). (a) Threshold for event detection is ΔI_{thresh} (Equation 3.2). (b) Threshold for event detection is 67% of ΔI_{thresh}. The complexity does not significantly change for analysis within the reasonable range of thresholds.*

5.3.2 Randomised Complexity

Figure 5.9 (a) and (b) show the complexity for two different 10-minute measurements of Device I compared with the complexity after the randomisations listed in Section 5.2.2. Note that Figure 5.9 (a) shows data measured at 8V, whereas Figure 5.9 (b) shows data measured at 10V. As discussed above, the complexity is very similar between datasets measured at 8V and 10V.

The wrap and Poisson randomisations significantly reduced the complexity of the PASN data. The complexity also decreased when the jitter method was applied. The larger the standard deviation (in time-bins) of the jitter, the greater the reduction in complexity.

The PASN complexity decreased slightly under the swap method in both Figure 5.9 (a) and (b). Additionally, the shuffle method led to a higher complexity than the swap method for the PASN data. Interestingly, the shuffle method occasionally produced data with larger complexity than the real data, as shown in Figure 5.9 (a).

Table 5.3 shows the total events observed at each electrode of the real and shuffled data in Figure 5.9 (a) and (b). Note that the events are observed at the electrodes in the real data, and the shuffle method simply changes the electrode that 'observed' each event. The real data shows an order of magnitude difference in the number of observed events between different electrodes for both datasets. In contrast, the shuffle method causes very similar numbers of events to be 'observed' at all electrodes, which has a large impact on the entropy for each electrode.

The entropy of the individual electrodes (event trains, $H(E_i)$) depends on the number of events observed at that electrode (Section 5.1.2). Table 5.4 shows the entropy of the different electrodes in the real and shuffled data corresponding to Figure 5.9 (a) and (b). The entropy of the shuffled data is larger than the real data for both measurements of Device I. Furthermore, the entropy increases more for the data in Figure 5.9 (a) than Figure 5.9

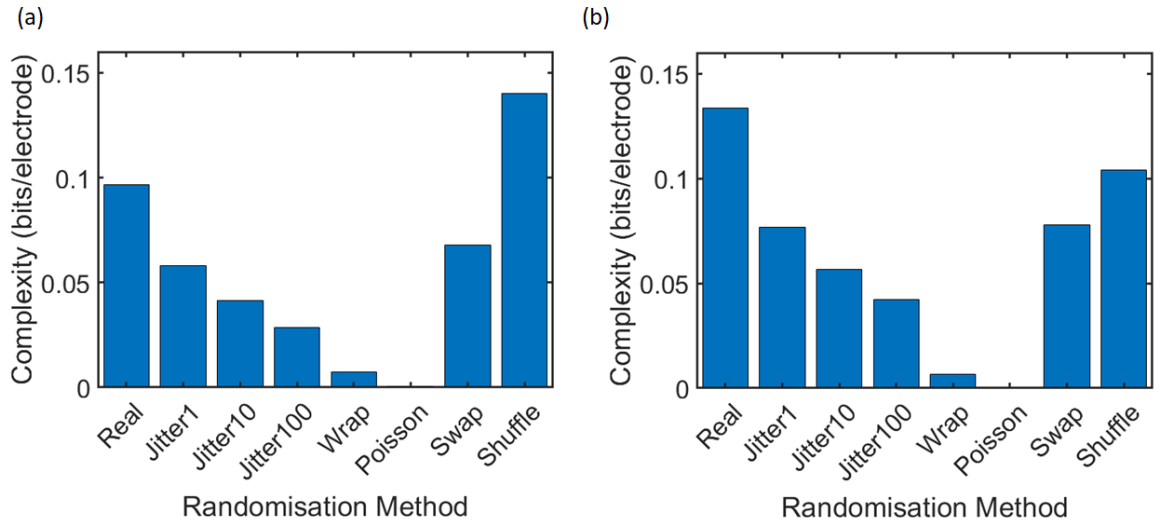

Figure 5.9: *(a,b) Complexity of 10-minutes of Device I data under each of the randomisation methods described in Section 5.2.2. (a) [DI, B, 8V, 1]. (b) [DI, A, 10V, 1]. The complexity of the shuffled data is larger than the real complexity in (a), but smaller than the real complexity in (b).*

(b).

5.3.3 Complexity of Simulations

Figure 5.10 (a) and (b) show the integration for the ~10% event density (without thresholds) simulation with an 80% and 90% global event threshold respectively (simulation details provided in Section 4.2.3). The complexity is non-zero for the simulation which further supports the hypothesis that PASNs exhibit complex switching activity. Note that, the different global thresholds do not significantly change the complexity or integration.

Figure 5.10 (c) and (d) compare the complexity of the simulation results with that calculated for the randomisation methods used in Figure 5.9 (a) and (b). Each randomisation reduces the complexity in a qualitatively similar manner to the experimental results shown in Figure 5.9 (b).

5.4 Comparison of PASN and Biological Complexity

5.4.1 Biological Data

The complexity of spiking neurons in dissociated rat hippocampal cultures were analysed in [1]. Note that the each row of the event raster for the biological data represents the spike train (analogous to event train) of a neuron identified in the recording of interest. Over 100 neurons were identified in a typical recording. See [1] for complete details.

Figure 5.11 (a) shows the integration for a recording of neurons in a culture [1]. The average integration (blue line) is non-linear which results in a non-zero complexity. Figure 5.9 (b) shows the complexity results obtained in [1] under each randomisation method described

	Figure 5.9 (a)		Figure 5.9 (b)	
Electrode	Real	Shuffled	Real	Shuffled
1	7138	2004	5158	2844
2	239	1967	421	2846
3	124	2020	453	2936
4	1863	2024	4107	2879
5	401	2053	6300	2883
6	2313	2010	781	2832

Table 5.3: *Total events observed at each electrode in the real and shuffled data for two different 10-minutes measurements of Device I (corresponding to Figure 5.9 (a) and (b)). Note that electrode 1,2,3,... correspond to the numerical order of the electrode identifiers. For example the set of electrodes P2, P4, P8 would be electrodes 1, 2, 3 respectively here.*

	Figure 5.9 (a)		Figure 5.9 (b)	
Electrode	Real	Shuffled	Real	Shuffled
1	0.6936	0.7753	0.9980	0.8284
2	0.1804	0.7678	0.2361	0.8287
3	0.1071	0.7785	0.2495	0.8408
4	0.7460	0.7793	0.9559	0.8332
5	0.2679	0.7850	0.9822	0.8337
6	0.8322	0.7765	0.3722	0.8267
Totals	2.827	4.662	3.794	4.991

Table 5.4: *Entropy of each electrode (event train) in the real and shuffled data for two different 10-minutes measurements of Device I (corresponding to Figure 5.9 (a) and (b)). The entropy is larger in the shuffled data than the real data.*

in Section 5.2.2. The complexity of the neuron data decreased under all randomisation methods except the swap method. The randomisations which strongly destroyed correlations within the data (100 bin jitter, wrap, and Poisson) reduced the complexity the most. The swap method did not significantly change the complexity, despite changing the combined states [1].

5.4.2 Comparison of PASN and Biological Complexity

As shown in Figure 5.9 (a) and (b), the complexity of PASN data decreased with the jitter, wrap, and Poisson methods. These decreases in complexity under randomisation are similar to the results obtained for biological data under the same randomisations [1]. Hence, the complexity of PASNs is similar to that of neuron spiking data in rat hippocampal cultures, which is a strong indicator for brain-like complexity in PASNs.

Figure 5.9 (a) and (b) also show a slight decrease in PASN complexity under the swap randomisation. As discussed in Section 5.1, the complexity depends on the entropy of the individual electrodes (individual event trains after binning) and the joint entropy of subsets of the event raster (X_j^k). The swap method does not change the entropy of the individual

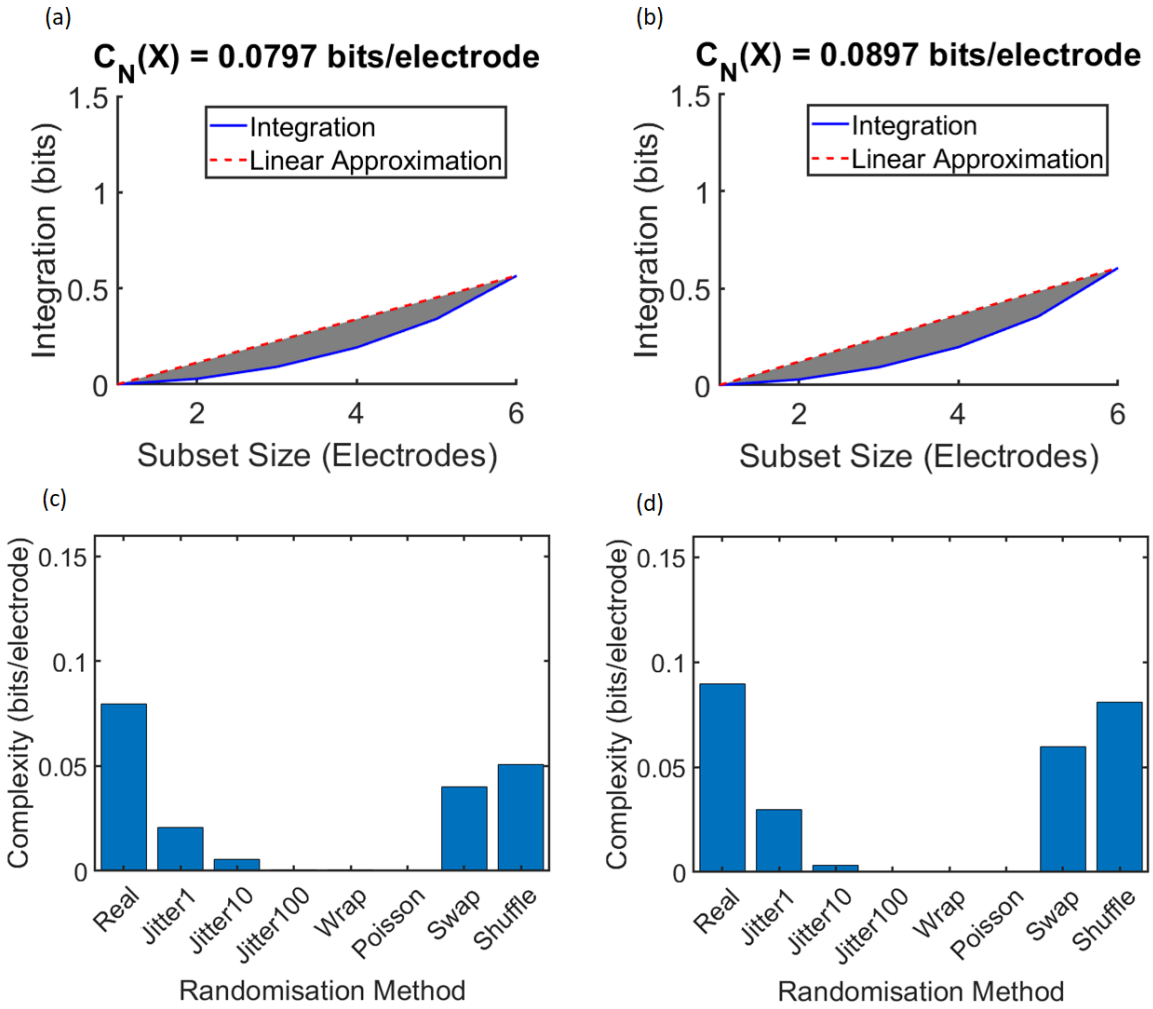

Figure 5.10: *Complexity analysis of 600,000 time-steps (before binning) of the simulation with an event density of ~10% (Section 4.2). (a,b) The linear approximation to the integration for each subset size (red line), and the average integration for each subset size (blue curve) when an 80% (a) and 90% (b) global threshold are applied to event detection. (c,d) Complexity of the simulation with each randomisation method described in Section 5.2.2 applied. (c) An 80% global threshold, and (d) 90% global threshold applied for event detection. Similar results are observed as for the experimental data in Section 5.3.2.*

electrodes, because the total number of events at each electrode does not change. However, the joint entropy increases slightly in the swapped data, because the frequently observed combined states, x, will be observed less often, while the infrequently observed combined states will be observed more often. Hence, $p(x)$ are distributed more uniformly under the swap randomisation, which causes the joint entropies to slightly increase (Equation 5.1), and hence the complexity slightly decreases. Note that the swap method preserves the total events in each time-bin, and so the $p(x)$ are only slightly changed, which explains why the swap method only slightly changes the complexity compared to other randomisation methods.

The decrease in complexity in PASN data under swap randomisation was not observed in the neuron data shown in Figure 5.11 (b). It is not clear what causes this difference in the effect of the swap randomisation for the PASN and neuron data. However, the discrepancy

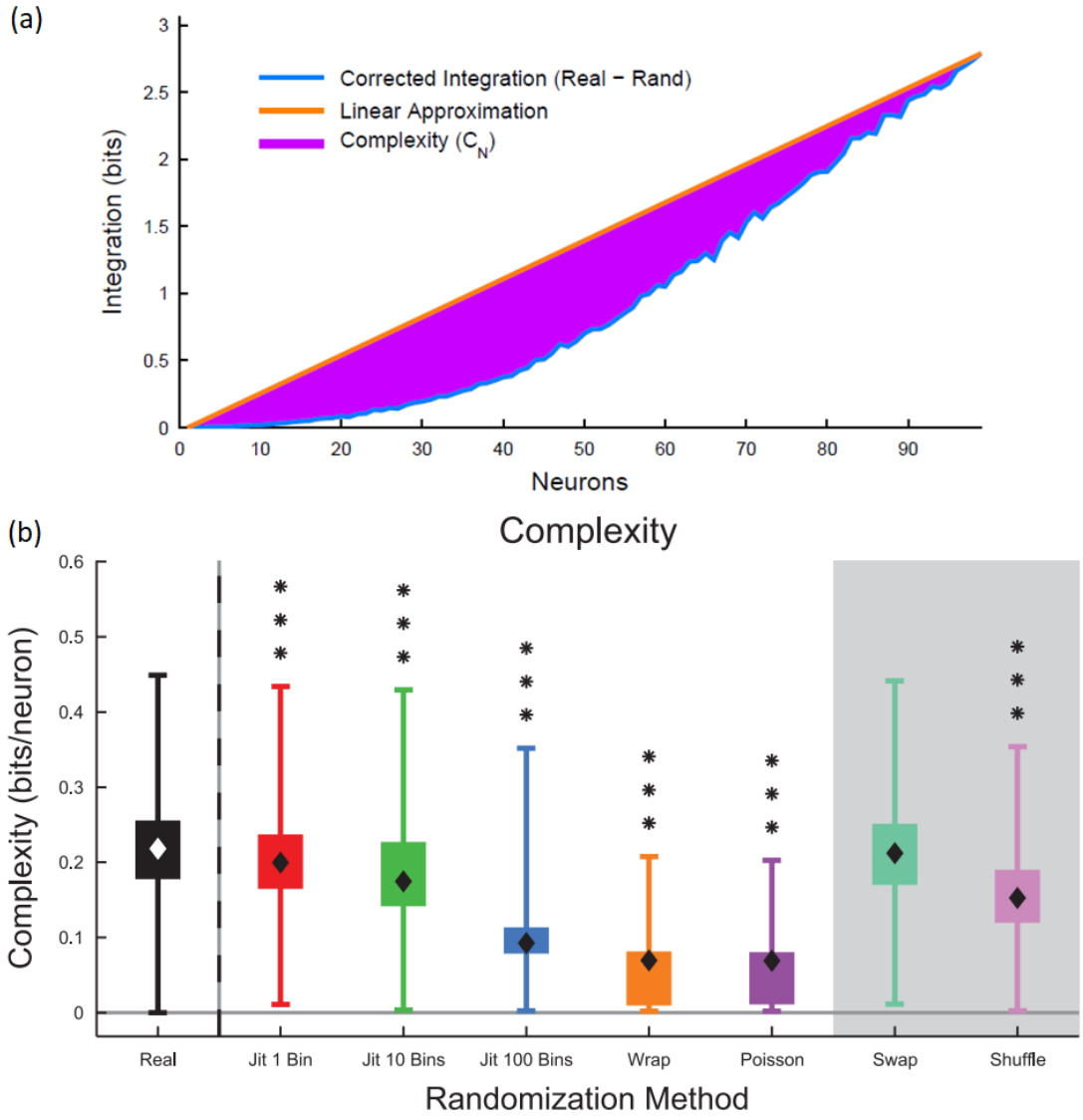

Figure 5.11: *(a) Average integration (blue line) and the linear approximation (red line) to the integration at all subsets of k neurons. (b) Complexity of neurons in rat hippocampal cultures under each randomisation method described in Section 5.2.2. The grey region highlights the swap and shuffle methods which preserve the total events per time-bin (Section 5.2.2). The data is presented as box plots with each line from bottom to top corresponding to the minimum, 25th percentile, median (shown as a diamond), 75th percentile, and maximum. The stars represent outliers. (a,b) Adapted from [1] under CCL: CC BY (http://creativecommons.org/licenses/by/4.0/).*

is likely related to the number of combined states in each type of data. The neuron data had ~100 neurons in each measurement, which means a total of $2^{\sim 100}$ possible combined states. In contrast, the PASNs had only 6 output electrodes (in Figure 5.9 (a) and (b)) and a total of 64 possible combined states.

Interestingly, the shuffle randomisation slightly reduced the complexity in some PASN datasets (Figure 5.9 (b)) and increased the complexity in other datasets (Figure 5.9 (a)). This result can be explained by considering the effect of the shuffle randomisation on the entropy. The shuffle method increases the joint entropies of each subset of X, because some

of the correlations between events are destroyed. This increase in joint entropy leads to a decrease in the complexity. However, the individual entropies tend to increase after the shuffle method, which increases the integration (Equation 5.4) and hence the complexity increases. It is the balance of the increase in complexity due to individual entropies and the decrease in complexity due to joint entropies that determine the complexity of the shuffled data. For the data in Figure 5.9 (a), the individual entropies increase significantly after shuffle randomisation and the complexity increases. For the data in Figure 5.9 (b), the individual entropies increase, but not by enough for the shuffled complexity to be larger than the real complexity.

5.5 Summary of Neural Complexity

The switching activity of MC PASNs has non-zero complexity with the neural complexity metric. The complexity does not significantly change with applied voltage, electrode configuration, or between reasonable threshold choices.

Switching activity of PASNs show comparable complexity to spiking activity in neurons of rat hippocampal cultures [1]. Moreover, the randomisation methods had a similar affect on the complexity of PASN data and neuron data, which indicates the complexity of PASNs is brain-like. Note that the PASNs had very few electrodes compared to the number of neurons in [1], which likely accounts for the slight differences in the complexity after the swap and shuffle randomisations. Moreover, the complexity of the PASN simulation is also qualitatively similar to the experimental complexity both with and without randomisation. Overall, these results indicate that switching activity of PASNs exhibits brain-like complexity.

Chapter 6

Conclusion

Percolating atomic switch networks are promising candidates for neuromorphic computing applications, because they exhibit many brain-like properties such as criticality, hierarchical structures, and long-range temporal correlations. Another important property for neuromorphic computing, complexity, has not been previously explored in detail. It has been argued that brain-like complexity is essential for truly brain-like computation. The recent development of devices with multiple electrodes connected to a PASN has enabled a first study into the complexity of switching activity in PASNs.

The first goal of this research was to establish whether the PASN switching dynamics are altered by the new multiple-electrode device geometry. The voltage dependence of switching activity, distributions of inter-event-intervals, and avalanche statistics are all key statistics of PASNs that were quantitatively similar regardless of device geometry. Hence, the dynamics of multi-electrode devices are similar to those of two-electrode devices, and all research into multi-electrode devices.

The primary objective of this thesis was to qualitatively and quantitatively explore the complexity of switching activity in PASNs, and to compare these results to the complexity of the brain. The qualitative behaviour of PASNs (Chapter 4) is neither random nor ordered, which indicates complexity on a qualitative level. Moreover, the qualitative complexity is linked to the underlying fractal structure of PASNs. The quantitative complexity analysis of PASNs (Chapter 5) demonstrated a non-zero complexity for PASN switching activity. Furthermore, the complexity of PASNs was very similar to the complexity of a network of neurons in rat hippocampal cultures. The effect of randomisation on the complexity was similar between PASNs and the neural system, except for the swap and shuffle randomisations. It is likely the small number of electrodes for the PASNs compared with the large number of neurons in the biological system is responsible for this discrepancy. Overall, the qualitative and quantitative analysis strongly suggest that PASNs exhibit brain-like complexity.

6.1 Future Work

This section briefly discusses ideas for future research building upon the complexity results in this thesis.

- This thesis focussed on the analysis of two multi-electrode devices. In future, the

neural complexity of more devices produced with different deposition conditions could be analysed. The effect of the different deposition conditions on complexity could inform decisions regarding which devices may be best for neuromorphic computing applications.

- The complexity analysis focussed on non-spiking events by subsampling the data. It would be interesting to complete a detailed analysis of how complexity changes for different segments of spiking data.

- It would be interesting to fabricate and analyse devices with a greater number of electrodes to investigate whether the complexity is significantly changed. Additionally, the effect of the swap and shuffle randomisation would be interesting to investigate with more electrodes.

- The neural complexity metric has been researched for over two decades, however no metric of complexity is definitively agreed upon in the literature. Therefore, it is important to investigate whether different complexity metrics, such as Lempel-Ziv complexity [111] or Granger causality [112], can be applied to PASNs in order to demonstrate whether they exhibit brain-like complexity.

Bibliography

[1] N. M. Timme, N. J. Marshall, N. Bennett, M. Ripp, E. Lautzenhiser, and J. M. Beggs, "Criticality maximizes complexity in neural tissue," *Frontiers in physiology*, vol. 7, p. 425, 2016.

[2] G. E. Moore, "Progress in digital integrated electronics," in *Electron devices meeting*, vol. 21, pp. 11–13, 1975.

[3] T. Cross, "After moore's law," *The Economist.(March 2016). http://www. economist. com/technology-quarterly/2016-03-12/after-moores-law*, 2016.

[4] G. E. Moore, "Cramming more components onto integrated circuits," *Proceedings of the IEEE*, vol. 86, no. 1, pp. 82–85, 1998.

[5] N. Bloom, C. I. Jones, J. Van Reenen, and M. Webb, "Are ideas getting harder to find?," *American Economic Review*, vol. 110, no. 4, pp. 1104–44, 2020.

[6] S. B. Desai, S. R. Madhvapathy, A. B. Sachid, J. P. Llinas, Q. Wang, G. H. Ahn, G. Pitner, M. J. Kim, J. Bokor, C. Hu, *et al.*, "Mos2 transistors with 1-nanometer gate lengths," *Science*, vol. 354, no. 6308, pp. 99–102, 2016.

[7] R. C. Fong, W. J. Scheirer, and D. D. Cox, "Using human brain activity to guide machine learning," *Scientific reports*, vol. 8, no. 1, pp. 1–10, 2018.

[8] C. M. Signorelli, "Can computers become conscious and overcome humans?," *Frontiers in Robotics and AI*, vol. 5, p. 121, 2018.

[9] D. Silver, A. Huang, C. J. Maddison, A. Guez, L. Sifre, G. Van Den Driessche, J. Schrittwieser, I. Antonoglou, V. Panneershelvam, M. Lanctot, *et al.*, "Mastering the game of go with deep neural networks and tree search," *nature*, vol. 529, no. 7587, pp. 484–489, 2016.

[10] M. Le Page, "Knowledge means power," *New Scientist*, vol. 240, no. 3199, pp. 22 – 23, 2018.

[11] C. Mead, "Neuromorphic electronic systems," *Proceedings of the IEEE*, vol. 78, no. 10, pp. 1629–1636, 1990.

[12] N. Srinivasa, N. D. Stepp, and J. Cruz-Albrecht, "Criticality as a set-point for adaptive behavior in neuromorphic hardware," *Frontiers in neuroscience*, vol. 9, p. 449, 2015.

[13] A. Sattar, S. Fostner, and S. A. Brown, "Quantized conductance and switching in percolating nanoparticle films," *Physical review letters*, vol. 111, no. 13, p. 136808, 2013.

[14] S. K. Bose, J. B. Mallinson, R. M. Gazoni, and S. A. Brown, "Stable self-assembled atomic-switch networks for neuromorphic applications," *IEEE Transactions on Electron Devices*, vol. 64, no. 12, pp. 5194–5201, 2017.

[15] S. K. Bose, S. Shirai, J. B. Mallinson, and S. A. Brown, "Synaptic dynamics in complex self-assembled nanoparticle networks," *Faraday discussions*, vol. 213, pp. 471–485, 2019.

[16] J. B. Mallinson, S. Shirai, S. K. Acharya, S. K. Bose, E. Galli, and S. A. Brown, "Avalanches and criticality in self-organized nanoscale networks," *Science advances*, vol. 5, no. 11, p. eaaw8438, 2019.

[17] S. Shirai, S. K. Acharya, S. K. Bose, J. B. Mallinson, E. Galli, M. D. Pike, M. D. Arnold, and S. A. Brown, "Long-range temporal correlations in scale-free neuromorphic networks," *Network Neuroscience*, vol. 4, no. 2, pp. 432–447, 2020.

[18] M. D. Pike, S. K. Bose, J. B. Mallinson, S. K. Acharya, S. Shirai, E. Galli, S. J. Weddell, P. J. Bones, M. D. Arnold, and S. A. Brown, "Atomic scale dynamics drive brain-like avalanches in percolating nanostructured networks," *Nano letters*, vol. 20, no. 5, pp. 3935–3942, 2020.

[19] C. D. Schuman, T. E. Potok, R. M. Patton, J. D. Birdwell, M. E. Dean, G. S. Rose, and J. S. Plank, "A survey of neuromorphic computing and neural networks in hardware," *arXiv preprint arXiv:1705.06963*, 2017.

[20] J. Von Neumann, "First draft of a report on the edvac," *IEEE Annals of the History of Computing*, vol. 15, no. 4, pp. 27–75, 1993.

[21] J. Backus, "Can programming be liberated from the von neumann style? a functional style and its algebra of programs," *Communications of the ACM*, vol. 21, no. 8, pp. 613–641, 1978.

[22] H. G. Cragon, *Computer architecture and implementation*. Cambridge University Press, 2000.

[23] N. Talati, R. Ben-Hur, N. Wald, A. Haj-Ali, J. Reuben, and S. Kvatinsky, "mmpu—a real processing-in-memory architecture to combat the von neumann bottleneck," in *Applications of emerging memory technology*, pp. 191–213, Springer, 2020.

[24] R. A. Nawrocki, R. M. Voyles, and S. E. Shaheen, "A mini review of neuromorphic architectures and implementations," *IEEE Transactions on Electron Devices*, vol. 63, no. 10, pp. 3819–3829, 2016.

[25] Z. Kuncic and T. Nakayama, "Neuromorphic nanowire networks: principles, progress and future prospects for neuro-inspired information processing," *Advances in Physics: X*, vol. 6, no. 1, p. 1894234, 2021.

[26] D. Marković, A. Mizrahi, D. Querlioz, and J. Grollier, "Physics for neuromorphic computing," *Nature Reviews Physics*, vol. 2, no. 9, pp. 499–510, 2020.

[27] M. I. Jordan and T. M. Mitchell, "Machine learning: Trends, perspectives, and prospects," *Science*, vol. 349, no. 6245, pp. 255–260, 2015.

[28] K. Boahen, "Neuromorphic microchips," *Scientific American*, vol. 292, no. 5, pp. 56–63, 2005.

[29] J. Ma and J. Tang, "A review for dynamics in neuron and neuronal network," *Nonlinear Dynamics*, vol. 89, no. 3, pp. 1569–1578, 2017.

[30] J. M. Murre and D. P. Sturdy, "The connectivity of the brain: multi-level quantitative analysis," *Biological cybernetics*, vol. 73, no. 6, pp. 529–545, 1995.

[31] H. Lodish, A. Berk, C. A. Kaiser, C. Kaiser, M. Krieger, M. P. Scott, A. Bretscher, H. Ploegh, P. Matsudaira, *et al.*, *Molecular cell biology*. Macmillan, 2008.

[32] T. V. Bliss and T. Lømo, "Long-lasting potentiation of synaptic transmission in the dentate area of the anaesthetized rabbit following stimulation of the perforant path," *The Journal of physiology*, vol. 232, no. 2, pp. 331–356, 1973.

[33] R. A. Nicoll, "A brief history of long-term potentiation," *Neuron*, vol. 93, no. 2, pp. 281–290, 2017.

[34] D. R. Chialvo, "Emergent complex neural dynamics," *Nature physics*, vol. 6, no. 10, pp. 744–750, 2010.

[35] E. Bullmore and O. Sporns, "Complex brain networks: graph theoretical analysis of structural and functional systems," *Nature reviews neuroscience*, vol. 10, no. 3, pp. 186–198, 2009.

[36] H.-J. Park and K. Friston, "Structural and functional brain networks: from connections to cognition," *Science*, vol. 342, no. 6158, 2013.

[37] E. Bullmore and O. Sporns, "The economy of brain network organization," *Nature Reviews Neuroscience*, vol. 13, no. 5, pp. 336–349, 2012.

[38] N. Gupta, "Artificial neural network," *Network and Complex Systems*, vol. 3, no. 1, pp. 24–28, 2013.

[39] M. H. Hassoun *et al.*, *Fundamentals of artificial neural networks*. MIT press, 1995.

[40] S. Agatonovic-Kustrin and R. Beresford, "Basic concepts of artificial neural network (ann) modeling and its application in pharmaceutical research," *Journal of pharmaceutical and biomedical analysis*, vol. 22, no. 5, pp. 717–727, 2000.

[41] C.-W. Tsao, C.-Y. Liu, T.-L. Cha, S.-T. Wu, G.-H. Sun, D.-S. Yu, H.-I. Chen, S.-Y. Chang, S.-C. Chen, and C.-Y. Hsu, "Artificial neural network for predicting pathological stage of clinically localized prostate cancer in a taiwanese population," *Journal of the Chinese Medical Association*, vol. 77, no. 10, pp. 513–518, 2014.

[42] J. T. Connor, R. D. Martin, and L. E. Atlas, "Recurrent neural networks and robust time series prediction," *IEEE transactions on neural networks*, vol. 5, no. 2, pp. 240–254, 1994.

[43] Z. C. Lipton, J. Berkowitz, and C. Elkan, "A critical review of recurrent neural networks for sequence learning," *arXiv preprint arXiv:1506.00019*, 2015.

[44] B. Schrauwen, D. Verstraeten, and J. Van Campenhout, "An overview of reservoir computing: theory, applications and implementations," in *Proceedings of the 15th european symposium on artificial neural networks. p. 471-482 2007*, pp. 471–482, 2007.

[45] K. Fu, R. Zhu, A. Loeffler, J. Hochstetter, A. Diaz-Alvarez, A. Stieg, J. Gimzewski, T. Nakayama, and Z. Kuncic, "Reservoir computing with neuromemristive nanowire networks," in *2020 International Joint Conference on Neural Networks (IJCNN)*, pp. 1–8, IEEE, 2020.

[46] H. Jaeger and H. Haas, "Harnessing nonlinearity: Predicting chaotic systems and saving energy in wireless communication," *science*, vol. 304, no. 5667, pp. 78–80, 2004.

[47] T. Tuma, A. Pantazi, M. Le Gallo, A. Sebastian, and E. Eleftheriou, "Stochastic phase-change neurons," *Nature nanotechnology*, vol. 11, no. 8, p. 693, 2016.

[48] G. Indiveri, B. Linares-Barranco, T. J. Hamilton, A. Van Schaik, R. Etienne-Cummings, T. Delbruck, S.-C. Liu, P. Dudek, P. Häfliger, S. Renaud, *et al.*, "Neuromorphic silicon neuron circuits," *Frontiers in neuroscience*, vol. 5, p. 73, 2011.

[49] D. A. McCormick, Y. Shu, and Y. Yu, "Hodgkin and huxley model—still standing?," *Nature*, vol. 445, no. 7123, pp. E1–E2, 2007.

[50] C. Mead and M. Ismail, *Analog VLSI implementation of neural systems*, vol. 80. Springer Science & Business Media, 2012.

[51] J. V. Arthur and K. Boahen, "Recurrently connected silicon neurons with active dendrites for one-shot learning," in *2004 IEEE International Joint Conference on Neural Networks (IEEE Cat. No. 04CH37541)*, vol. 3, pp. 1699–1704, IEEE, 2004.

[52] C. Bartolozzi and G. Indiveri, "Synaptic dynamics in analog vlsi," *Neural computation*, vol. 19, no. 10, pp. 2581–2603, 2007.

[53] D. B. Strukov, G. S. Snider, D. R. Stewart, and R. S. Williams, "The missing memristor found," *nature*, vol. 453, no. 7191, pp. 80–83, 2008.

[54] L. Deng, D. Wang, Z. Zhang, P. Tang, G. Li, and J. Pei, "Energy consumption analysis for various memristive networks under different learning strategies," *Physics Letters A*, vol. 380, no. 7-8, pp. 903–909, 2016.

[55] D. Kuzum, S. Yu, and H. P. Wong, "Synaptic electronics: materials, devices and applications," *Nanotechnology*, vol. 24, no. 38, p. 382001, 2013.

[56] M. Hu, H. Li, Y. Chen, Q. Wu, G. S. Rose, and R. W. Linderman, "Memristor crossbar-based neuromorphic computing system: A case study," *IEEE transactions on neural networks and learning systems*, vol. 25, no. 10, pp. 1864–1878, 2014.

[57] X. Feng, Y. Li, L. Wang, S. Chen, Z. G. Yu, W. C. Tan, N. Macadam, G. Hu, L. Huang, L. Chen, *et al.*, "A fully printed flexible mos2 memristive artificial synapse with femtojoule switching energy," *Advanced Electronic Materials*, vol. 5, no. 12, p. 1900740, 2019.

[58] M. Prezioso, F. Merrikh-Bayat, B. Hoskins, G. C. Adam, K. K. Likharev, and D. B. Strukov, "Training and operation of an integrated neuromorphic network based on metal-oxide memristors," *Nature*, vol. 521, no. 7550, pp. 61–64, 2015.

[59] M. A. Zidan, Y. Jeong, J. Lee, B. Chen, S. Huang, M. J. Kushner, and W. D. Lu, "A general memristor-based partial differential equation solver," *Nature Electronics*, vol. 1, no. 7, pp. 411–420, 2018.

[60] K.-H. Kim, S. Gaba, D. Wheeler, J. M. Cruz-Albrecht, T. Hussain, N. Srinivasa, and W. Lu, "A functional hybrid memristor crossbar-array/cmos system for data storage and neuromorphic applications," *Nano letters*, vol. 12, no. 1, pp. 389–395, 2012.

[61] L. Patrick, C. Posch, and T. Delbruck, "A 128x 128 120 db 15μ s latency asynchronous temporal contrast vision sensor," *IEEE journal of solid-state circuits*, vol. 43, pp. 566–576, 2008.

[62] P. A. Merolla, J. V. Arthur, R. Alvarez-Icaza, A. S. Cassidy, J. Sawada, F. Akopyan, B. L. Jackson, N. Imam, C. Guo, Y. Nakamura, *et al.*, "A million spiking-neuron integrated circuit with a scalable communication network and interface," *Science*, vol. 345, no. 6197, pp. 668–673, 2014.

[63] M. V. DeBole, B. Taba, A. Amir, F. Akopyan, A. Andreopoulos, W. P. Risk, J. Kusnitz, C. O. Otero, T. K. Nayak, R. Appuswamy, *et al.*, "Truenorth: Accelerating from zero to 64 million neurons in 10 years," *Computer*, vol. 52, no. 5, pp. 20–29, 2019.

[64] V. K. Sangwan and M. C. Hersam, "Neuromorphic nanoelectronic materials," *Nature nanotechnology*, vol. 15, no. 7, pp. 517–528, 2020.

[65] A. V. Avizienis, H. O. Sillin, C. Martin-Olmos, H. H. Shieh, M. Aono, A. Z. Stieg, and J. K. Gimzewski, "Neuromorphic atomic switch networks," *PloS one*, vol. 7, no. 8, p. e42772, 2012.

[66] A. Z. Stieg, A. V. Avizienis, H. O. Sillin, C. Martin-Olmos, M. Aono, and J. K. Gimzewski, "Emergent criticality in complex turing b-type atomic switch networks," *Adv. Mater*, vol. 24, pp. 286–293, 2012.

[67] A. Diaz-Alvarez, R. Higuchi, Q. Li, Y. Shingaya, and T. Nakayama, "Associative routing through neuromorphic nanowire networks," *AIP Advances*, vol. 10, no. 2, p. 025134, 2020.

[68] Z. Kuncic, I. Marcus, P. Sanz-Leon, R. Higuchi, Y. Shingaya, M. Li, A. Stieg, J. Gimzewski, M. Aono, and T. Nakayama, "Emergent brain-like complexity from nanowire atomic switch networks: Towards neuromorphic synthetic intelligence," in *2018 IEEE 18th International Conference on Nanotechnology (IEEE-NANO)*, pp. 1–3, IEEE, 2018.

[69] Z. Kuncic, O. Kavehei, R. Zhu, A. Loeffler, K. Fu, J. Hochstetter, M. Li, J. M. Shine, A. Diaz-Alvarez, A. Stieg, *et al.*, "Neuromorphic information processing with nanowire networks," in *2020 IEEE International Symposium on Circuits and Systems (ISCAS)*, pp. 1–5, IEEE, 2020.

[70] P. Jena and A. W. Castleman Jr, *Nanoclusters: a bridge across disciplines*. Elsevier, 2010.

[71] J. B. Mallinson, *Percolating Atomic Switch Networks for Neuromorphic Computing*. PhD thesis, Department of Physics and Astronomy, Univerisity of Canterbury, 2020.

[72] S. Ali, V. Myasnichenko, and E. Neyts, "Size-dependent strain and surface energies of gold nanoclusters," *Physical Chemistry Chemical Physics*, vol. 18, no. 2, pp. 792–800, 2016.

[73] N. S. Phala and E. Van Steen, "Intrinsic reactivity of gold nanoparticles: Classical, semi-empirical and dft studies," *Gold Bulletin*, vol. 40, no. 2, pp. 150–153, 2007.

[74] R. Reichel, J. G. Partridge, A. D. Dunbar, S. A. Brown, O. Caughley, and A. Ayesh, "Construction and application of a uhv compatible cluster deposition system," *Journal of Nanoparticle Research*, vol. 8, no. 3, pp. 405–416, 2006.

[75] A. Sattar, *Electrical Characterization of Cluster Devices*. PhD thesis, Department of Physics and Astronomy, Univerisity of Canterbury, 2011.

[76] S. Fostner, R. Brown, J. Carr, and S. A. Brown, "Continuum percolation with tunneling," *Physical Review B*, vol. 89, no. 7, p. 075402, 2014.

[77] S. Fostner and S. A. Brown, "Neuromorphic behavior in percolating nanoparticle films," *Physical Review E*, vol. 92, no. 5, p. 052134, 2015.

[78] J. W. Essam, "Percolation theory," *Reports on progress in physics*, vol. 43, no. 7, p. 833, 1980.

[79] D. Stauffer and A. Aharony, *Introduction to percolation theory*. CRC press, 2018.

[80] E. T. Gawlinski and H. E. Stanley, "Continuum percolation in two dimensions: Monte carlo tests of scaling and universality for non-interacting discs," *Journal of Physics A: Mathematical and General*, vol. 14, no. 8, p. L291, 1981.

[81] K. Terabe, T. Hasegawa, T. Nakayama, and M. Aono, "Quantized conductance atomic switch," *Nature*, vol. 433, no. 7021, pp. 47–50, 2005.

[82] M. Olsen, M. Hummelgård, and H. Olin, "Surface modifications by field induced diffusion," *PLoS One*, vol. 7, no. 1, p. e30106, 2012.

[83] T. Ganetsos, A. Mair, G. Mair, L. Bischoff, C. Akhmadaliev, and C. Aidinis, "Can direct field-evaporation of doubly charged ions and post-ionisation from the singly charged state co-exist?," *Surface and Interface Analysis: An International Journal devoted to the development and application of techniques for the analysis of surfaces, interfaces and thin films*, vol. 39, no. 2-3, pp. 128–131, 2007.

[84] H.-C. Yu, S. Liu, and C. Chen, "Study of electromigration in thin tin film using edge displacement method," *Journal of applied physics*, vol. 98, no. 1, p. 013540, 2005.

[85] P. Bonifazi, M. Goldin, M. A. Picardo, I. Jorquera, A. Cattani, G. Bianconi, A. Represa, Y. Ben-Ari, and R. Cossart, "Gabaergic hub neurons orchestrate synchrony in developing hippocampal networks," *Science*, vol. 326, no. 5958, pp. 1419–1424, 2009.

[86] C. Meisel, K. Bailey, P. Achermann, and D. Plenz, "Decline of long-range temporal correlations in the human brain during sustained wakefulness," *Scientific reports*, vol. 7, no. 1, pp. 1–11, 2017.

[87] W. L. Shew and D. Plenz, "The functional benefits of criticality in the cortex," *The neuroscientist*, vol. 19, no. 1, pp. 88–100, 2013.

[88] R. V. Janssens, "Elusive magic numbers," *Nature*, vol. 435, no. 7044, pp. 897–898, 2005.

[89] D. R. Lide, *CRC handbook of chemistry and physics*, vol. 85. CRC press, 2004.

[90] P. Song and D. Wen, "Experimental investigation of the oxidation of tin nanoparticles," *The Journal of Physical Chemistry C*, vol. 113, no. 31, pp. 13470–13476, 2009.

[91] S. Cho, J. Yu, S. K. Kang, and D.-Y. Shih, "Oxidation study of pure tin and its alloys via electrochemical reduction analysis," *Journal of electronic materials*, vol. 34, no. 5, pp. 635–642, 2005.

[92] E. Sutter, F. Ivars-Barcelo, and P. Sutter, "Size-dependent room temperature oxidation of tin particles," *Particle & Particle Systems Characterization*, vol. 31, no. 8, pp. 879–885, 2014.

[93] H. S. Dow, W. S. Kim, and J. W. Lee, "Thermal and electrical properties of silicon nitride substrates," *AIP Advances*, vol. 7, no. 9, p. 095022, 2017.

[94] D. Andrews, T. Nann, and R. H. Lipson, *Comprehensive nanoscience and nanotechnology*. Academic press, 2019.

[95] E. Galli, *Mulitple Electrode Percolating Atomic Switch Networks*. PhD thesis, Department of Physics and Astronomy, Univerisity of Canterbury, 2021.

[96] R. Reichel, *Nano Scale Cluster Devices*. PhD thesis, Department of Physics and Astronomy, Univerisity of Canterbury, 2007.

[97] C. B. Nakhosteen and K. Jousten, *Handbook of vacuum technology*. John Wiley & Sons, 2016.

[98] P. J. Kelly and R. D. Arnell, "Magnetron sputtering: a review of recent developments and applications," *Vacuum*, vol. 56, no. 3, pp. 159–172, 2000.

[99] R. Behrisch and W. Eckstein, *Sputtering by particle bombardment: experiments and computer calculations from threshold to MeV energies*, vol. 110. Springer Science & Business Media, 2007.

[100] B. Von Issendorff and R. Palmer, "A new high transmission infinite range mass selector for cluster and nanoparticle beams," *Review of scientific instruments*, vol. 70, no. 12, pp. 4497–4501, 1999.

[101] M. D. Pike, "A deterministic model of a neuromorphic nanoparticle network," Master's thesis, Department of Electrical and Computer Engineering, Univerisity of Canterbury, 2019.

[102] Z. E. Heywood, *Simulation Models and Computational Exploitation of Percolating Atomic Switch Networks*. PhD thesis, Department of Electrical and Computer Engineering, University of Canterbury, 2021.

[103] C. Adami, "What is complexity?," *BioEssays*, vol. 24, no. 12, pp. 1085–1094, 2002.

[104] C. H. Lineweaver, P. C. Davies, and M. Ruse, "What is complexity? is it increasing," *Complexity and the Arrow of Time*, pp. 3–15, 2013.

[105] N. Marshall, N. M. Timme, N. Bennett, M. Ripp, E. Lautzenhiser, and J. M. Beggs, "Analysis of power laws, shape collapses, and neural complexity: new techniques and matlab support via the ncc toolbox," *Frontiers in physiology*, vol. 7, p. 250, 2016.

[106] G. Tononi, O. Sporns, and G. M. Edelman, "A measure for brain complexity: relating functional segregation and integration in the nervous system," *Proceedings of the National Academy of Sciences*, vol. 91, no. 11, pp. 5033–5037, 1994.

[107] G. Tononi, G. M. Edelman, and O. Sporns, "Complexity and coherency: integrating information in the brain," *Trends in cognitive sciences*, vol. 2, no. 12, pp. 474–484, 1998.

[108] C. E. Shannon, "A mathematical theory of communication," *The Bell system technical journal*, vol. 27, no. 3, pp. 379–423, 1948.

[109] N. M. Timme and C. Lapish, "A tutorial for information theory in neuroscience," *eneuro*, vol. 5, no. 3, 2018.

[110] T. M. Cover, *Elements of information theory*. John Wiley & Sons, 1999.

[111] M. M. Schartner, A. Pigorini, S. A. Gibbs, G. Arnulfo, S. Sarasso, L. Barnett, L. Nobili, M. Massimini, A. K. Seth, and A. B. Barrett, "Global and local complexity of intracranial eeg decreases during nrem sleep," *Neuroscience of consciousness*, vol. 2017, no. 1, p. niw022, 2017.

[112] A. K. Seth, "Causal connectivity of evolved neural networks during behavior," *Network: Computation in Neural Systems*, vol. 16, no. 1, pp. 35–54, 2005.